4. THE GG PAYLOAD

4.1 PAYLOAD CONFIGURATION

The GG payload is constituted by: the PGB (Pico Gravity Box) laboratory enclosing, in a nested configuration, two cylindrical test bodies with the read-out capacitance plates for very accurate sensing of their relative displacements, the small capacitance sensors/actuators for sensing relative displacements and damping the whirl motions, the suspension springs and the coupling flat gimbals, the FEEP thrusters for drag compensation (physically located on the spacecraft outer surface), the inchworms and piezo-ceramics for fine mechanical balancing and calibration. All suspended bodies are provided with a locking mechanism to withstand launch accelerations and to be unlocked once the nominal attitude (perpendicular to the orbit plane) and spin rate (*2 Hz*) have been achieved at the nominal orbit (circular, equatorial, *520 km* altitude). In addition, all bodies have a locking mechanism made of inch-worms for finer control of their unlocking at the beginning of the mission (as discussed in Sec. 2.1.6). The payload apparatus includes the electronics (for calibration, signal measurements, FEEP control and whirl damping), with the necessary electric connections, and the thermal insulation. In addition, the PGB carries a small mirror, in correspondence of a photo-detector mounted on the inner surface of the spacecraft, for the measurement of small residual phase lags between the spacecraft and the PGB which might remain despite the passive mass compensation mechanism (see Chap. 5 and Fig. 5.7); residual phase lags will be reduced to acceptable levels using the FEEP. No such phase lags will arise between the test bodies due to the thermal stability achieved inside the PGB (see Sec. 4.4).

The mass budget of the payload, with mention to the materials used, is given in Table 4.1 where all values are calculated from the 3-D model of the system developed with the IDEAS software package. The model provides 3-D views of all sub-systems in addition to 2-D technical drawings of all components. This exercise is especially important for the GG payload where the constraints posed by the available physical room are rather stringent due to the compactness of the GG satellite. As far as the GG cost evaluation is concerned (provided to ASI on October 1st 1998) it should be recalled that the cost of the FEEP and FEEP control electronics is part of the payload, although the corresponding mass is given in the GG mass budget as part of the spacecraft (see Table. 5.18).

The locking/unlocking mechanisms (LUM) of the test bodies are shown in Fig. 4.1, showing the PGB tube, enclosing the coupling arms and the mechanical suspensions of the test bodies, and the top and bottom LUM. The test bodies are not shown in this Figure to help understanding how locking/unlocking is achieved. Each LUM (there is one at the top and one at the bottom) has: 4 mechanical arms connecting it rigidly to the PGB laboratory, 8 fixing cylindrical bullets, 4 for holding the inner test cylinder and 4 for holding the outer test cylinder, which are inserted into the test bodies during the GG assembling (note that the inner test cylinder has smaller height than the outer one and therefore the bullets for holding it need to be mounted on higher supports); 8 actuators, 4 per test body, to pull out the cylindrical bullets whereby unlocking the test bodies; a transmission mechanism. At the time of unlocking the actuators, by means of the transmission mechanism, pull out the cylindrical bullets from the test bodies whereby freeing them. The actuators taken into consideration for this purpose are either electric motors or paraffin actuators (as used already in BeppoSAX). The electric motors would be located on the mechanical arms far away from the test bodies; in any case, they need to be used only once, at the beginning of the operation phase. After unlocking the motors would be switched off and, in case of paraffin actuators, the required heat would be dissipated and the heat source turned off. Note that, once freed, the test bodies are constrained by mechanical stops which allow them to perform only little movements (about *0.5 cm* room). This is well visible in Fig. 4.1, showing the shafts sticking out of the PGB tube (8 per test body, 4 at the top and 4 at the bottom, each arm at 90º from the next). In addition, as discussed in Sec.

2.1.6, Fig. 2.20, a finer locking is available by means of inch-worms equipped with pressure sensors (8 per test body, 4 at the top and 4 at the bottom) which allows fine release and ensures a safe transient from the initial unlocking to the dynamical state at *regime* simulated numerically in Chap. 6.

ITEM NAME	MATERIAL	DENSITY (g/cm^3)	MASS (KG)	QUANTITY
Internal Test mass	Copper	8.96	10	1
External Test Mass	Beryllium	1.84	10	1
PGB Cylinder	Aluminum (ERGAL)	2.8	39.19	1
PGB Covers	Aluminum (ERGAL)	2.8	20.68	2
(Partial Total)			(79.870)	
Test Body Mechanism (outer mass)	TiAl6V4	4.5	0.066	2
Test Body Mechanism (inner mass)	TiAl6V4	4.5	0.048	2
L.U.M. (top)	Aluminum (ERGAL)	2.8	1.16	1
L.U.M. (bottom)	Aluminum (ERGAL)	2.8	1.16	1
Active Dampers on Test Bodies	Aluminum (ERGAL)	2.8	0.019	16
Active Dampers on PGB	Aluminum (ERGAL)	2.8	0.019	16
Active Dampers Arms	TiAl6V4	4.5	0.014	32
Read-out Capacitors, Inch-worms, Rods			1	
(Partial Total)			(3.486)	
Total Payload Mass			83.356	

Table 4.1 Mass budget of the GG payload. The various components of the payload are listed, save for the electronics and the payload computer. This Table is consistent with Table 5.18, giving the GG total mass budget, where mass margins are also taken into account.

The locking/unlocking mechanism mounted with the inner test cylinder is shown in Fig. 4.2. The outer test cylinder is shown in Fig. 4.3, with the PGB tube only and no locking/unlocking mechanism. This figure shows clearly the 4 shafts at the top sticking out of the PGB tube, inside which they are connected together and suspended by a spring to the arms that couple the test bodies via flat gimbals, as shown in Fig. 2.1.

The relative position of the test cylinders is sensed by means of 4 capacitance plates, with cylindrical curvature, located in between them at 90º from one another forming 2 capacitance bridges (see Fig. 4.4). Each plate is rigidly connected to the PGB tube via two inch-worms (one

at the top and 1 at the bottom) for fine adjusting its position halfway between the outer surface of the inner cylinder and the inner surface of the outer one (mechanical balancing of the bridge). The relative position of each test cylinder with respect to the PGB is sensed also by means of two capacitance bridges, however the plates of the bridges in this case are much smaller (see Fig. 4.2). These small capacitors are used as actuators as well, to damp the relative whirl motions (see Sec. 2.1.5 and Chap. 6), hence, each test body has 8 small dampers, 4 at the top and 4 at the bottom, at 90º from one another. Each damper is made of 2 little plates facing each other; one plate is rigidly connected to one test cylinder and the other to the case of one inch-worm, which in its turn is rigidly connected to the PGB tube. In this way they can sense the relative position of each test body with respect to the PGB and also actuate according to appropriate control laws. Fig. 4.4 shows the dampers (in light blue): in this figure each damper of the inner test cylinder is connected on both ends (one plate to the test cylinder and the other plate to the inch-worm case), while those of the outer test cylinder are connected only to the inch-worm cases because the outer test cylinder is not shown. Although they are not shown in any of these drawings, there are active dampers also between the PGB tube and the spacecraft, as schematized in Fig. 2.7. Each damper is made of two little plates, just like those described here for the test bodies; the inner plate is rigidly connected to the PGB tube while the outer one is rigidly connected to a short spacecraft tube; in addition, axial movements between the PGB and the spacecraft can be sensed and adjusted, which requires 8 additional small dampers between the PGB and the spacecraft, 4 at the top and 4 at the bottom (see Fig. 2.7). In total, the PGB has 16 small dampers.

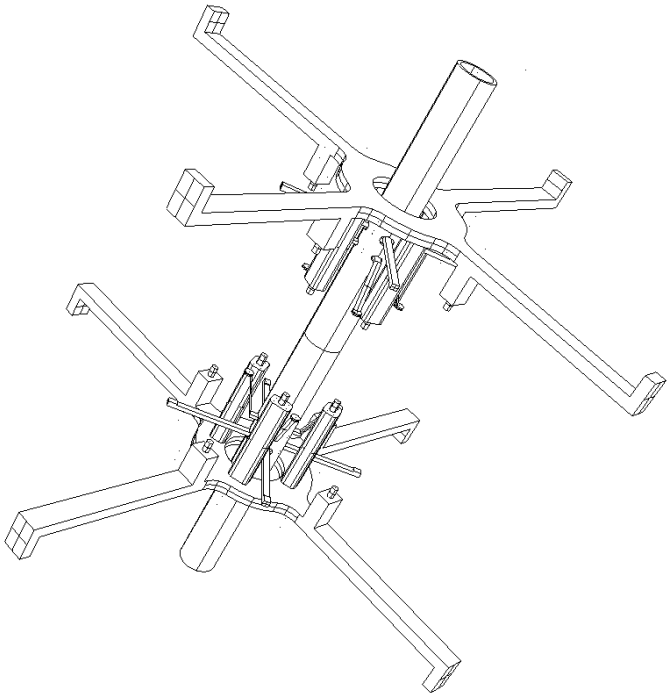

Figure 4.1 The PGB tube, enclosing the coupling arms and the mechanical suspensions of the cylindrical test bodies (not shown) and their locking/unlocking mechanisms, one at the top and one at the bottom. Every such mechanism shows: 4 mechanical arms (for rigid connection to the PGB cylindrical surface), 8 cylindrical bullets for holding the test cylinders (4 per test cylinder, each cylindrical bullet has its own actuator). The actuators are shown enclosed in a metallic case above or below each cylindrical bullet. Although the test cylinders are not shown, the shafts which stick out of the PGB tube (8 per test body, 4 at the top and 4 at the bottom) are well visible; they are rigidly connected to the test bodies on the far end and to the suspension springs on the other (the suspension springs are located inside the PGB tube as it is better shown in a section through the spin/symmetry axis, as in Fig. 2.1). Only limited movements (about half a cm) are permitted to each shaft, hence to the test bodies; this feature is also referred to as a mechanical stop.

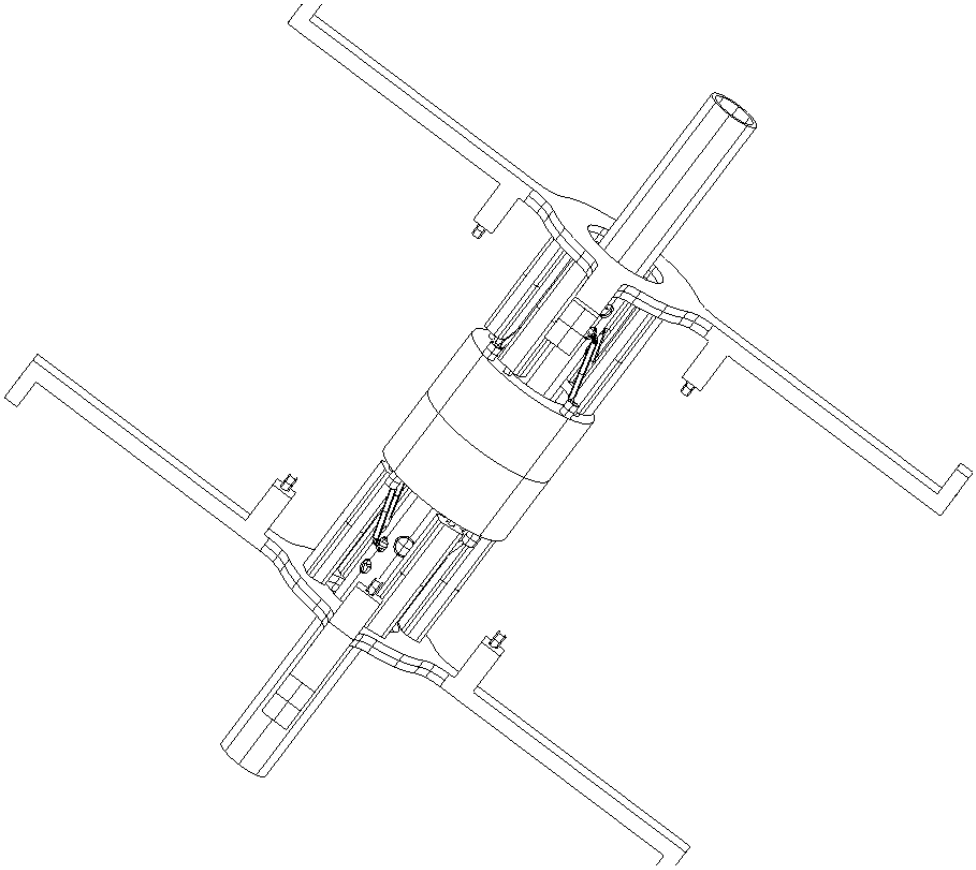

Figure 4.2. The locking/unlocking mechanisms as in Fig. 4.1 with the addition of the inner test cylinder mounted and locked by means of the 8 cylindrical bullets (4 at the top and 4 at the bottom) of the locking/unlocking device previously shown in Fig. 4.1

A 3-D view of the PGB tube, the locking/unlocking mechanisms, the inner test body, the read-out capacitors, the inch-worms and the small plates of the capacitance sensors/actuators is shown in Fig. 4.4. The outer test cylinder is not drawn in this figure since it would prevent all parts inside it from being seen; the inch-worms are schematized as small cylinders in light-blue, the small plates of the capacitance sensors/actuators are shown in light blue; the large capacitance plates of the read-out are shown in pink; the locking/unlocking mechanisms are well visible in gray. The caption of Fig. 4.4 gives a rather detailed description of the GG experimental apparatus inside the PGB laboratory with the help of colors. It is worth adding that power and signals are brought inside the PGB via its helical suspension springs (3 wires each spring), as described in Chap. 2.1 (see Sec.2.1.1 and Fig. 2.5). No electric signal goes through the helical springs which suspend the test bodies (2 for each body, not shown in any of these figures because they are located inside the PGB tube; see Fig. 2.1). The piezoceramics used for calibration and for adjusting the arms which couple the test cylinders (also located inside the PGB tube and therefore not shown) need to be commanded: this requires 3 wires, which are selected to be 3 of the 6 wire sectors of each of the two flat gimbals through which the coupling arms are connected to the PGB tube, so that they can be insulated at their clamping rings (see Sec. 2.1.1 and Fig. 2.3).

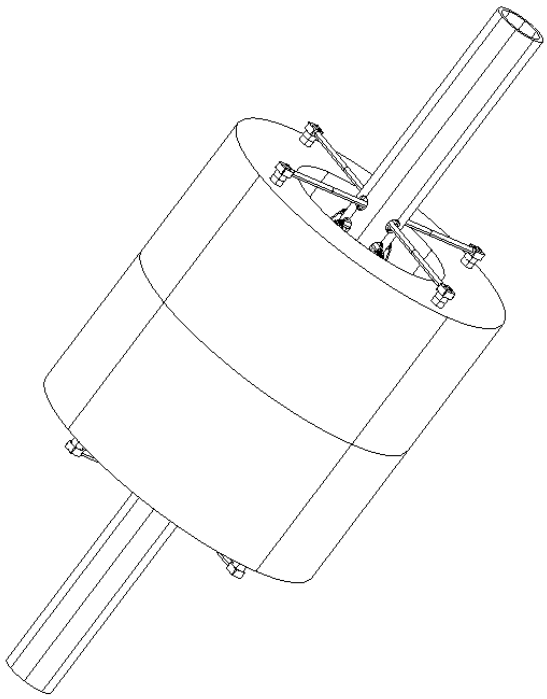

Figure 4.3 The PGB tube and the outer test cylinder. The locking/unlocking mechanism is not shown. The read-out capacitors and inner test mass are hidden by the outer test cylinder. The 4 shafts (at the top) which stick out of the PGB tube and are connected to the outer cylinder are clearly visible (there are 4 shafts at the bottom as well). It is apparent that the body is permitted very limited movements only (by about half a cm) because the 4 shafts are constrained by mechanical stops consisting of small holes on the PGB tube (usually referred to as mechanical stops). All 4 of them connect together inside the tube, where a suspension helical spring connects them (hence the test body) to one coupling arm located inside the tube. Another helical spring connects the 4 shafts located at the bottom to the other coupling arm inside the PGB (see Fig. 2.1 for a section through the spin/symmetry axis).

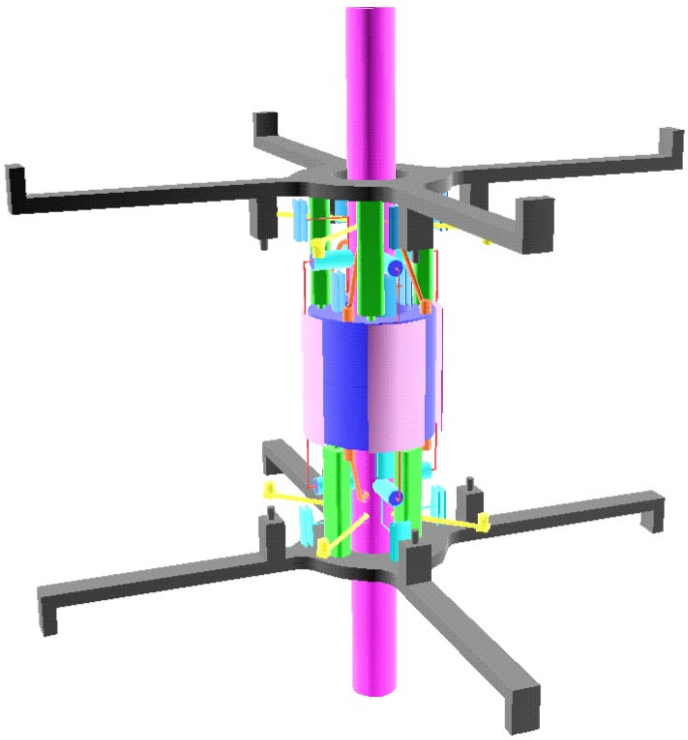

Figure 4.4 Overall, 3-D view of the GG experimental apparatus internal to the PGB laboratory (only the central tube of the PGB is shown (in dark pink). Of the actual apparatus that will be located inside the PGB everything is shown here except the outer test cylinder, which would hide all the components inside it. The locking/unlocking mechanisms are shown in gray; the cylindrical bullets and their actuators, also in gray, are well visible only for the outer test cylinder; the inner test cylinder is locked. It is shown in blue, partially covered by the capacitance plates of the read-out (in pink). The inch-worms for the mechanical balancing of the plates are schematized as small cylinders in light blue. Note that these plates are rigidly connected (through the inch worms) to the PGB tube. There is one inch-worm per radial shaft, each plate has 2 shafts, 1 at the top and 1 at the bottom, amounting to 8 shafts and 8 inch-worms for the total read-out system. The small plates of the active dampers are shown in light blue. Each damper consists of 2 halves: 1 is connected to the inch-worm case, hence to the PGB, and the other to the test body. In this way it is possible to sense the relative position of each test body with respect to the PGB, and to actuate in order to damp their whirl motions (see Chap. 6)

4.2 FEEP THRUSTERS AND CONTROL ELECTRONICS

4.2.1 FEEP THRUSTERS

THE FEEP THRUSTER CONCEPT Field Emission Electric Propulsion (FEEP) is an electrostatic propulsion concept (Bartoli *et al.*, 1984) based on field ionization of a liquid metal and subsequent acceleration of the ions by a strong electric field. FEEP is currently the object of great interest in the scientific community, due to its unique features: $1\ \mu N$ to $1\ mN$ thrust range, near instantaneous switch on / switch off capability, and high-resolution throttleability (better than one part in 10^4), which enables accurate thrust modulation in both continuous and pulsed modes. Presently baselined for several scientific missions onboard drag-free satellites, this propulsion system has been also proposed for attitude control and orbit maintenance on commercial small satellites and constellations (Marcuccio *et al.*, 1997). Developed at Centrospazio with power and control electronics made by LABEN, the FEEP system will be flight tested on a Get Away Special canister onboard the Space Shuttle in early *2000*.

In the past, most FEEP development efforts were focused on enhancing the current extracted, in an attempt to obtain higher thrust levels. At thrust levels of above a few *milli-Newton*, FEEP has some drawbacks due to the very high specific impulse, which is associated with a very high power-to-thrust ratio. As no established solution was identified to reduce specific impulse, the development of FEEP as a *milli-Newton* level thruster was almost terminated in the late '80s. The recent shift of perspective on FEEP technology, which now focuses on the very low current capability of this thruster, has drastically changed this situation. At very low thrust levels (i.e., in the *micronewton* range), the traditional FEEP slit emitter performs best, and its features make it the only candidate for several space applications.

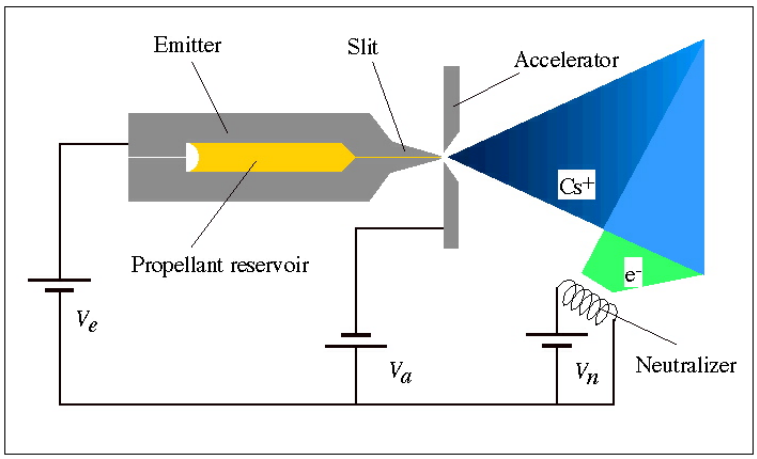

Fig. 4.5 The FEEP Principle

In FEEP emitters, unlike most ion engines, ions are directly extracted from the liquid phase. The thruster can accelerate a large number of different liquid metals or alloys. Cesium is usually selected for its high atomic weight, low ionization potential, low melting point ($28.4\ °C$), and good wetting capabilities on the emitter substrate. Specific impulse is in the $4000 - 10000\ s$ range, and may be easily adjusted to meet specific mission requirements. Thrust level can be finely tuned (Marcuccio *et al.*, 1998), and instantaneous switching capability allows pulsed mode operation and accurate thrust modulation at high bandwidth.

Thrust is produced by exhausting a beam of mainly singly-ionized Cesium atoms, produced by field evaporation. The emitter module consists of two metallic plates with a small propellant reservoir. A sharp blade is accurately machined on one side of each plate. A thin layer of *Ni* is

sputter-deposited on the other three sides of one of the plates, to act as a spacer; when the two emitter halves are tightly clamped together, a slit of about $1\ \mu m$ is left between the blades. Cesium flows through this tiny channel, forming a free surface at the exit of the slit with a radius of curvature in the order of $1\ \mu m$. Under a strong electric field generated by the application of a voltage difference between the emitter and an accelerator electrode located directly in front of it, the free surface of the liquid metal approaches a condition of local instability, due to the combined effects of the electrostatic force and the surface tension. A series of protruding cusps, or "Taylor cones," are created. When the electric field reaches a value of about $10^9\ V/m$, the atoms at the tip spontaneously ionize and an ion jet is extracted by the electric field, while the electrons are rejected in the bulk of the liquid. An external source of electrons provides negative charges to maintain global electrical neutrality of the thruster assembly. Mass flow rate is extremely low and requires no control, as the particles extracted are replaced by the capillary actions from the propellant reservoir at a rate sufficient to maintain dynamic equilibrium at the emitter tip. When voltage is removed, the capillary force prevents the propellant from pouring out of the slit.

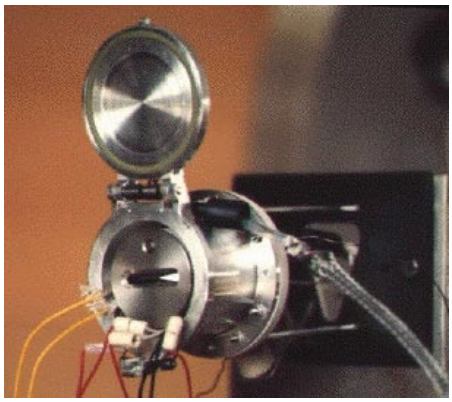

Fig. 4.6 A $30\ \mu N$ FEEP thruster assembly during thermal vacuum test

THRUSTER DEVELOPMENT STATUS A FEEP thruster endurance test, aimed at totaling *2000 hours* of operation, is under preparation in the ESTEC Electric Propulsion Laboratory under the responsibility of Centrospazio. Starting in end 1998, this test will exploit a set of diagnostics (ion beam probes, quartz crystal microbalances, etc.) to fully characterize the thruster performance and the plume effects on nearby surfaces.

Realization of a thrust balance (Paolucci *et al.*, 1997) is underway. The envisaged design is aimed at measuring $100\ \mu N$ maximum thrust with a resolution of $0.1\ \mu N$.

The thruster design is being finalized for its first space test. In 1997, ESA awarded a contract to Centrospazio to perform a FEEP flight demonstration (Marcuccio *et al.*, 1998) on a Get Away Special (GAS) canister onboard the Space Shuttle. The industrial team set up to carry out this task includes Centrospazio as prime contractor, with LABEN (Milan, Italy) and Techno System Developments (Pozzuoli, Italy) as subcontractors for the FEEP Electronics Unit (FEU) and the GAS Experiment Electronics, respectively. Known as EMITS (Electric MIcrothruster Test in Space), this experiment is aimed at:

- demonstrating that the FEEP system is robust enough to withstand typical launch loads;
- firing the thruster in space for the first time;
- demonstrating the propellant storage and container sealing functionality;
- demonstrating proper operation in microgravity of propellant feeding by capillarity;

- demonstrating thruster proper operation in such an adverse environment as the low altitude, water vapor- and oxygen-rich Shuttle orbit;
- demonstrating ion beam neutralization;
- assessing the plume current distribution;
- evaluating the propellant backflow and deposition on surrounding surfaces;
- testing the power conditioning unit in operational environment.

Direct thrust measurement will not be performed, to avoid excessive complication of the experimental setup. Indirect thrust measurement will be performed using the electrical parameter data. Evidence of the ion beam presence will be gained by means of electrical measurements in the thruster's power supply lines and, independently, by means of ion beam electrostatic probes.

The experiment will be accommodated in a GAS canister, equipped with a Motorized Door Assembly (MDA). The GAS/MDA hardware and the flight onboard the Shuttle are provided by NASA, through an existing agreement with ESA. The GAS canister doesn't receive power, nor exchanges data with the Shuttle, except a pre-defined set of four telecommands used to switch on and off the experiment. Therefore, all the necessary experiment hardware and support equipment must be carried within the GAS, including:

- the battery pack;
- the experiment management electronics, including raw power conditioning, onboard computer, data acquisition and storage;
- the thruster power electronics;
- the thrusters, including the neutralizers;
- the movable electrostatic probe assemblies and the propellant deposition monitors.

The experiment layout is shown in Fig. 4.7.

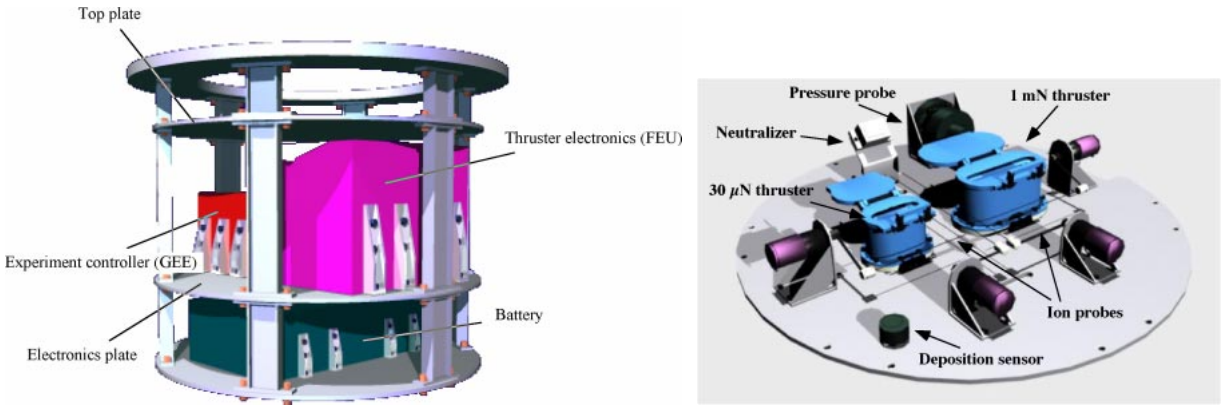

Fig. 4.7 The EMITS (Electric Microthruster test in Space) Experiment: left, overall arrangement; right, top plate close-up

EMITS will feature two different thruster assemblies, each including its own sealed container, heater, temperature sensor, emitter and accelerator. In order to cover the thrust ranges of interest of both commercial and scientific applications of FEEP, the following two emitter slit lengths have been selected:

- $2\ mm$ slit length: nominal thrust = $30\ \mu N$, power consumption = $1.8\ W$;
- $70\ mm$ slit length: nominal thrust = $1\ mN$, power consumption = $60\ W$.

The thruster module design includes a sealed container, to protect the thruster during the pre-launch phases. The container provides a sealed envelope filled with an inert gas, which protects the emitter from interaction with air, to avoid slit clogging due to formation of propellant oxides from the moment of propellant filling to thruster operation start in orbit. A new container assembly has been recently developed to host the $30\ \mu N,\ 2\ mm$ slit length emitter. The new container features an improved sealing system and a paraffin actuator for lid release.

The liquid metal used as propellant (Cs or Rb) will be stored in the emitter internal reservoir. Propellant feeding to the emitter tips will be performed by capillarity. The emitters will be loaded with about $2\ grams$ of propellant each. The onboard controller will record, at appropriate sampling rates, the main electrical parameters (thruster voltages and currents), several temperatures (emitters, neutralizers, FEU, onboard computer, battery) and the data from the propellant deposition sensors. All data will be stored onboard, and will be available for analysis upon Shuttle return from orbit.

As of October, 1998, NASA has approved the EMITS Payload Accommodation Requirements and EMITS has been assigned payload number G-752.

More information can be found on the Internet at http://www.centrospazio.cpr.it

4.2.2 FEEP CONTROL ELECTRONICS

The FEEP Electronic Unit proposed for GG is being developed in Laben under an ESA contract. The Block Diagram of this unit is shown in Fig. 4.8. The unit can be easily adapted to the GG needs; two units are needed to manage the 8 FEEP thrusters currently foreseen for GG. The FEEP Electronic Unit is constituted by the following items:

- Overall control system which receives the commands from and provide the H/K to the Payload Data Processor, and control the main thruster parameters .
- Four Emitter High Voltage Power Supply (HVPS) whose output voltage shall be programmable in the range *3KV* to *5KV*
- Accelerator HVPS whose output voltage shall be programmable in the range *-3KV* to *–5.5KV*
- Neutralizer Low Voltage Power Supply will be obtained directly from the FEU main DC-DC converter.

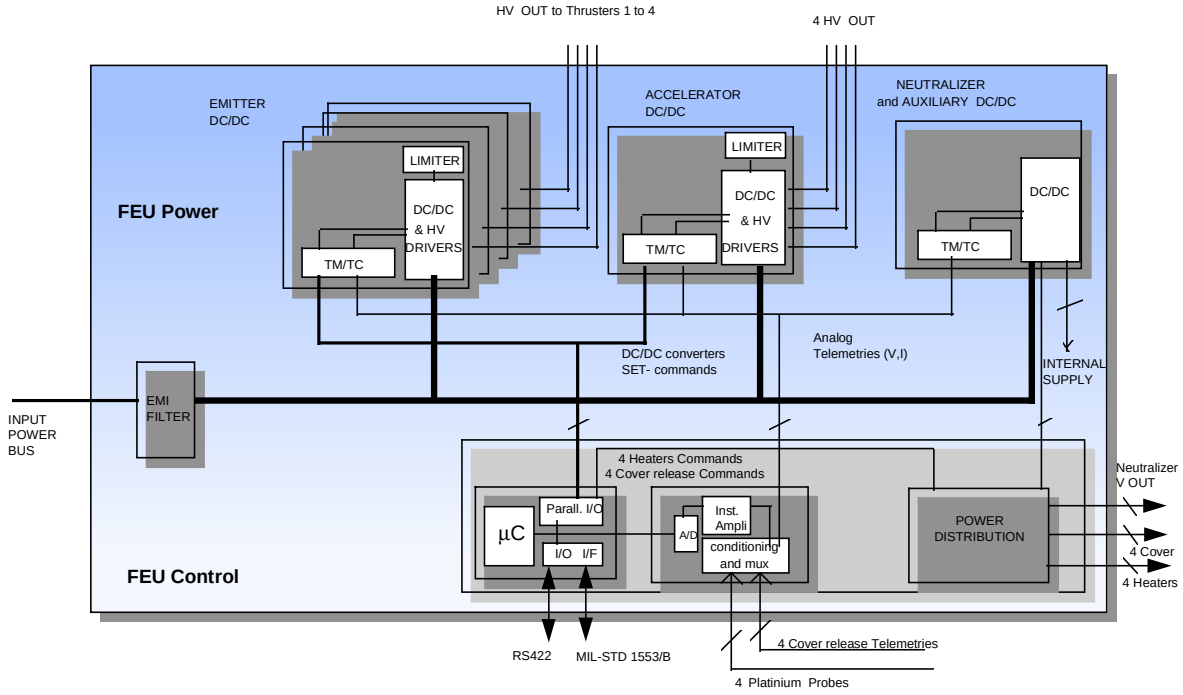

Figure 4.8 Block diagram of the FEEP Electronic Unit

EMITTER HVPS. The Emitter HVPS provides a positive high voltage programmable in the range *3KV* to *5KV*. Current specifications are:

Input voltage range	*24* to *28 V* (TBC)
Output voltage range	*3KV* (min), *5KV* (max.)
Output voltage stability	< *1.5V*
HV max. ripple	Less than *1.5V*
HV load	min load: no load max. load: *300 µA*
Programmability	Digital commands.
Output protection	Over current protection < *2mA*
Dynamic performance	The output voltage shall vary from *3KV* to *5.5KV*, sinus wave *2Hz*., i.e. the converter bandwidth shall be at least *20Hz*

The required dynamic performances can cause an additional power dissipation. In fact the low output ripple requires filter capacitance. This capacitance shall be charged and discharged at 2Hz. The additional needed output current is given by:

$I = CdV/dT_{max} = 2\pi fCA$
For $C=10\ nF$, $A=1.5\ KV$, $f=5Hz$ $I=300\ \mu A$

Additional power dissipation:

$P = fC(V_1^2 + V_2^2)$
for $C=10\ nF$, $f=2Hz$, $V_1 = 5KV$, , $V_2 = 2KV$ $P=0.4\ W$

ACCELERATOR HVPS . The Accelerator HVPS provides a negative high voltage programmable in the range *3KV* to *5.5KV*. The current specifications are:

Input voltage range	*24* to *28 V* (TBC)
Output voltage range	*-3KV* (min), *-5.5KV* (max.)
Output voltage stability	< *1.5V*
HV max. ripple	Less than *1.5V*
HV load	min load: no load max. load: *100 μA*
Programmability	Digital commands.
Output protection	Over current protection < *1mA*

During flight operations the Accelerator voltage will be set at a constant value and propulsor thrust controlled by means of the emitter voltage, being the ions emission related to the total voltage difference between the two. For the above reason only one Accelerator HVPS can be used for a cluster of 4 thrusters, and then all the thruster accelerator will be permanently connected to the positive voltage which will be maintained ON during the mission. This solution will save mass and volume with a small drawback of a permanent power consumption estimated in about *0.5W*.

CONTROL ELECTRONICS. The Control Electronics provides the interfaces to the Payload Data Processor and control the main thruster parameters such as:

- Emitter Power Supply Output Currents and Voltages.
- Accelerator Power Supply Output Current and Voltage.
- Neutralizer Power Supply Output Current and Voltage.
- Propellant temperature monitor.
- Propellant heater control.

PROPOSED SOLUTION. The overall propulsion system for GG foresees 8 thrusters, in two clusters. Each cluster is powered and driven by an electronic unit FEU (FEEP Electronic Unit). The Emitter and Accelerator HV Power Supply will be based on the well known and tested Topology constituted by a Flyback converter followed by a Cockcroft-Walton multiplier. Due to the great accuracy required on the output voltage, feedback shall be taken directly to the output, moreover matched resistor HV divider, precision operational amplifiers, stable voltage reference are needed to insure the requirement. The Power Supply HV parts shall be completely encapsulated and shielded to prevent EMI problem which are critical for the experiment. A block diagram of the Emitter power supply is given in Fig. 4.9. The power needed by the neutralizer will be provided directly by the main DC-DC converter which provides power to the control circuitry

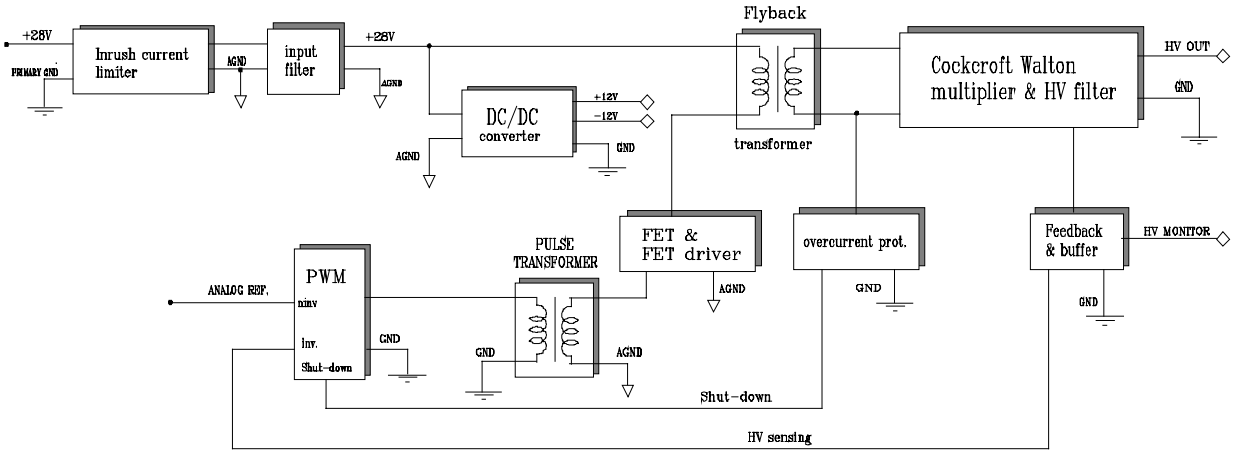

Fig. 4.9 Emitter High Voltage Power Supply

CONTROL SYSTEM. The control system is in charge of:

- Enabling the primary circuits of the 4 Emitters and 1 Accelerator HV Power supply, by means of dedicated primary enable commands
- Pre-setting the HV power supplies to the minimum operational voltage via a dedicated Power Enable Commands.
- Providing programming ward (by means of a shared parallel bus) to the five HV power supplies.
- Switch on-off function for the heaters and neutralizer
- Acquiring all current, voltage and temperature monitor.

The control system will be based on a general purpose RISC micro controller design

BUDGET. A preliminary estimate of the mass, dimensions and power consumption is given hereafter. Mass and dimension estimates are based on the assumption that 8 thrusters, and therefore two electronic units, are needed. Each unit will house four Emitter HV supplies, one Accelerator HVPS, Neutralizer and control and monitor electronics . The mass of each unit is *5.5 kg* (hence *11 kg* total) and the dimensions are: *250x140x200 mm* (each unit)

The power budget is strongly dependent on the number of thrusters which are activated at the same time and on the required power to heat the neutralizer and the emitter. A preliminary estimate is *30 W* for each unit assuming that 2 thrusters are activated simultaneously at the minimum thrust.

4.3 PAYLOAD ELECTRONICS

The GG Payload Electronics is composed by two major sub-systems: The Payload Control Electronics (PCE) and the Payload Data Processor (PDP). The former is in charge of performing active damping to the PGB and test masses and performing data acquisition from the sensors, while the latter does processing of data received from the Payload Control Electronics, TLC/TLM management, S/C interface and FEEP thrusters actuation for drag free control.

4.3.1 PAYLOAD CONTROL ELECTRONICS ARCHITECTURE

The purpose of the GG Payload Control Electronics is to perform the EP violation measurement, detected as a differential displacement between the two test masses, and to provide active damping against potentially unstable spurious motion (whirling) of the three suspended bodies (PGB and test masses). The active damping will be performed via a closed loop system based on capacitance sensors for positions determination of the body to be damped and electrostatic active dampers as actuators. The following paragraph provides an overview of the P/L Control Electronics sub-system architecture, highlighting the identified critical areas.

Fig. 4.10 shows the GG P/L Control Electronics block diagram; two separate sub-systems can be identified:

i) the PGB Control for PGB active damping conditioning purposes; located outside the PGB, it collects data related to the PGB displacement with respect to the spacecraft and performs active damping providing the electrical power to the electrostatic actuators.

ii) The Experiment Control Electronics, the purpose of which is to measure the EP violation and to provide active damping to the test masses, using the same approach as used for the PGB. It should be located inside the PGB.

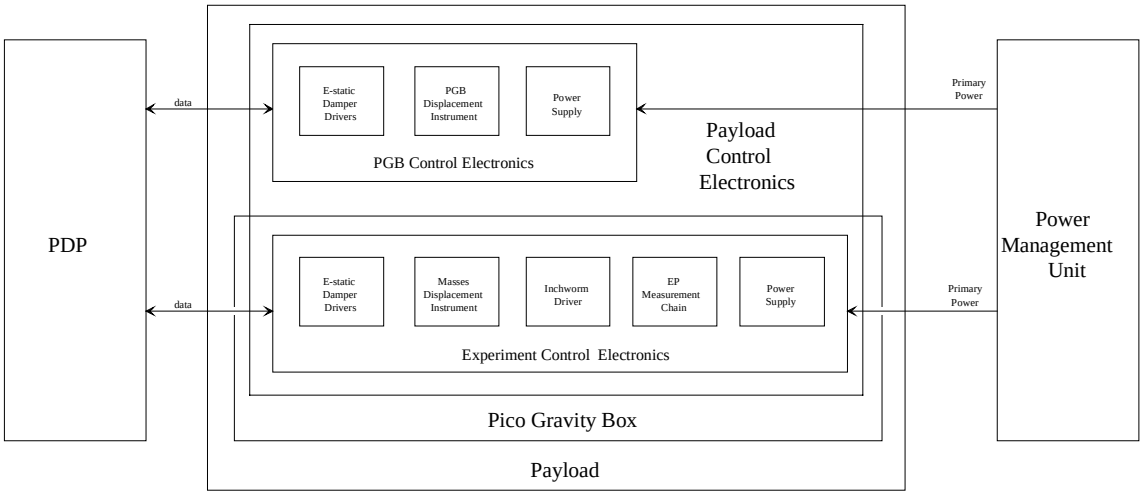

Figure 4.10 GG Payload Electronics

This architecture was identified with the specific aim to minimize the number of wires crossing the PGB springs; using a serial interface (RS-422 or similar) the number of the wires can be reduced to 6 (3 through each PGB spring): power supply (2), RX data (2) and TX data (2).

For further wires reduction, other solutions were investigated (power supply through the springs but data modulated on an RF carrier; battery located inside the PGB, charged through a magnetic coupling and data transferred across an optical interface) but they were discarded due to the serious electrical and/or mechanical drawbacks.

PGB CONTROL ELECTRONICS. The overall sub-system is represented in Fig. 4.11; the PGB displacements along the X and Y axis are detected by the PGB Control Electronics by measuring the capacitance variation between pairs of plates around the PGB. Whirling motions are detected by comparing the upper and lower capacitance plates 'belts'. On the same principle, the displacements along the Z axis are detected by the capacitance plates located on the PGB top and bottom.

In the proposed architecture, the same capacitance plates are used as Sensors and as Active Dampers. An alternative way foresees separate sensor/transducer plates, in each group of four capacitors, two used as sensors and the other two as actuators.

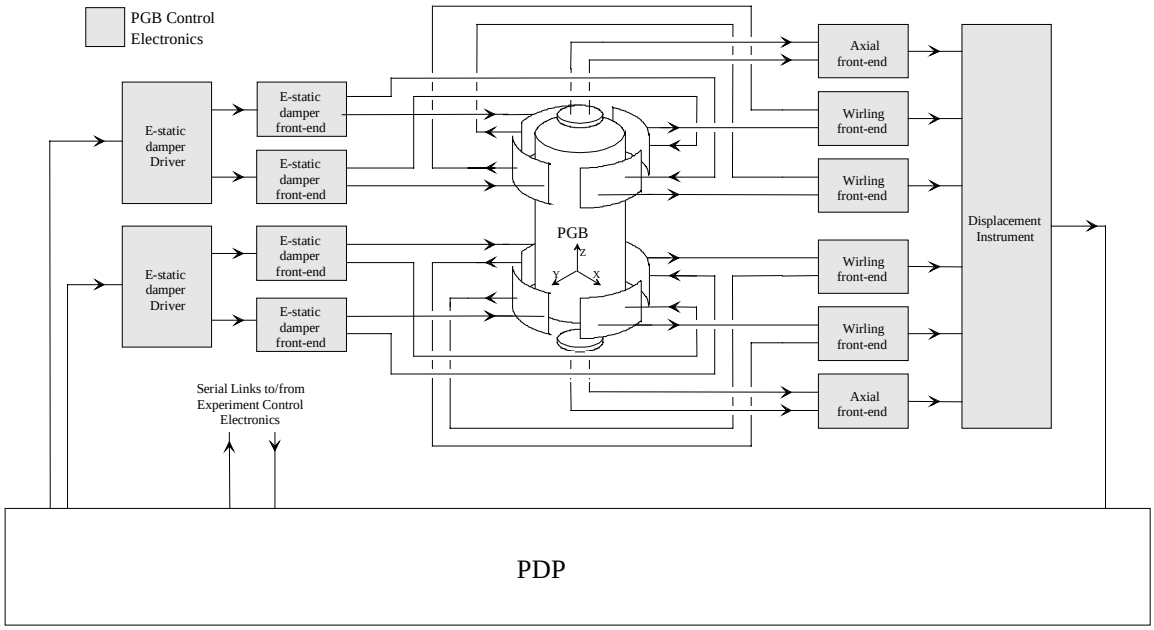

Figure 4.11 PGB Control Electronics

WHIRLING AND AXIAL DISPLACEMENT MEASURING INSTRUMENT: this instrument must determine the PGB displacements along the three axes; starting from the variation of the capacitance plates value, it must generate a numerical value proportional to the PGB displacement. These values are transferred to the PDP for further processing (Active Dampers output value calculation and telemetry to ground).

The capacitance variation allows to achieve the measurement resolution ($0.01\ \mu m$) imposed to the acquisition system; the GG instrument design will be based on well established guidelines and techniques used in laboratory instruments that provide, without any particular problem, the required accuracy.

ELECTROSTATIC DAMPER DRIVER: starting from the PGB position, determined by the dedicated instrument, the PDP will evaluate the magnitude of the force that must be applied to the PGB through the Active Electrostatic Dampers.

This parameter will be transferred (through a serial line) to the Electrostatic Drivers that generate the voltage applied to the capacitance plates.

It will be possible to modulate the force applied to the PGB by means of a programmable voltage generator able to generate up to $1\ kV$ with 255 steps resolution.

EXPERIMENT CONTROL ELECTRONICS This sub-system will measure the differential displacements and provide active damping to the test masses. The operating principle applied for the Test Masses active damping is similar to the one used for the PGB and previously explained.

The scientific chain will include a displacement sensor based on a capacitance detector much more sensitive than that used for the active damping loops. Two identical scientific chains are foreseen on orthogonal axes.

The architecture of the the Experiment Control Electronics, whose architecture is represented in Fig. 4.12. Note that as a baseline approach the same capacitance plates are used as Whirling Sensors and Active Dampers, or as two different pairs in each group of four capacitances.

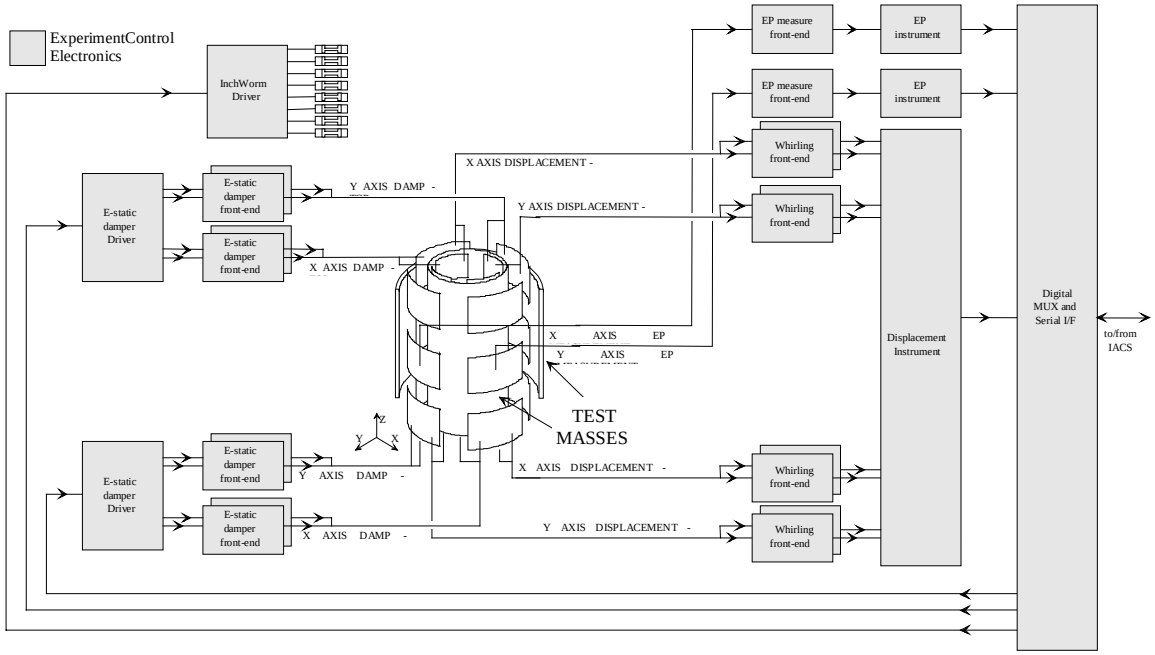

Figure 4.12 Experiment Control Electronics

WHIRL SENSING: on the same principle as the PGB, the position of each Test Mass with respect to the PGB will be monitored through eight capacitance plates located on the top and bottom of the Test Mass itself, measuring its displacements along the X and Y axis.

The capacitance variation provided by the capacitance *plates* ($C \approx 3\ pF$, $\Delta C \approx 3 \cdot 10^{-3}\ pF$ @ $1\ \mu m$) is of the same order of magnitude as that for the PGB; as baseline an instrument identical to the one used to determine the S/C-PGB displacement will be used for this purpose.

ELECTRO-STATIC DAMPER DRIVER: the force that is to be applied to the Test Masses will be computed by the PDP on the basis of the measured positions and then translated into a voltage to be supplied to the capacitance plates by these drivers.

In order to minimize noise interference between the Active Dampers and the Scientific Measurement Chain, an operating voltage lower ($\leq 300\ V$) than the one used externally to the PGB has been selected. Like the external damper drivers, these too will be 255-steps programmable devices.

INCHWORM DRIVER: used to adjust the capacitance plates position. The design of these drivers will be based on well established techniques used in Scanning Tunneling Microscopy (STM) and Atomic Force Microscopy (AFM) applications.

A commercial inchworm controller can easily achieve $10\ Å$ resolution while a high-performance inchworm controller can achieve a resolution of $0{,}6\ Å$ (Chen X. *et al.,*1992).

In the proposed architecture, one driver (or two if required for symmetrical operation) switched between the inchworms is foreseen.

EP MEASUREMENT CHAIN: this instrument must measure the differential displacement between the Test Masses due to the EP violation, which is the purpose of the GG mission.

This measurement chain must possess extremely high sensitivity as the expected differential displacement of the two test masses related to an EP violation of one part on 10^{17} is about $0.58\ pm$ (pico-meters). The above sensitivity requirement is extremely challenging, comparable or beyond what is achieved by measurement techniques such as laser interferometry. A well established laboratory technique for non-cryogenic subnanometric displacement measurement is based on the use of balanced capacitive bridges (Jones R. *et al.*, 1973); the same approach has then been chosen the EP measurement in the GG mission.

A block diagram of the foreseen EP detector arrangement is shown in Fig. 4.13.

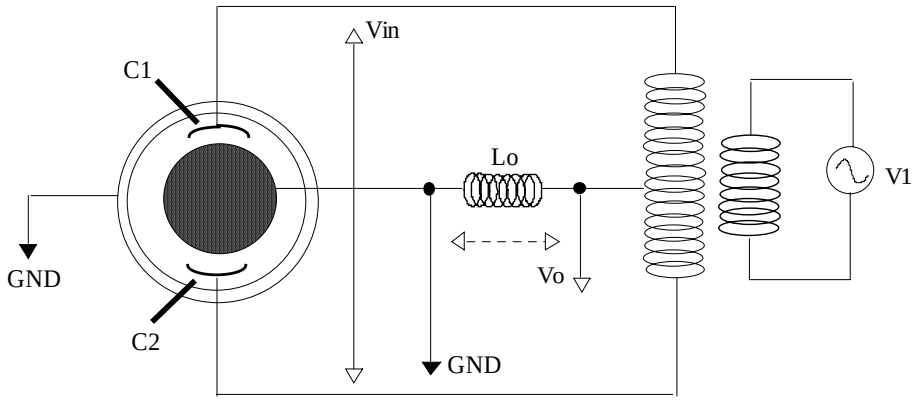

Figure 4.13 EP Measurement Chain with an LC bridge. Another option (capacity bridge) is shown on Fig. 3.10 and is currently mounted and in use in the GGG prototype.

The two test masses *A* and *B* are assumed to be at ground potential, the plates in between are the detecting elements. A high stability ratio-transformer is used to supply the detecting plates, also forming a moderately high *Q* resonant circuit.

The *V1* generator will be the output of a local oscillator running at the bridge resonating frequency F_0. The value of this resonating frequency F_0 will be driven by a trade-off between various constraints: higher frequencies are preferred in order to reduce the *1/f* noise contribution and with the aim of having smaller sizes coils, while lower frequencies are preferred in order to avoid speed constraints on the electronic components. Suitable values of F_0 seem to be between *10 kHz* and *1 MHz*.

Making some simplifying assumption it can be shown that the output signal V_0 from the above circuit is given by the following expression:

$$Vo = Vin \cdot Q \cdot \left[\frac{(C1 - C2)}{2(C1o + C2o)} \right] \tag{4.1}$$

where *C1o* and *C2o* are the "nominal" values of *C1* and *C2* when the system is perfectly centered (no differential displacement). The V_0 signal will be sinusoidal with the same frequency as the driving signal V_1, its amplitude will be modulated by the (*C1-C2*) term.

If the measuring plates are well placed just in the middle of the gap between the test masses with an accuracy of the order of some *1.9 μm* (see Sec. 2.2.1) (using the inchworms) the *(C1-C2)* term is dominated by the differential displacement between the plates, as is the effect expected from an EP violation. In such a situation the EP-related modulating signal *(C1-C2)* as function of time is a periodic signal at the same frequency as the satellite spin *(2 Hz)* modulating the *Vin* carrier of frequency F_0.

With the present mechanical design data the expected differential displacement between the masses is estimated to produce a voltage V_0 with an amplitude of the order of *2nV*. The EP violation signal is then obtained as a sine wave carrier with frequency F_0, amplitude-modulated by a *2 Hz* sine wave with *2 nV* amplitude. The detection and measurement of such low-level signals demands (apart from a carefully design of the low noise preamplifier) the use of a synchronous detection technique, that in this application is simplified by the fact that we can use the local oscillator itself as reference signal. Fig. 4.14 shows a high-level block diagram of the foreseen electronic chain.

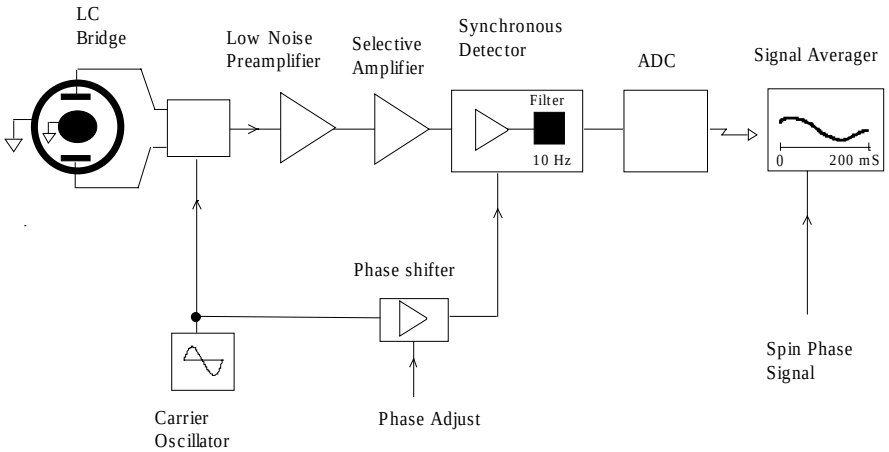

Figure 4.14 High Level Block Diagram for the EP Electronic Chain

In the following we give some details of the various stages of the chain, highlighting the most important features.

The EP detector is constituted by the LC bridge described in the previous paragraph. Particular care should be devoted to the physical connection between the detecting plates and the other components of the bridge as these connection will introduce a certain amount of disturbing effects such as non-stable stray capacitance and noise pick-up. A rigid coaxial connection (like an RF-plumbing) may be adopted to limit above disturbances. The implementation of above connection should also be very symmetric in order to avoid the introduction of unwanted differential "offset" signal. An "ovenised" approach could also be followed so as to operate the bridge in a highly stable thermal environment in order to stabilize all parasitic influences.

As shown in the above diagram, the first stage after the LC bridge is a "low noise amplifier" whose purpose is to provide an impedance and signal level matching between the detector (LC bridge) and the following stages. The design of this amplifier will use state-of-the-art low noise design, a goal of $10^{-7}\ pF/\sqrt{Hz}$ equivalent input noise spectral density has been reached in recent work and will constitute the design starting point.

The stage following the preamplifier will be a selective amplifier having high gain (*120-140 dB)* and a very narrow bandwidth (some hundreds of *Hz*) centered around the carrier frequency F_0 in order to limit noise components amplifications. This stage will be an *AC*-coupled multistage in order to avoid offset amplification along the chain. The output of the selective amplifier will be put at the input of a synchronous detector locked on a phase-shifted replica of the local carrier F_0.

The synchronous detection technique is commonly used when a periodic signal of known shape is to be extracted from noise, the output of this stage will be a low frequency signal whose amplitude follows that of the amplitude-modulated carrier i.e. proportional to the differential mass displacement in the detector. The phase shift will be adjustable on board in order to maximize the circuit sensitivity. The *2*-phase synchronous demodulation circuits built and used for this purpose in the GGG prototype are shown in Fig. 3.11.

The signal at the synchronous detector output is then A/D (analog-to-digital)converted with 16 bit resolution for serial transmission outside the PGB for further processing. The circuit built for this purpose and used in the GGG prototype is shown in Fig. 3.12. The foreseen conversion sample rate is *20 Hz*. The last stage of the EP detection chain could be a "signal averager" (maybe S/W implemented inside the PDP). The purpose of this stage is to average the EP data samples synchronously with the spin phase signal (from attitude sensors) in order to extract the actual EP violation signal from possible other effects leading to differential test mass displacement. The operation of the signal averager, synchronous to the spin phase, can be viewed also as a second synchronous detector locked at the spin frequency and indeed could also be realized by H/W in that way.

The gain of the overall detecting chain will be set in order to have a full-scale of $\pm 50\ \%$ around the 'centre' position. Proper signal for upper and lower out-of-scale will be generated in order to allow the initial centering of the measuring plates by means of the inchworms. A certain amount of on board gain setting could also be provided.

4.3.2 PAYLOAD DATA PROCESSOR ARCHITECTURE

The Payload Data Processor (PDP) will be an electronic unit in charge of performing all the tasks related to payload data processing, payload management and Drag Free Control (DFC). Its main tasks will therefore be:

- TC reception from spacecraft and decoding
- Payload timelines and command execution
- Science data collection and formatting
- TM packetisation and transmission to the spacecraft
- Drag free control algorithm computation
- Commanding of the FEEP power supplies

The PDP computer will be based on a proven design and flight qualified hardware. The proposed processor is the TSC21020, a powerful *32 bit* DSP functionally and electrically equivalent to the well known Analog Devices ADSP21020, but realised in radiation tolerant technology and fully qualified for space applications by Temic. The processor has been selected mainly for the following characteristics:

- consolidated design (its development has been supported by ESA)
- very high processing power (*20 MIPS* and up to *40 MOPS*)
- relatively less expensive that other comparable processors
- good performances in terms of radiation immunity (latch-up free and very low SEU rate)
- fully qualified for space.

Although DSP processors like this are targeted to computationally intensive applications, the TSC21020 performs very well also in data handling tasks. Its choice is therefore adequate for the PDP computer where both the two types of tasks are present, giving a quite large safety margin in the available processing power. A general block diagram of the proposed PDP unit is shown in Fig. 4.15.

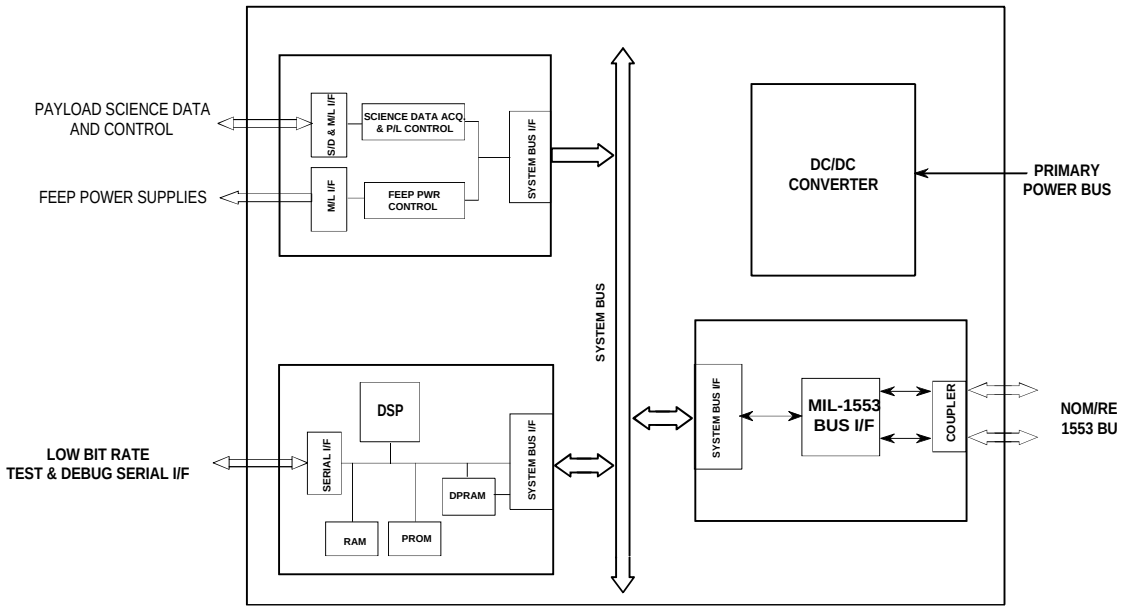

Figure 4.15 Payload Data Processor block diagram

A brief description of the overall architecture of the PDP and of the various blocks is given below.

ARCHITECTURE. The PDP electronic unit is composed by four boards: three digital boards for data processing and one DC/DC converter for units power supply. The digital boards are interconnected by a *16 bit* parallel system bus (the Laben standard SBUS90), which allows to exchange data at high speed among master and slave boards.

MICROCOMPUTER BOARD. This board performs the tasks of science data processing, P/L control, DFC algorithm, FEEP power supplies control and TM/TC packets handling. A block diagram is shown in Fig. 4.16.

The board is based on the Temic 32 bit DSP TSC21020. The processor is equipped with 8 Bytes of PROM memory containing the bootstrap program and the emergency/maintenance code, *512 Bytes* of non volatile EEPROM memory storing the application SW, *128 Kwords* (*48 bit* per word) of static RAM for program memory and, optionally, up to *256 Kwords* (*32 bit* per word) of static RAM for data memory. At power-on, the bootstrap program stored in PROM copies the application program from EEPROM to program RAM, from where it is actually executed. The execution from program RAM instead of EEPROM allows a faster execution and the possibility of temporary patches of the code. Permanent patches/upgrades of the application code are in any case possible, even in flight, by rewriting the EEPROM content by maintenance code residing in PROM.

All the RAM can be optionally protected from soft errors induced by heavy ions radiation which are normally present in space, by means of an error detection and correction circuit (EDAC) able to automatically correct any single bit error in each RAM word and detect double bit errors without CPU intervention. If a periodic scrubbing of the RAM content (i.e. reading and rewriting each word) is done, the probability of erroneous reading of the RAM becomes practically zero even using memory devices less resistant to radiation but cheaper. A trade off is generally made depending on mission requirements and orbit characteristics, taking also in account that the EDAC circuits require additional memory and decrease the CPU speed.

The board includes, in addition to the peripherals already included in the DSP device (timer, interrupt controller, etc.), a serial asynchronous full-duplex channel with RS422 interface, which can be used for testing and debugging as well as for application purposes. It also

includes an interface to the system bus with master and slave capabilities, which allows the CPU to communicate with the other boards of the unit.

Additional peripherals or memory can be added directly to the microcomputer board by means of mezzanine boards. Program test and debugging are possible via the JTAG port of the DSP and the access to the program memory bus available on a specific test connector.

MIL-1553 board. The MIL-1553 board allows to interface the PDP unit to the spacecraft data bus which is a MIL-STD-1553 bus. Core of the board is a space qualified hybrid device which implements the functions of Remote Terminal (RT) and Bus Controller (BC) interfacing a generic microcomputer system on one side and a pair of nominal/redundant MIL-1553 busses on the other side. The board also includes an interface to the units system bus by which the DSP can communicate with the hybrid to send to, and receive from, the spacecraft TM/TC packets over the 1553 bus.

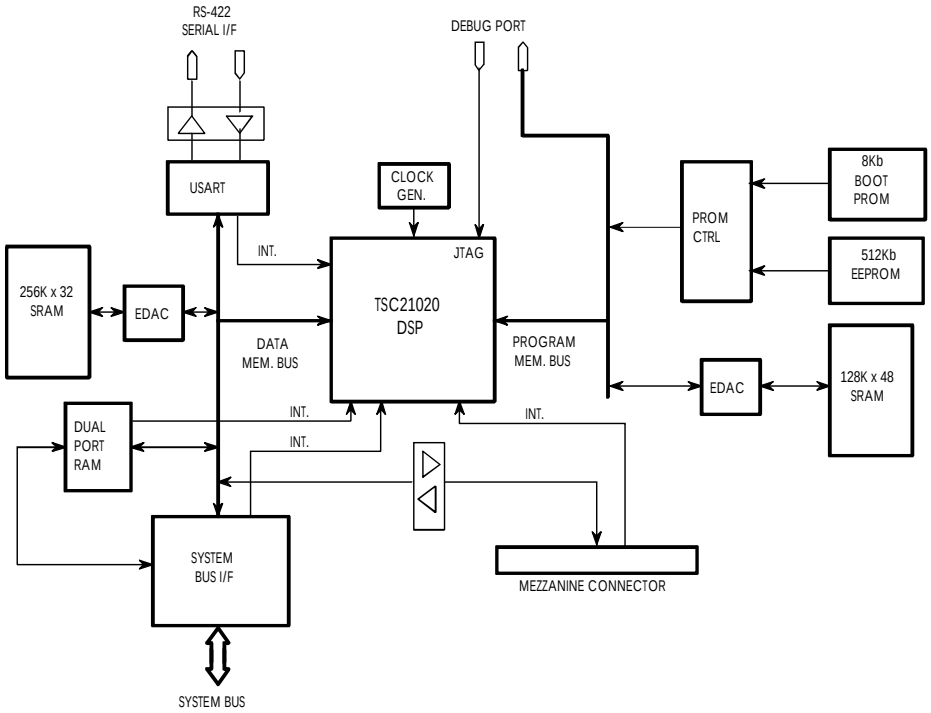

Figure 4.16 Microcomputer board block diagram

FEEP AND PAYLOAD INTERFACE BOARD. This board interfaces the payload in order to control the payload instruments and to receive scientific data. It also interfaces the various power supplies of the FEEP thrusters to control the thrust according to the Drag Free Control algorithm results.

Both interfaces are of digital type, in the style of the standard Memory Load (ML) / Serial Digital (SD) serial channels. These interfaces are accessible by the microcomputer board via the system bus.

The payload interface is composed of one outgoing ML channel for payload commanding and one incoming SD channel for science and housekeeping data acquisition.

The FEEP interface is composed by one ML channel for Emitter HV power supply control and 6 ML channels for Accelerator + Neutralizer power supplies control (one for each thruster).

This is the baseline configuration. Additional simple interfaces (e.g. thermistors or analog monitors acquisition) can be easily added in case of need.

4.4 THERMAL CONTROL OF THE SCIENTIFIC PAYLOAD

This paragraph contains a brief description of the thermal control solutions developed by LABEN in order to satisfy the scientific requirements of the GG mission.

4.4.1 THERMAL REQUIREMENTS

The principal thermal requirements for the scientific P/L are concerned with the test bodies and are the following:

- high temperature uniformity on each test mass
- test masses temperature drift $\leq 0.2\ °C/day$
- test masses temperature oscillations at orbit period (induced by eclipses) even smaller.

4.4.2 THERMAL CONTROL SOLUTIONS

The orbit of the GG satellite is such that it spends almost half of its time in eclipse (shadow of the Earth) and half in sunlight: equilibrium temperatures in the two different conditions may differ by several tenths of degrees. Due to the fast spin of the satellite, the temperature has azimuthal symmetry, but temperature gradients between the dark side and the lightened side of the spacecraft (radial gradients) may be very large. Anyway, the temperature gradients can be made negligible if the satellite is properly insulated: in fact, the temperature of the payload becomes stable if we are able to reduce the heat flowing from the inner surface of the satellite towards PGB and Test Masses. Some design solutions have been developed and are based over a 'passive' thermal design. These solutions have been studied considering a preliminary satellite configuration as shown in Chap. 2.

All the models and analyses developed by LABEN show the feasibility of the solutions proposed for the thermal control.

The P/L thermal control is based on a thermal insulation as large as possible among test masses, PGB and S/C and on vacuum inside the satellite, so that energy is transferred only by radiation among the large surfaces inside the satellite, and not by thermal conduction. Thermal conduction is limited to the small connecting elements between Spacecraft and PGB, and between the PGB and Test masses: the smallness of the connecting elements makes it feasible to reduce the heat flux inside them. Moreover, only the preamplifiers are located at the PGB level: the rest of the electronics is located at the s/c level.

In order to reach the correct level of thermal insulation, the inner surface of the S/C and the PGB surfaces are covered by MLI with an effective emissivity $\varepsilon_{eff} = 0.01$, which corresponds to about 20 layers MLI tape. Moreover, the test masses have an emissivity equal to 0.05 which is due to their polished surfaces.

The heat transfer can be schematized in the following way (note that the solar panels are located around the lateral surface of the satellite, not in the top and bottom covers). The radiation (Sun, Earth albedo and Infrared) impinges on the external surface of the satellite where it is absorbed by the solar cells; the insulating shell covering the inner surface of the spacecraft strongly reduces the amount of energy which can then be radiated towards the PGB. Assuming that x is the radial direction, the temperature across the insulating shell can be described along x by the simple model

$$T(x) = T_0 + (T_E - T_0) \cdot e^{-x/d} \tag{4.2}$$

with T_0 the satellite initial temperature, T_E the external environmental temperature, and d the penetration depth of the insulating shell (d < thickness of MLI). The temperature of the inner surface of the spacecraft depends on time as

$$T(t) = T_{eq} + (T_0 - T_{eq}) \cdot e^{-t/\tau} + \Delta T sin(\omega_{orb} t) \quad (4.3)$$

with τ the time scale of thermal inertia of the insulating shell, T_{eq} the "equilibrium temperature" of the spacecraft, ΔT the residual orbital oscillation of the temperature due to the eclipse-sunlight transitions. The energy flow from the inner surface of the spacecraft to the external surface of the PGB can only be radiative, due to vacuum inside the satellite. The temperature difference between the inner surface of the spacecraft and the external surface of the PGB is thus minimized, having reduced to the lowest possible level the exchange of energy. In a similar way, radiative energy transfer takes place between the inner surface of the PGB and the external surface of the Test Masses. In this way thermal gradients on the test masses can be reduced and thermal stability ensured. As for the top and bottom covers of the satellite, they are coated with reflecting material in order to reduce heating, and the previous technique is applied in order to reduce thermal exchange with the inner part of the spacecraft.

Due to the high insulation of the spacecraft and to the high thermal inertia τ of PGB and test masses, the time required to reach the steady state may be very long if the initial temperatures differ by several degrees from the "equilibrium temperatures" T_{eq}. A guideline for this design is therefore for the initial temperatures of GG components to be as close as possible to the equilibrium ones to make the drift as small as possible, as shown below.

4.4.3 ESTIMATE OF THE ORBITAL HEAT FLUXES

In order to begin a quantitative study of the solutions described above, it is necessary to estimate the heat fluxes absorbed by the GG vessel while orbiting around the Earth; heat fluxes which depend on the GG orbital parameters. To perform feasibility studies of the thermal design, the GG orbit has been considered with zero declination of the Sun. This is a worst case analysis for GG because of the largest gradients between the covers and the cylindrical body of the GG vessel.

In order to determine quantitative results, an Esarad model of the GG vessel has been developed. The model contains 24 nodes:

- Geometrical configuration :
  - cylinder: *130 cm* height, *100 cm* diameter,
  - spin axis: z (principal axis of inertia),
  - spin period: *0.5 sec* (ν = *2 Hz*),
- Thermo-optical surface properties (α = absorption coefficient, ε = emissivity):
  - cylinder: α = *0.73* ; ε = *0.83* (solar cells properties),
  - covers: α = *0.35* ; ε = *0.70* .

The orbital data used in the calculations are:

- Circular obit, altitude: *520 km* (orbital period *5700 sec*)
- Orbital inclination over the equator: *3°*
- GG z axis: *3 degrees* inclination to orbit normal
- Earth temperature: *257 K*
- Zero declination of the Sun

Esarad provides the power absorbed by each node of the model at various orbital positions of the satellite along its orbit (11 in our case). It is found that the power absorbed is highly uniform, as it was expected because of the fast spin.

4.4.4 THERMAL MODELS

In order to evaluate the performances of the proposed thermal design, thermal mathematical models (TMM) and analyses were developed with the Esatan software tool using the data obtained by Esarad.

With the satellite structure shown in Chap. 5, a detailed thermal model with *79* nodes was developed. By transient analyses results, a high uniformity of the temperature both for the PGB and the test masses was found, as expected. Therefore, it was decided that a less detailed (reduced) model could be used instead.

The reduced thermal mathematical model includes 17 nodes plus 1 boundary node:

- 3 nodes for the vessel
- 1 node for the PGB cylindrical body
- 3 nodes for the PGB rod, LUMs & supports
- 2 nodes for the test bodies
- 8 nodes for the electronics
- 1 boundary node for outer space.

The total electrical power considered in these simulations is $106\ W$. The nodal thermal couplings are computed taking account the estimated coupling for the detailed TMM (the detailed TMM radiative couplings were calculated by Esarad, running the Monte Carlo ray tracing module).

The conductive coupling between the PGB and the GG vessel by means of the PGb tiny springs is negligible due to the spring dimensions (see Fig. 2.5).

4.4.5 ANALYSES AND RESULTS

Both transient and steady state analyses were addressed.

Using the average heat absorbed by GG during one orbit, the equilibrium temperatures of nodes, $T_{i\text{-}eq}$, are calculated (steady state analysis). The meaning of these values is: once thermal equilibrium has been reached, the nodal temperatures $T_i(t)$ oscillate around the corresponding equilibrium values $T_{i\text{-}eq}$ (thermal equilibrium may be reached after a long time since the bodies are well insulated). The test masses have equal $T_{i\text{-}eq} = -2.7\ °C$.

Another steady state analysis was performed in order to estimate the range of variation of $T_{i\text{-}eq}$ values, due to different seasonal and climatic conditions. To do this, the following variations in the average heat flux data have been inserted in the model:

- absorbed solar heat flux variation: *5%*
- absorbed albedo heat flux variation: *15%*
- absorbed Earth heat flux variation: *30%*

The results show that the maximum excursion over $T_{i\text{-}eq}$ due to variations of the incoming energy flux on the satellite is less than $7.5\ °C$. As consequence of this, it is reasonable to demand that the GG satellite be launched with an initial temperature: $|T_0 - T_{tm\text{-}eq}| \leq 10\ °C$; where $T_{tm\text{-}eq}$ is the test masses equilibrium temperature and T_0 satisfies: $T_0 = T_i\ (t=0)\ \ \forall i$.

This condition shortens all the initial transient times and makes all drifts in temperature small. In order to verify the compliance of the design with the thermal requirements, a transient

analysis is needed. Since the temperature drift is proportional to the difference between the initial and the equilibrium temperatures, a worst case condition for the analysis is to require:

$$|T_0 - T_{tm\text{-}eq}| = 10\ °C \qquad (4.4)$$

Using data obtained from the steady state analysis, the above condition means: $T_0 = +7.3$, *(i.e.: -2.7 + 10.0)*. The time span chosen for the simulation is *30 days*. Fig. 4.17 shows the temperature evolution of the nodes corresponding to the PGB and the test masses; Fig. 4.18 shows a detailed view of the evolution of the test masses temperatures.

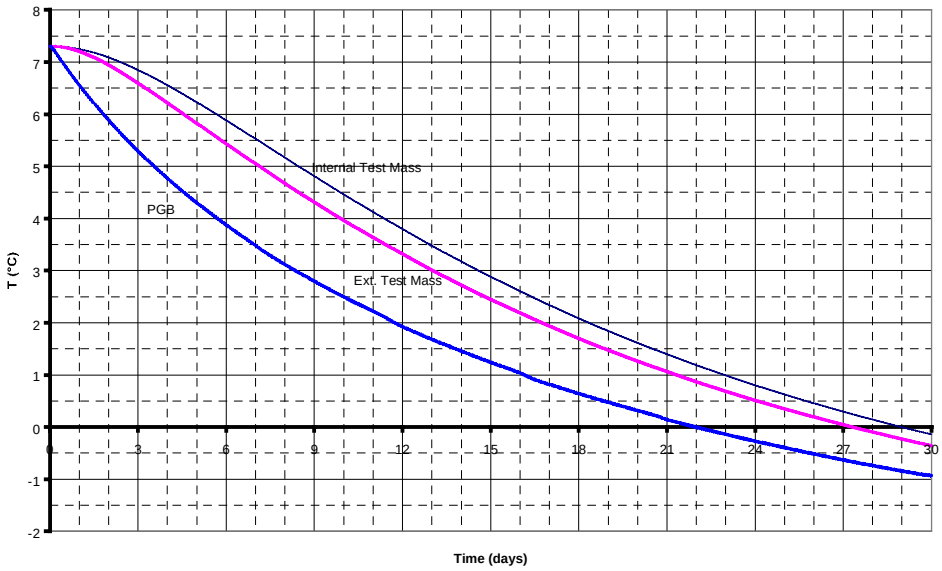

Figure 4.17 Nodal temperature drift to equilibrium

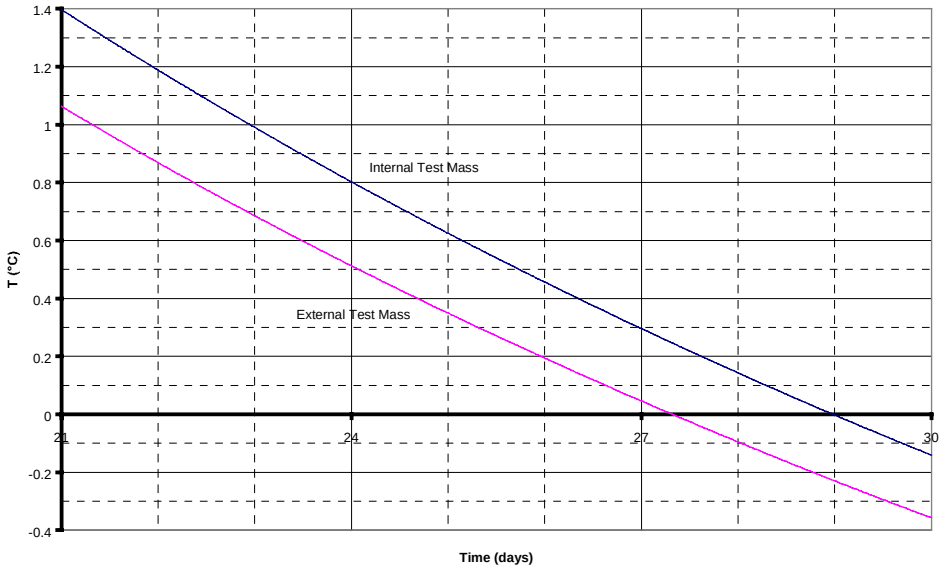

Figure 4.18 Detailed view of the time evolution of the test masses temperatures

The results of this analysis can be summarized as follows:

- PGB Temperature Drift :
  - $\Delta T \approx 0.13\ °C/day$ (evaluation for the last 5 days);
  - $\Delta T \approx 0.60\ °C/day$ (evaluation for the first 5 days).
- Temperature oscillations of PGB with orbit period (due to eclipse): $< 0.01\ °C$.
- Test Masses Temperature Drift :
  - $\Delta T \approx 0.15\ °C/day$ (for the last 5 days);
  - $\Delta T \leq 0.30\ °C/day$ (for the first 5 days).
- Temperature oscillations of Test Masses with orbit period (due to eclipse): $< 0.001\ °C$.
- The vessel $T_i(t)$ temperatures oscillate around the equilibrium values after $1\ day$

The results show that after the 21st day the test masses temperature drift is less than $0.2°C/day$.

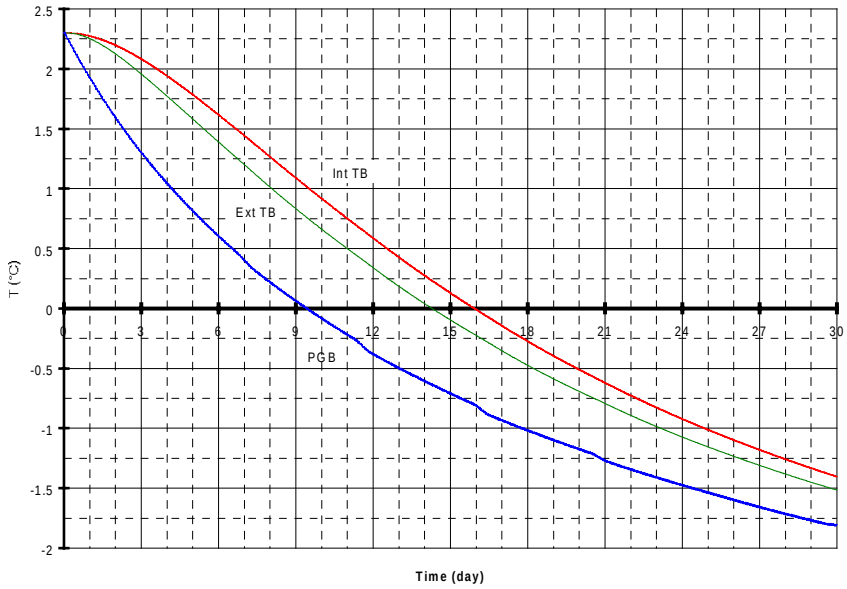

Another case has been analyzed in which: $|T_0 - T_{tm\text{-}eq}| = 5\ °C$. The results are reported in Fig. 4.19 and show that the test masses drift fulfills the requirements for the entire $30\ days$ duration of the simulation.

Figure 4.19 Time evolution of P/L Temperatures in the case $|T_0 - T_{tm\text{-}eq}| = 5\ °C$

4.4.6 CONCLUSIONS

The results reported here show that the performances of the passive thermal control proposed for the GG payload are such that the mission requirements can be met. However, there are severe limits to the maximum power that can be dissipated by the payload electronics. For this reason, only the preamplifiers are allowed at the PGB level (on the PGB tube). It is also found that –as expected– the initial deviation from equilibrium of the temperature distribution inside the PGB, rules the steepness of the temperature drift. It is therefore recommended that the initial model temperatures be as close as possible (within less than $10\ degrees$) to their equilibrium values, which is doable. As for temperature gradients along the z axis, across the test bodies and the coupling arms (shown in Fig. 2.1), a detailed numerical simulation was not carried out but conservative estimates show that the requirement for them not to exceed about $1\ degree$ can be met.

5. THE GG SATELLITE

5.1 LAUNCH REQUIREMENTS AND CONSTRAINTS

The requirements call for a low-cost launch vehicle able to inject up to $300\ kg$ into low, circular, equatorial orbit. Furthermore, to simplify the early orbit operations, an ability to deploy the satellite in a spinning mode, with the spin axis approximately perpendicular to the orbit plane, is sought.

A number of 'small' launch vehicles, potentially meeting the above requirements, is either available or in an advanced development stage. Table 5.1 shows a comparison of the characteristics, based on the information available to date. Launch into an equatorial orbit, as required by GG, needs additional investigation, specific to each launcher, since the minimum inclination is constrained by the latitude of the launch site.

	Performance @500 km		Fairing		P/L Interface		Quasi Static Loads		Min. Dynamic Requirements		C.O.G. Max. Height	Launch Cost Estimate
Launch Vehicle	Orbit Inclination	Lift Mass [kg]	ϕ [mm]	h [mm]	ϕ [mm]	Type	Lateral [g's]	Axial [g's]	Lateral [Hz]	Axial [Hz]	[mm] [1]	[M$]
VEGA SLV1	5°	600	1708	2500	937	TBD	±3	8	TBD	TBD	TBD	14
VEGA SLV2-K3	5°	1200	2000	4500	937	Bolted/ Marman	±1	8	18	30	1800	17
LMLV1-B (Athena)	28.5°	750	1984	3969	944	Continuous	±2.9	9.2	15	32	TBD	16
ROCKOT	55°	860	2260	4757	937	Continuous	±0.8	9.55	15	33	any	5-10
COSMOS	48°	1330	2200	4728	1060	Discrete	±1.6	6.8	10	25	1050	9-12
PEGASUS XL	0°	380	1118	2139	965	Continuous	+3.5 -0.6	9	20	n.a.	900	12-14

[1] Maximum lift mass considered

Table 5.1 Comparison of launch vehicle design data. The cost data in the last column (1997 status) are orders of magnitude and refer to typical launch scenarios. Cost deltas may apply for special requests, such as attitude at separation, launch dispersions etc.

For the purposes of this preliminary design exercise, the following approach was adopted.

- The Orbital Sciences Corporation Pegasus was taken as reference launcher. Pegasus has already passed a number of qualification flights and its characteristics (technical and programmatic, including cost) are sufficiently well documented. In addition, as demonstrated by the table above, Pegasus requires the satellite to comply with particularly demanding constraints (i.e., size, mass, launch loads).
- Significant margins were taken in the design, particularly in the normal modes at launch (see Sec. 5.3.5).

The approach above ensures that a design compatible with Pegasus will be readily adapted to other launchers. In particular, recent data demonstrate (as shown in the remainder of this Section and in Sections 5.2 and 5.3) that all design parameters of the VEGA launcher are less constraining, for the design of GG, than the corresponding parameters of Pegasus.

LAUNCH VEHICLE CHARACTERISTICS Some characteristics of the Pegasus XL launch vehicle are listed in Table 5.2 (ref. OSC Pegasus® Users' Guide, Release 4.0, September 1998).

Type:	Pegasus XL
Launch site:	Alcantara, Kwajalein (provided as a non-standard service)
Mass into orbit:	≈ 380 kg (520 km circular, equatorial) ≈ 370 kg (600 km circular, equatorial)
Payload dynamic envelope:	diameter 1168.4 mm (46"), height 2138.7 mm (84.2") (without HAPS[1]) height 1767.8 mm (69.6") (with HAPS)
Standard adapter interface diameter:	590.5 mm (23")
Separation system (remaining with the S/C) mass:	≅ 3.95 kg
Design limit loads & dynamic requirements:	see paragraph 5.3.1

Table 5.2 Pegasus Launch Vehicle Characteristics

The dimensions of the VEGA launcher fairing are larger than those of Pegasus; they are 2 m in diameter and 3.5 m in height (cylindrical part). The VEGA launch mass capability for the reference orbit is also much higher than that of Pegasus (over 1000 kg with the K3 version). A launcher to S/C standard interface of 937 mm (TBC) is foreseen; if that is the case, a suitable adapter must be designed for GG.

ORBIT INJECTION PERFORMANCE The Pegasus XL Users' Guide provides the following information for typical launch scenarios.

- Duration of launch phase (lift-off to separation): 2811 s (with HAPS).
- Orbit injection errors as in Table 5.3.

Configuration		perigee	apogee	eccentricity	inclination
Pegasus XL	(low)	-110 km	±18 km	0.01	±0.2º
	(high)	±18 km	+110 km		
Pegasus XL with HAPS		±19 km	±28 km	0.003	±0.05º

Table 5.3 Pegasus Launch Vehicle Injection Performance

[1] HAPS = Hydrazine Auxiliary Propulsion System

No capability for correction of injection errors will be available on board GG. An eccentricity as large as *0.01* is hardly tolerable, therefore we assume use of the hydrazine auxiliary propulsion system (HAPS).

Attitude orientation at separation: the third stage of Pegasus can spin the satellite up and provide a pre-defined orientation of the spin axis before separation. A spin up to *16.7 rpm (0.28 Hz)* is nominally provided, while rates above *16.7 rpm* are considered a non-standard service and depend on the amount of propellant left. Therefore, an autonomous system for spin-up to the required *120 rpm* must be provided by the satellite.

The typical pre-separation performance is as follows:

- spin rate accuracy: *0.3 rpm*
- angular momentum depointing: *±2 °*
- transverse angular rates: *±2 %sec*

Given these errors, the autonomous spin-up system mentioned above must also provide for correction of angular momentum depointing and damping of angular rates.

5.2 SATELLITE CONFIGURATION

The main configuration requirements are:

- cylindrical symmetry with outside diameter not larger than about *1 m*
- low area-to-mass ratio, hence as low as possible cylinder height
- easy integration of the payload (PGB with locked test masses)
- accommodation of the spacecraft equipment and payload electronics outside the PGB
- the axis of symmetry of the cylinder (spin axis) must be a principal axis of inertia.
- the moment of inertia about the spin axis (J_z) must be larger than the moments about the other principal axes (J_x), that must be about equal in magnitude, such as to realise an inertia ratio $\beta = (J_z-J_x)/J_x$ in the range of *0.2 - 0.3*
- provision of sufficient room for the equipment boxes and the solar array.

The above requirements cannot be reconciled with a structural configuration derived from the PRIMA bus. Therefore, a configuration built around the payload module (PGB) was preferred as shown in Fig. 5.3.

The structure (see Fig. 5.1 and Fig. 5.2 where the solar panels have been removed for clarity) is made up of a central cylinder and an upper and lower truncated cone. The upper cone is removable to allow the integration of the PGB with its suspension springs; the lower cone supports the launcher interface ring. The equipment are mounted on the central cylinder by means of suitable cut-outs, and to the upper and lower cone. The solar panel is divided into two pieces to make room for the equipment mounted in the central belt, including thrusters and sensors (Fig. 5.3); this solution also allows a suitable distribution of thermal covers and radiators to realise an efficient thermal control. The total height of the satellite (antennas not included) is *1.31 m; 0.93 m* in eight is allocated to the solar arrays allowing for sufficient power output. The mass distribution permits to reach a value of $\beta \approx 0.3$.

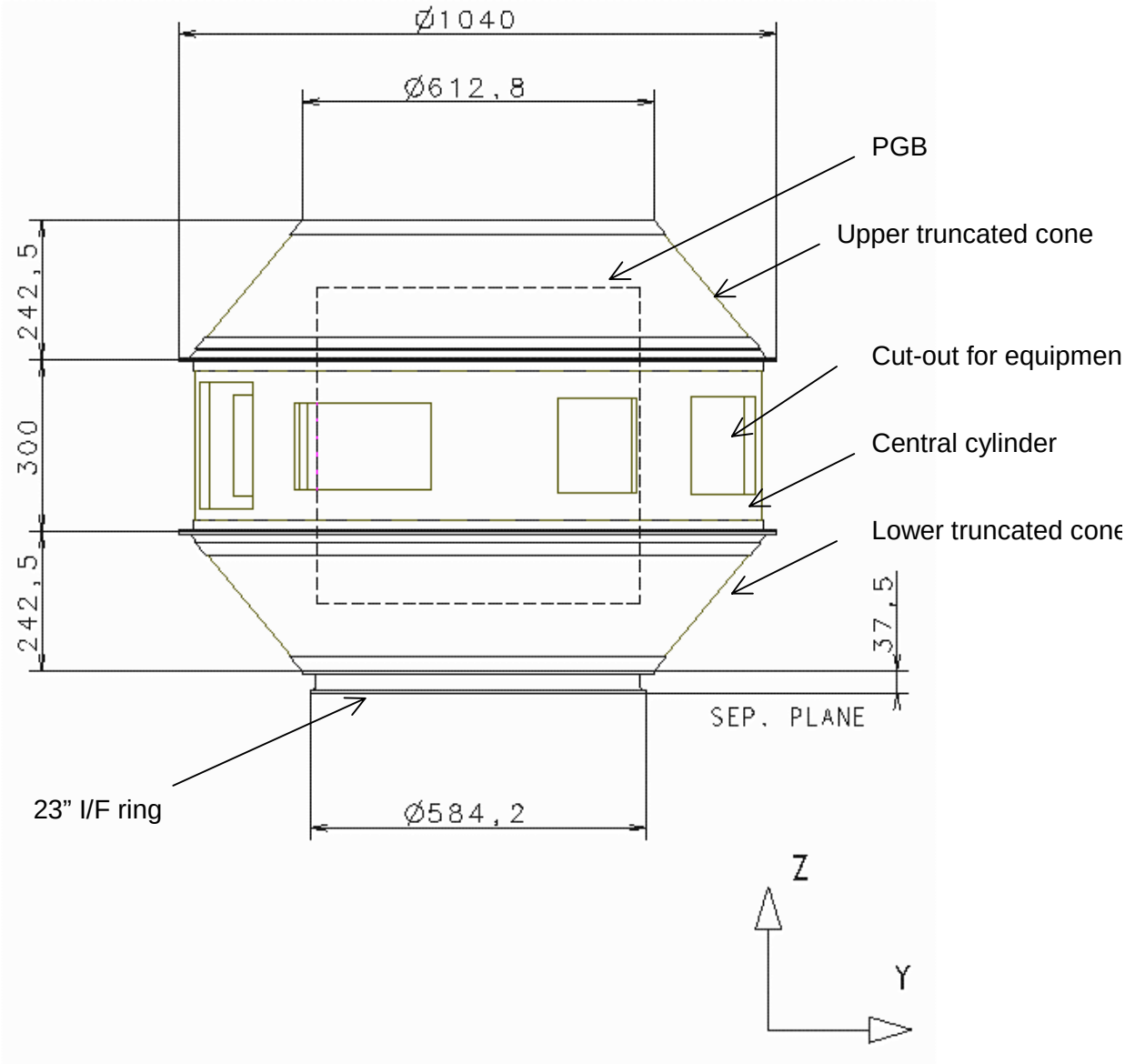

Figure 5.1 Structural configuration (side view) with solar arrays removed. The structure, completely enclosing the PGB laboratory (shown in outline), is made up of three parts: (a) central cylinder with 1 m diameter, providing cut-outs for the equipment accommodated outboards for reasons of field of view or thermal dissipation; (b) upper truncated cone, with the interface to the PGB suspension system, and (c) lower cone, symmetrically placed, hosting the launcher interface ring. (All distances in the drawing are in mm).

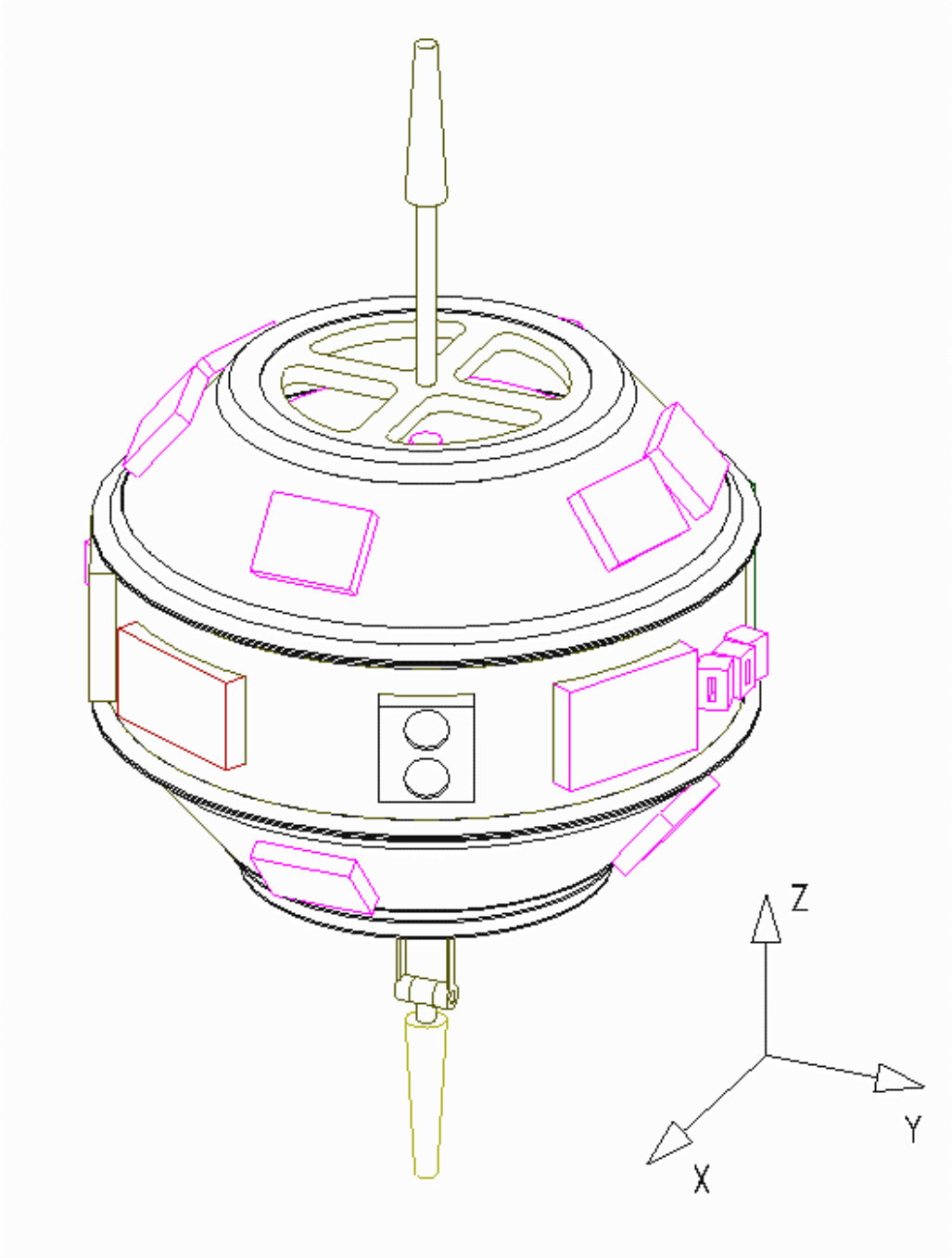

Figure 5.2 Structural configuration with solar arrays removed. This 3D view shows the accommodation of the equipment on the upper and lower cones as well as in the central cylinder, and the S-band antennas. This compact configuration results in a very stiff structure, with high frequency margins with respect to the launcher requirements.

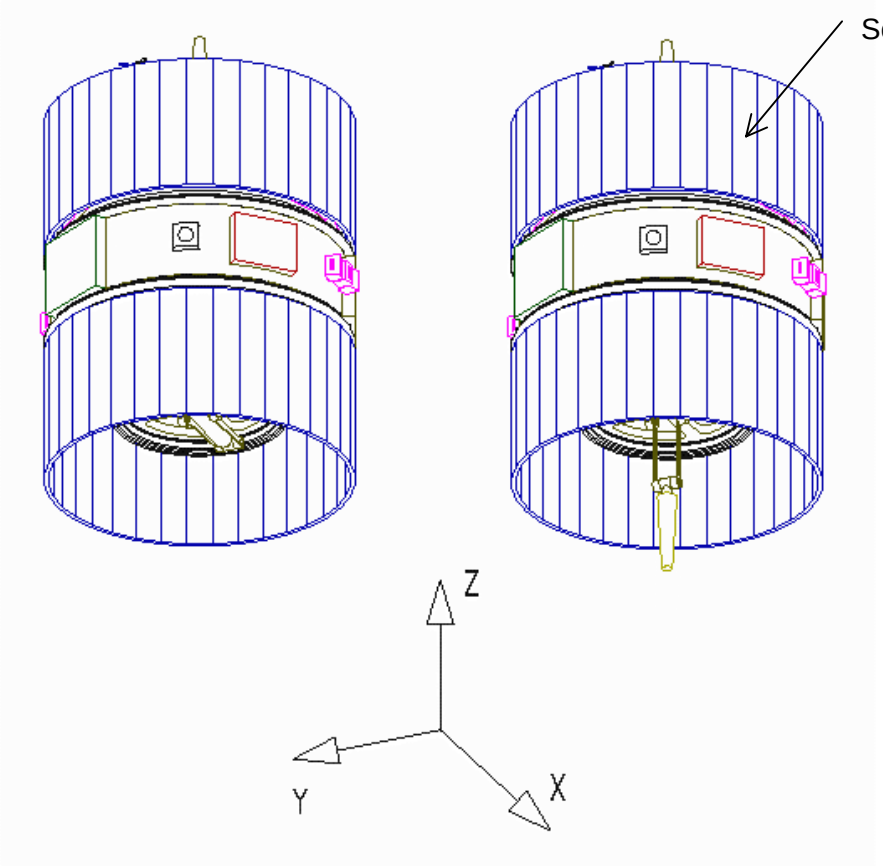

Figure 5.3 External configuration with solar panels and antennas. The picture on the left shows the stowed bottom antenna (launch configuration), and the picture on the right the deployed position. No deployment mechanism is needed for the top antenna.

The final configuration comprises, from bottom to top, the following items:

- a *23" (0.584 m)* interface ring with the launcher;
- a lower circular plate with cut-outs; it looks like a wheel with spokes;
- a lower truncated cone;
- a central cylinder with suitable cut-outs for mounting the equipment;
- an upper truncated cone;
- an upper circular plate with cut-outs; it looks like a wheel with spokes;
- a cover on the upper side of the satellite solar arrays cylinder (minimizing drag effects; on the lower side this solution is not fully applicable because of the adapter);
- two solar panels sets surrounding the outermost cylinder;
- a PGB assembly with the on-orbit suspension springs device;
- a PGB locking mechanism device to be used at launch;
- two antennas aligned with the spin axis (the one on the side of the launcher interface must be deployable).

The station of the equipment ring w.r.t. the PGB can be adjusted (thanks to the sufficient gap between the PGB and the structure in the spin axis direction), such that the centre of mass of the satellite is placed in the mid-plane of the figure of revolution (an important consideration for minimizing the torques due to surface forces).

Fig. 5.4 shows the configuration under the Pegasus fairing and Figs. 5.5a/b show the equipment configuration in the central cylinder and the layout of the FEEP thrusters in the equatorial region.

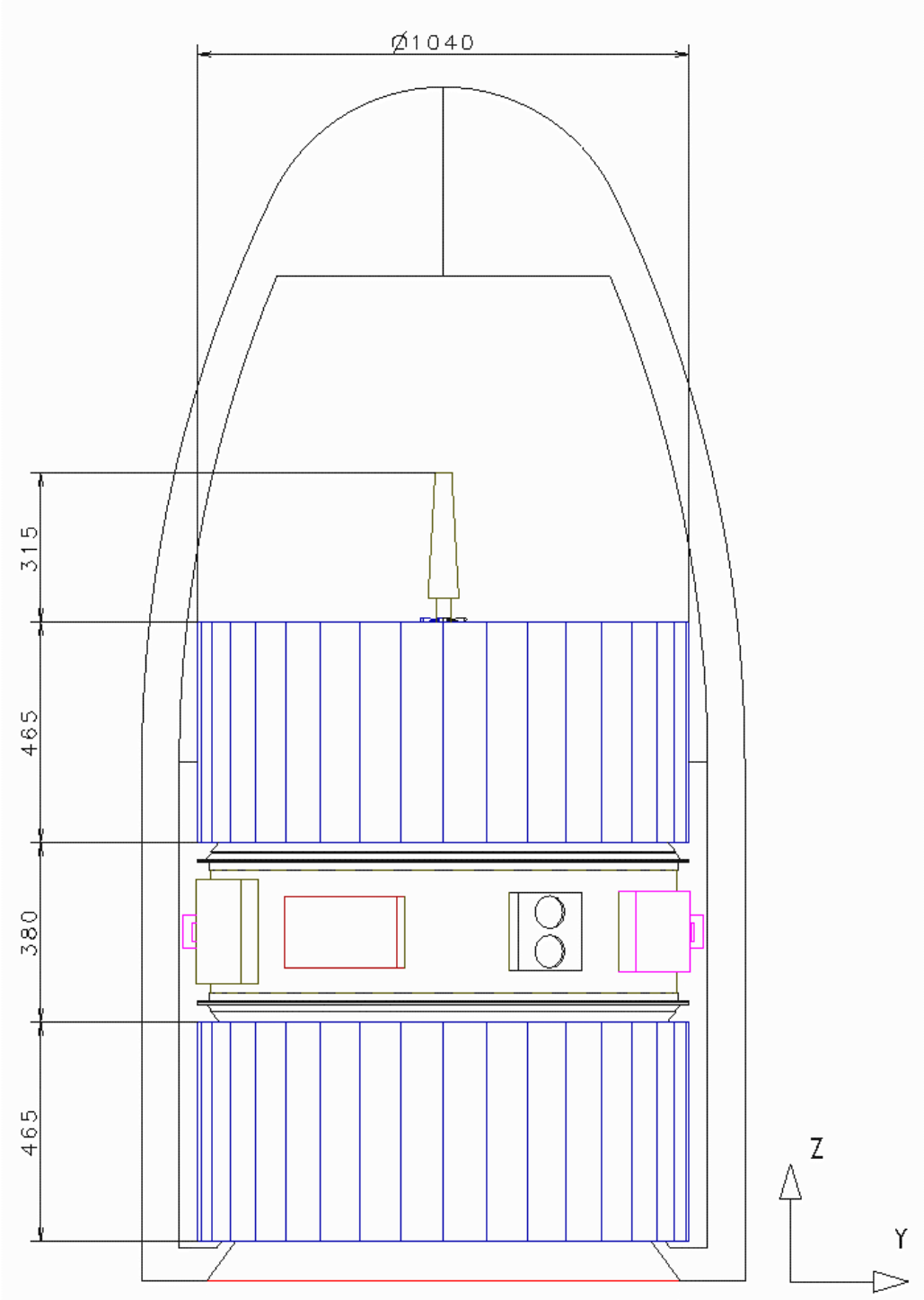

Figure 5.4 Configuration under the Pegasus fairing

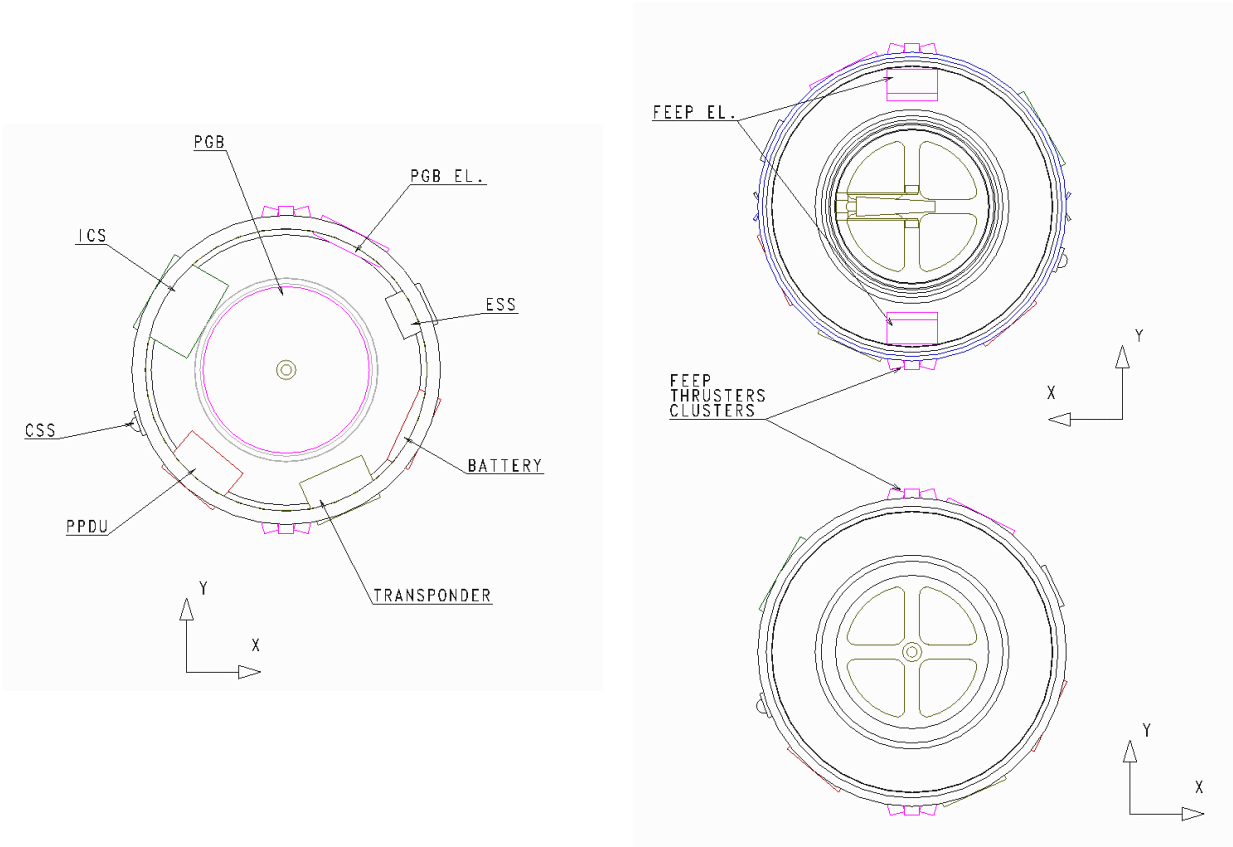

(a) (b)

Figure 5.5 (left panel) Equipment location in the central cylinder. The equipment include the Power Protection and Distribution Unit (PPDU), Coarse Sun Sensor (CSS), the spacecraft control system electronics (ICS), the transponder, the battery and the Earth and fine sun sensor box ; the clearance with respect to the PGB is shown too.
(right panel) Configuration of the FEEP thrusters. Six thrusters are used, placed in two groups of three on opposites sides of the spacecraft according to the scheme described in chapter 5.5. Each thruster package carries its own small propellant reservoir, dispensing with tanks and feed lines. Each cluster of three thrusters is served by an electronic package mounted close to it.

LAUNCH LOCKING OF THE PGB ASSEMBLY For launch-locking of the PGB assembly to the structure (to transfer the inertial launch loads), two concepts have been elaborated. In the first option, the locking mechanism is placed on the area housing the suspension spring device; then, the launch loads use the circular lower platform to reach the launcher interface

In the alternative concept illustrated in Fig 5.6, a short cylinder is used to mount a lock/unlock mechanism composed by three pins, equally spaced along the circumference. Such mechanism would be actuated by means of a set of springs (to move the pins in the unlocked position), tensioned wires (to actuate the pins locking against springs) and electrically actuated cutters (acting on the wires). The advantages of this solution are that (a) the load path is shorter, reducing the PGB bounce response, and (b) the lock device is moved away from the area of the suspension springs device, reducing its complexity. A trade-off between the two solutions will be performed in the detailed design phase. Whatever the final choice for this lock/unlock device, a set of 8 inch-worms (4 at the top and 4 at the bottom), will be placed between the PGB central tube and a short spacecraft tube for a finer, controlled, release of the

PGB. The inch-worms are arranged at 90º from one another, in between the active dampers as shown in Fig. 2.20; the unlocking procedure is discussed in Sec.2.1.6. In addition, the PGB has mechanical stops in all similar to those of the test bodies with radial shafts being allowed only very limited movements (about half a cm); see Sec. 4.1 and Fig. 4.3.

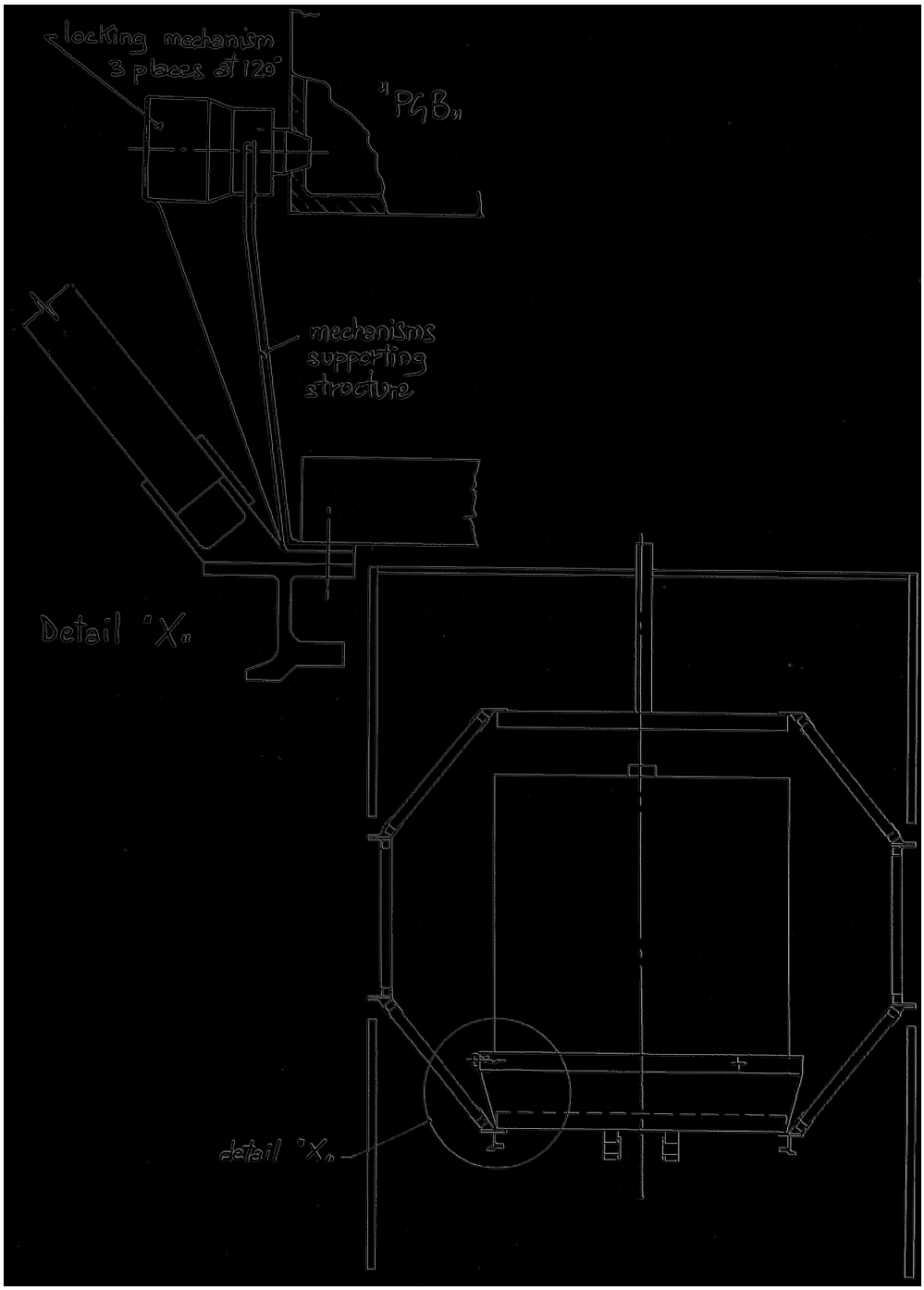

Figure 5.6 Alternative lock/unlock mechanism concept

MASS COMPENSATION SYSTEM Thermal distortion of the spacecraft structure will change the moment of inertia about the spin axis, hence, at constant angular momentum, the spin rate (see Sec. 2.1.2). The effect can be compensated for by suitable masses suspended on rods that expand and contract in "counterphase" to the spacecraft. The system can consist of a high-CTE rod cantilevered (and thermally anchored) on the outer shell and connected to a parallel, low-CTE rod supporting a balance mass on its free end (Fig. 5.7a). However, configuration constraints lead to short rod lengths and large balance masses. Moreover, the large spin centrifugal force suggests to modify the scheme into that of Fig. 5.7b. Yet another concept is based on two rods in a triangular configuration supporting the balance mass (Fig. 5.7c). Angle α is constrained by considerations of friction angle and linearity. In a preliminary sizing, the rod's Δl is amplified by a factor of $\cong 1/\sin\alpha \cong 6$, allowing use of conventional Al alloy rods and small balance masses, on 4 positions around the cylinder. Solution (c) was adopted for the purposes of the mass budget in Table 5.18.

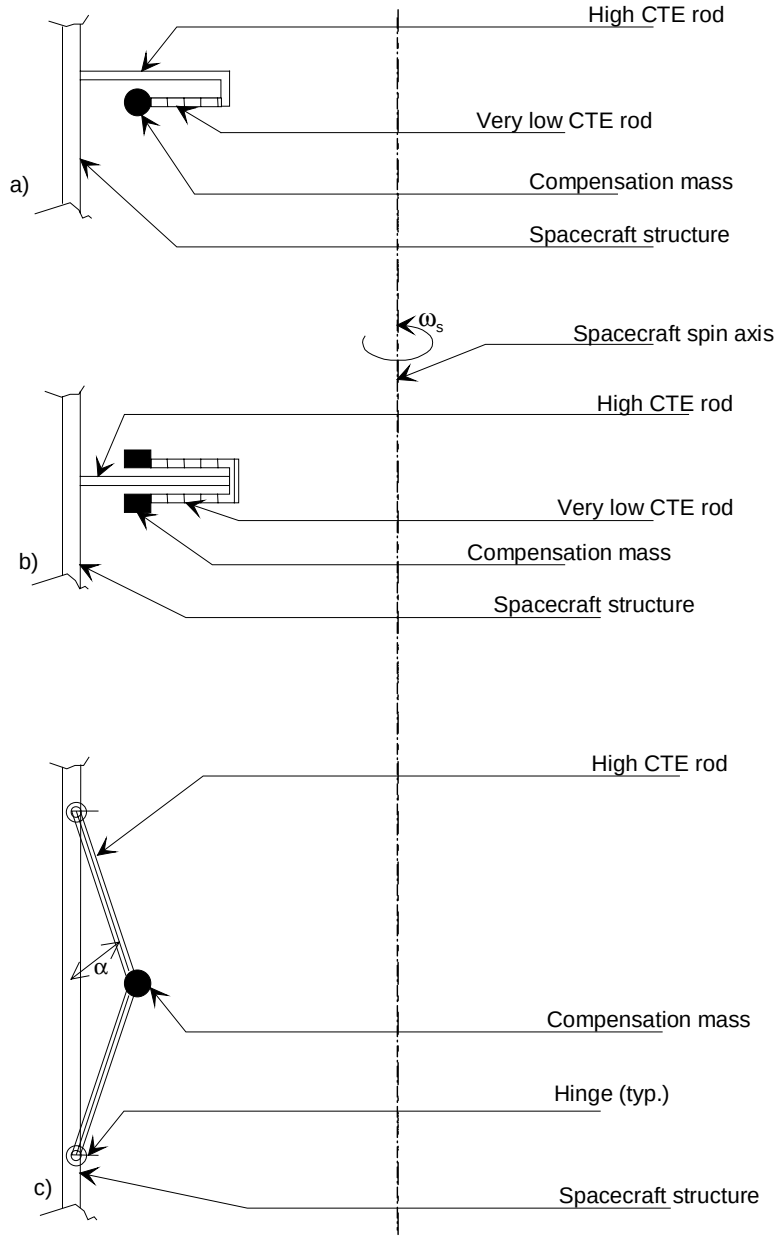

Figure 5.7 Concepts for the passive compensation of thermal expansion and contraction

5.3 MECHANICAL DESIGN

5.3.1 STRUCTURAL DESIGN

The task of the structure is to support the satellite equipment through all mission phases including transportation; the structure is conventionally divided into a "primary structure", to withstand the launch loads and a "secondary structure" composed of brackets and other minor attachment points. The structure provides the following functions:

- it supports all the spacecraft (S/C) equipment
- it transfers the launch loads to the launcher interface
- it has adequate stiffness to decouple S/C to launcher modes
- it guarantees alignment between critical equipment
- it contains equipment mounting brackets (if necessary)
- it allows for ballast mass(es) allocation due to balancing needs (if any) of the overall integrated spacecraft
- it allows for thermal decoupling
- it gives support to passive thermal protection (e.g. MLI)
- it gives support to thrusters and plumbing
- it gives equipment protection against launch vehicle vibration environment
- it allows electrical ground return service as part of the electrical distribution system
- it minimises electrostatic discharge problems
- it has dedicated points (and/or areas) for S/C lifting and suitable interface(s) toward the launch vehicle.

The GG satellite is mainly composed of:

- the PGB package
- the primary structure surrounding the PGB
- the solar panels.

The PGB is connected via suitable suspension springs (locked at launch) to the primary structure; the latter interfaces the launcher separation plane via a standard (Pegasus 23") adapter ring.

5.3.2 LAUNCHER MECHANICAL REQUIREMENTS

The satellite structure has been designed to be compatible with the PEGASUS launcher environment. Preliminary data about the VEGA launcher have been included for comparison. The study has been performed using the requirements coming from the PEGASUS launcher; they are:

- frequency requirements
- dimensioning loads
- Safety Factors
- S/C Centre Of Mass location

FREQUENCY REQUIREMENTS. To avoid dynamic coupling between the launcher low frequency modes and the spacecraft modes, the spacecraft shall be designed with adequate structural stiffness. The minimum eigenfrequency requested to the spacecraft in hard-mounted condition at the separation plane is $20\ Hz$ (i.e. excluding the S/C separation system). In order to take into account the uncertainties connected to the study maturity, we set for the preliminary structural design a value $>40\ Hz$.

The VEGA launcher minimum eigenfrequencies at launch are $18\ Hz$ (TBC) in lateral and $30\ Hz$ (TBC) in axial mode, hence largely met by our 40 Hz design target.

DIMENSIONING LOADS. The S/C primary structure shall be sized under the most severe combination of loads that can be encountered at any given instant of flight assuming the lateral loads may act in any direction simultaneously with longitudinal loads. The design limit loads to be used in the static analysis are shown in Table 5.4; they refer at the base of the separation system.

The VEGA launcher Quasi Static Loads at launch are $\pm 1.0\ g's$ (TBC) in lateral and $-8.0\ g's$ (TBC) in axial direction w.r.t. the launcher body.

		Axial (g's)	(*)		Lateral (g's)	
	Static	Dynamic	Total	Static	Dynamic	Total
Taxi, Abort and Captive Flight	±1.0	N/A	±1.0	3.67	N/A	3.67
Aerodynamic Pull-Up	-3.7	±1.0	-4.7	2.34	1.41	3.75
Stage Burn-out (**)	-9.2	±1.0	-10.2	0.28	1.41	1.69

Note: (*) the minus sign (associated to the S/C "Z" axis) indicates compression
(**) the static value depends on the "Payload" mass here assumed to be 300 kg.

Table 5.4 Pegasus Design Limit Loads

SAFETY FACTORS. Pegasus launcher requires different Safety Factors depending on the design and test options. A value of 1.5 and 1.1 at ultimate and yield respectively is demanded if the "proof test on each flight article" is chosen; an ultimate Safety Factor of 3.0 has been assumed for unconventional materials (e.g. CFRP).

No data are yet available about the VEGA launcher safety factors; use of standard values is hence recommended.

S/C CENTRE OF MASS LOCATION. Pegasus launcher limits the S/C centre of mass location as follows:

a) $\cong 750\ mm$ (along the launcher X axis) from the separation plane for a S/C mass of $300\ kg$
b) $\cong 25\ mm$ (radially) from the launcher centreline when the HAPS is used.

The proposed configuration is in agreement with the above data.

5.3.3 MATERIALS SELECTION AND PROPERTIES

Drivers in the structural materials selection have been the strength capability, the stress corrosion resistance and CTE values for those parts which must insure high mechanical stability. The used materials are:

- 7075 *Al*-alloy
- CFRP (for sandwich skins).

A trade-off has been performed between *Al*-alloy and CFRP materials for honeycomb skins; mass over stiffness ratio is nearly the same for the two classes of materials, hence the CFRP material has been chosen as baseline in order to reduce as much as possible the S/C thermal distortion.

The main engineering constants of the selected materials are reported in Table 5.3-2. The mechanical properties of the main S/C structural components (Sandwich Plates) are collected in Table 5.6.

7075-T6 Al-alloy	
density elastic modulus Poisson coefficient Tensile strength (yield) Compressive strength (yield) Ultimate Shear Strength Coefficient of Thermal Expansion	ρ = 2795 kg/m^3 E = 71 Gpa ν = 0.33 σ_{ty} = 413.7 MPa σ_{cy} = 420.6 Mpa σ_{su} = 289.5 MPa CTE = 23·10^{-6} m/m/°C
Sandwich honeycomb (3/16-5052-.001 Al-alloy type)	
density shear modulus L direction shear modulus W direction	ρ = 49.69 kg/m^3 = 310.3 Mpa = 151.7 MPa
CFRP laminate sandwich sheets (M40/914c tape)	
laminate lay-up laminate type ply thickness number of plies density $E_1 = E_2$ $\nu_{12} = \nu_{21}$ σ_u $CTE_1 = CTE_2$	67% at ± 60°, 33% at 0° symmetric, quasi-isotropic 125 μm (each) 12 ρ = 2100 kg/m^3 69.1 Gpa 0.3109 200 MPa 0.96·10^{-6} m/m/°C

Table 5.5 Materials Engineering Constants

	Upper circ. plate	*Upper trunc. cone*	*Central cylinder*	*Lower trunc. cone*	*Lower circ. plate*
Honeycomb height	0.050 m	0.020 m	0.020 m	0.020 m	0.050 m
Honeycomb type	3/16-5052-.001	3/16-5052-.001	3/16-5052-.001	3/16-5052-.001	3/16-5052-.001
Face sheets thickness	0.00075 m (each)	0.00075 m (each)	0.00075 m (each)	0.00075 m (each)	0.00075 m (each)
Face sheets material	CFRP Tape M40/914c	CFRP Tape M40/914c	CFRP Tape M40/914c	CFRP Tape M40/914c	CFRP Tape M40/914c

Table 5.6 Sandwiches Properties

5.3.4 STRUCTURAL MASS BUDGET

Table 5.7 shows the structural mass breakdown for the baseline configuration (CFRP sandwich skins). On all the structural items, both subsystem margins *(+20%)* and system margins *(+20%)* have been applied because of the low design maturity.

Item	Mass [kg]	S/S Margin [kg]	Total mass [kg]
Upper Platform	1.14	0.23	1.37
Upper Cone	3.08	0.62	3.70
Outermost Cylinder	4.67	0.93	5.60
Lower Cone	3.08	0.62	3.70
Lower Platform	1.14	0.23	1.37
Cones to Cylinder I/F rings (quantity = 2)	18.46	3.69	22.15
Cones to Platforms I/F rings (quantity = 2)	7.76	1.55	9.31
Lock/unlock mechanism	2.50	0.50	3.00
Separation system ring	3.95	0.79	4.74
Hardware (Inserts, cleats etc.)	2.00	0.40	2.40
Total Structure			57.34
System margin (20%)			11.47
Grand Total Structure			**68.81**

Table 5.7 Structure Mass Budget

5.3.5 FINITE ELEMENT MODEL AND STRUCTURAL ANALYSIS

Different models have been assembled and used during the study in order to follow the configuration evolution and trade-offs. Here follows a brief description of the Finite Element Model (FEM) used in the last study phase (on the frozen configuration). Carbon fibre compound materials have been eventually chosen as baseline because of their better on-orbit thermoelastic stability.

The FEM model has been assembled in order to dynamically verify the compatibility of the satellite with the launcher dynamic requirements. The output in the launch hard-mounted condition consists of the eigenvalues and the eigenvectors.

The model mesh has been obtained using the SDRC I-DEAS Master Series 2.1 pre-processor software while the MSC/NASTRAN version 68.2 program has been used to solve the mathematical model; Fig. 5.8 shows the FEM mesh.

The masses represented in the FEM model(s) include both system (20% constant) and sub-system (variable depending on the sub-system considered) contingencies; the non-structural masses, i.e. equipment masses, have been concentrated in the location of the centre of mass of each equipment item, according to the chosen layout. The masses in the FEM Model include the contingencies. The FEM model used for launch analyses is fully constrained (6 DOF's) at the spacecraft to launcher interface nodes.

STATIC ANALYSIS. According to usual rules in S/C mechanical design, the GG structure has been sized against stiffness; later on a static verification should be planned in order to detail the stresses in all structural elements. In this project phase, only a preliminary verification of the sandwich panels local instabilities and of the solar cells glue capability to withstand the centrifugal forces *(8.37 g's)* has been performed. It is useful, anyway, to point out that (with the data we have) the dimensioning launch loads of the PEGASUS launcher encompass those of the VEGA one.

LOCAL PANEL INSTABILITIES. Sandwich structures must be designed not only to have sufficient safety factors with respect to dimensioning loads but also against local instabilities such as:

- *shear crimping*: the core should be thick enough and have sufficient shear modulus to prevent overall buckling of the sandwich under load
- *intracell dimpling*: the core cells should be small enough to prevent the facings to buckle or dimple into the spaces between core walls
- *face wrinkling*: compressive modulus of the core and compressive modulus of the facings should be sufficient to prevent the facings to buckle as a plate on an elastic foundation.

The output demonstrated positive safety factors greater than unity for all the main components.

SOLAR CELL BEHAVIOUR UNDER CENTRIFUGAL FORCES. Due to the fast rotational motion of the satellite, the solar panels, that are located at the periphery, are subject to severe centrifugal loads

$F_c = m \cdot \omega_s^2 \cdot r$

where

F_c is the centrifugal force applied on the single solar cell (N)
m is the solar cell mass (about $0.003\ kg$)
ω_s is the angular velocity ($2\ Hz = 120\ rpm \approx 12.566\ rad/sec$)
r is the distance of the solar cell from the rotation axis ($0.52\ m$).

The resulting force is $F_c \approx 0.25\ N$. As the cell dimensions are about $20x40\ mm$, the resulting pull-up stress on the adhesive is about $\sigma_p \approx 0.0003\ N/mm^2$. From brochure data (ref. BeppoSAX project), the pull-up capability of a typical adhesive (e.g. RTV-S 691) is $R_p \approx 1.5\ N/mm^2$ at $20\,°C$. Assuming a decreasing of the nominal glue capability down to $1/50$ in a temperature range $70 \div 100°C$, we find anyway a very comfortable Safety Factor:

$F \cdot S_p = R_p / \sigma_p \approx 100$

NORMAL MODE ANALYSIS AT LAUNCH. Normal modes analysis (ref. MSC/NASTRAN Dynamic Handbook) of the S/C in hard-mounted condition has been performed and the results are reported in Table 5.8. Fig. 5.8 shows the FEM model mesh and Figs. 5.9 to 5.11 show the eigenvector plots of the first three modes. The requirement in terms of minimum "constrained" eigenfrequencies has been met; the obtained values contain however a positive margin on the minimum eigenfrequencies such to take into account the flexibility added by connection elements (e.g. cleats) and model assumptions. From the VEGA launcher viewpoint, we can stress the fact that with the assumed requirements (i.e. $f_0 > 40\ Hz$) and the FEM output, no particular problems can now be envisaged in case the VEGA launcher were to be chosen.

Mode No.	Frequency [Hz]	Type
1	49.3	Axial mode (PGB + Platforms)
2	65.9	Lateral mode (whole primary structure)
3	66.1	Lateral mode (whole primary structure)
4	150.4	Local mode (PPDU)
5	157.1	Local mode
6	166.9	Local mode

Table 5.8 Normal Modes output of the GG structure

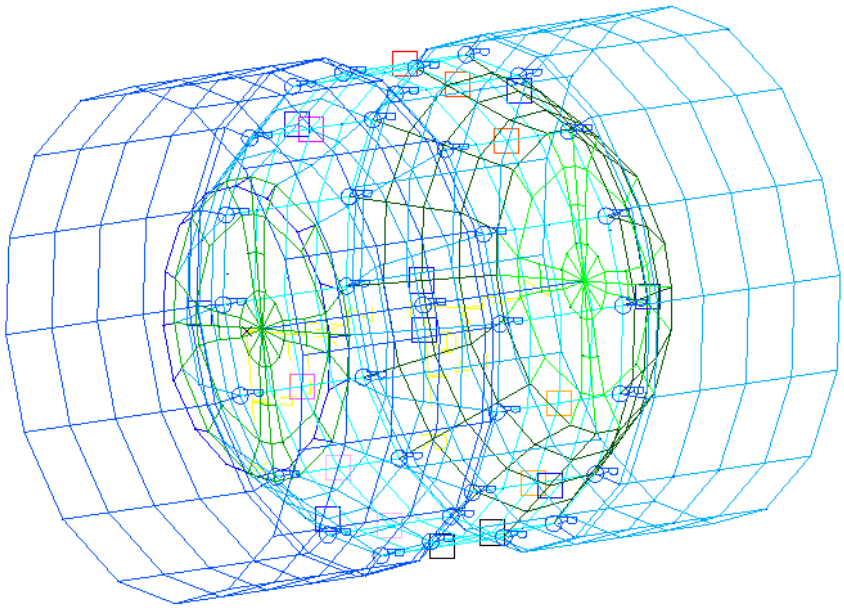

Figure 5.8 Finite Element Model Mesh. The final spacecraft FEM model consists of about 500 nodes and 500 elements.

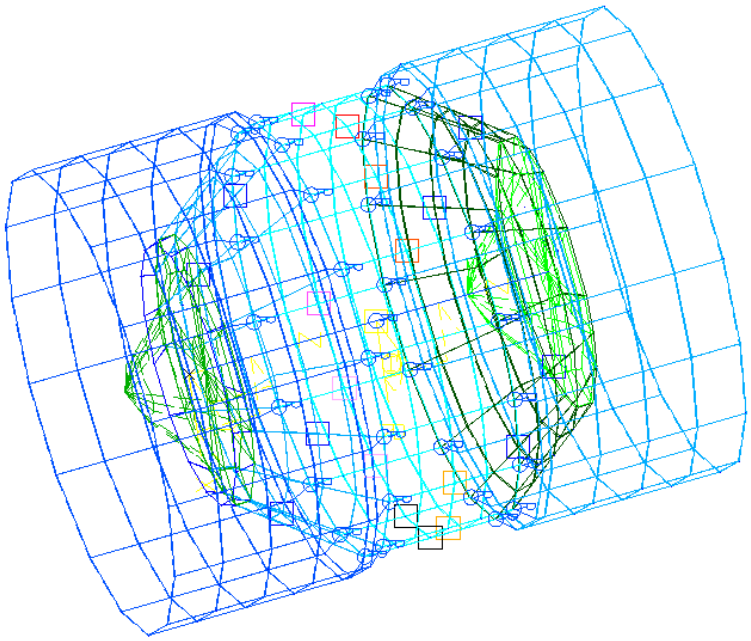

Figure 5.9 Eigenvector Plot : First Axial Mode. The mode represents a 'bouncing' along the longitudinal symmetry axis of the whole structure, while fixed at the separation plane.

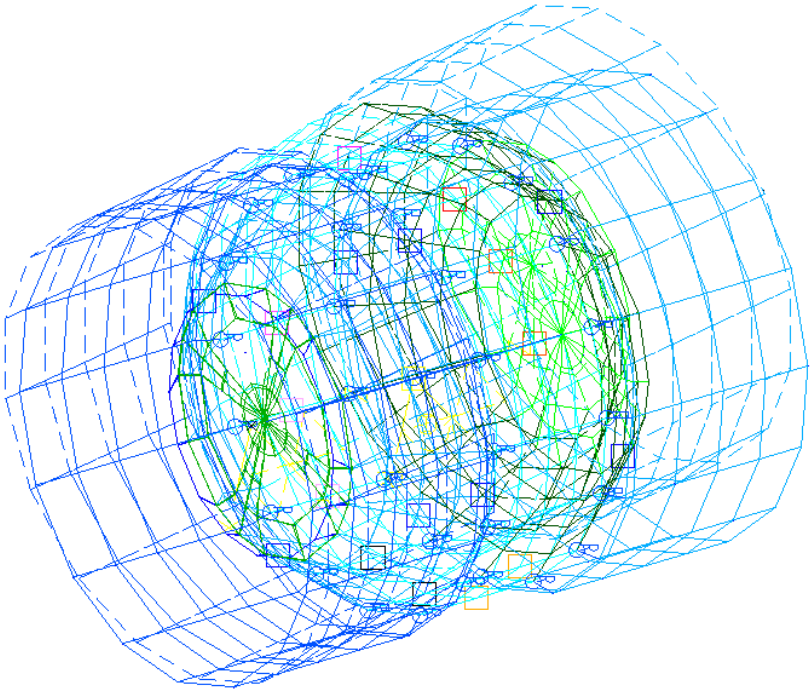

Figure 5.10 Eigenvector Plot : First Lateral Mode. The mode consists in a lateral motion of the structure, that behaves as a cantilevered boom while fixed at the separation plane.

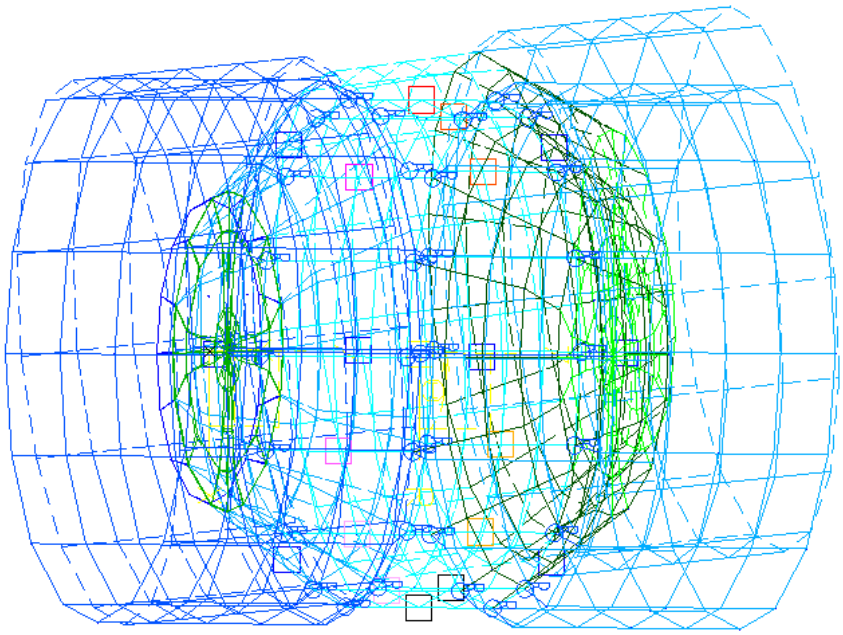

Figure 5.11 Eigenvector Plot : Second Lateral Mode. Like the first lateral mode, it consists in a lateral motion of the structure, that behaves as a cantilevered boom while fixed at the separation plane.

SOLAR PANEL MECHANICAL CHARACTERISTICS. Solar panels can have either an *Al*-alloy or CFRP sub-structure; the following preliminary characteristics have been used:

- Panel flexural rigidity (*Al*-alloy type) [D] = 6750 $N \cdot m$
- Panel flexural rigidity (CFRP type) [D] = *13400* $N \cdot m$

(see HEXCEL® TSB124 catalogue). The global solar panel mass per unit surface is $4.65\ kg/m^2$ for the Al-alloy type and $3.45\ kg/m^2$ for the CFRP type (nominal values without contingencies). The dynamic analysis results are pertinent to a solar panel having a CFRP sub-structure, and including mass margins.

Because of the preliminary phase of the project, no stress evaluation has been carried out for the solar panel sub-structure; we recommend to study this particular aspect in the detailed design phase.

5.4 SPACECRAFT THERMAL CONTROL

5.4.1 THERMAL CONTROL SUBSYSTEM (TCS) REQUIREMENTS

The S/C thermal control subsystem shall maintain all equipment within the temperature range applicable to their operating status in all mission phases. It shall be designed to guarantee adequate margins between the predicted units extreme temperature ranges (based on worst design cases) and the required operational temperature limits.

Radiative and conductive thermal decoupling between the spacecraft and the PGB shall be implemented to minimise mutual interaction and perturbations.

For the spacecraft equipment, commonly accepted temperature limits have been assumed, as shown in Table 5.9.

ITEM	Operating range [°C]	Design range [°C]	Non-Operative range [°C]	Design Range [°C]
Electronic Units Batteries	-10 to +50 0 to +20	0 to +40 +5 to +15	-20 to +60 -5 to +25	-10 to +50 0 to +20

Table 5.9 Temperature Requirements

5.4.2 TCS CONCEPT AND CONFIGURATION

The main features of the S/C thermal control subsystem are shown in Fig. 5.12. The following characteristics of the thermal hardware are foreseen.

MLI BLANKETS. MLI Blankets on external surfaces will consist of 20 layers double aluminised Kapton or Mylar with Dacron net as spacer. In the S/C parts exposed to high heat input, e.g., thruster plumes, the shield material will be *0.3 mil* aluminised Kapton. The external MLI has an outer layer of *2 mil* Kapton that is coated with a suitable finish.

The MLI will cover all the external surfaces except the radiators and part of the FEEP's external surfaces. Furthermore internal MLI blankets will wrap units surfaces not facing the radiators with an outer aluminised foil to decouple them from the interior of the S/C and all the external PGB surface.

MLI blankets of ten layers, white painted on the side facing space will cover the back of the solar panels as well as their supports. Table 5.10 below shows the specific conductivity of the blankets introduced in the model.

Average T [°C]	-100	-50	0	50	100
K MLI 10 layers [W/m²]	0.025	0.037	0.050	0.065	0.083
K MLI 20 layers [W/m²]	0.017	0.025	0.035	0.048	0.062

Table 5.10 MLI blanket conductivity

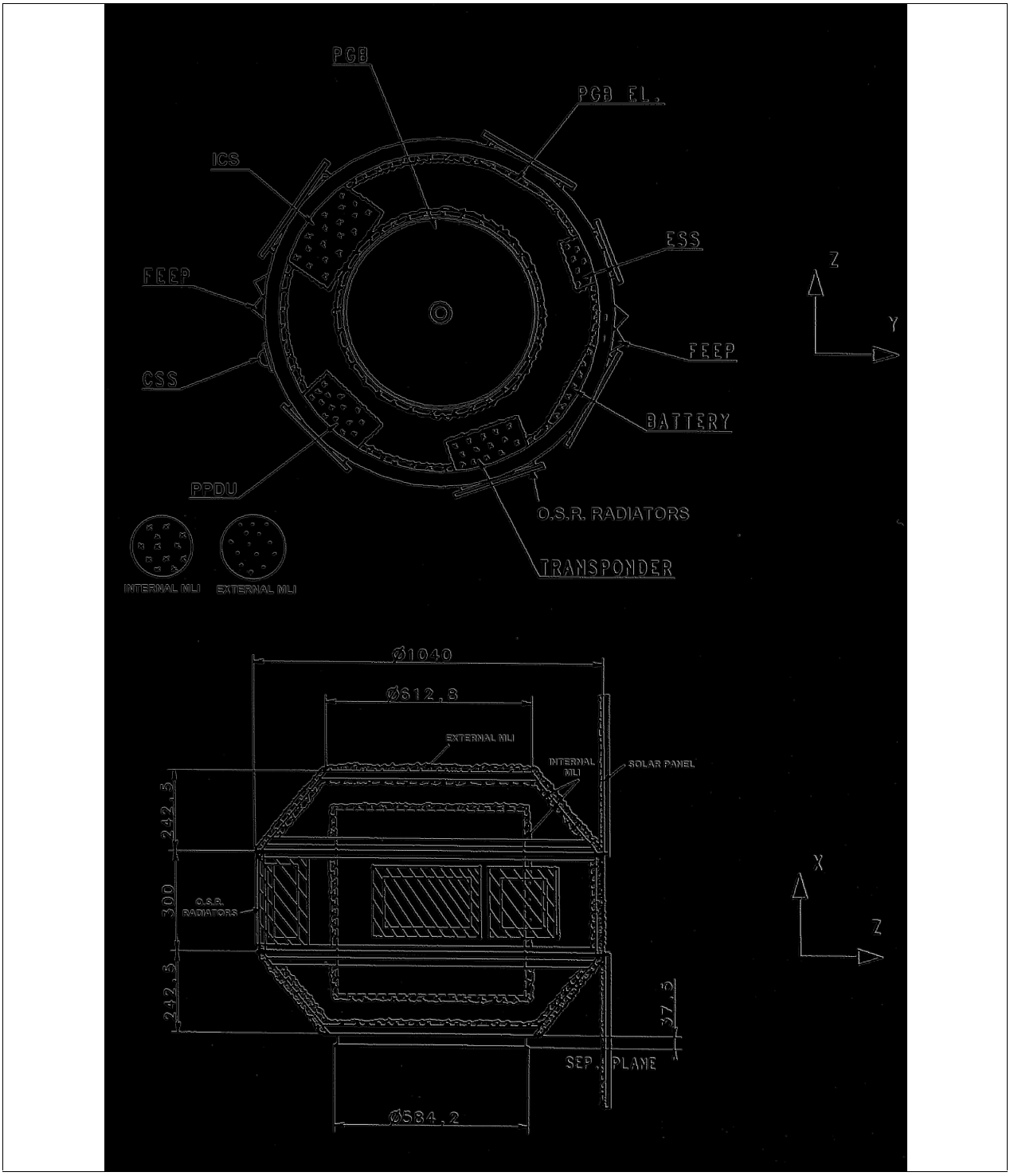

Figure 5.12 Thermal Design Concept

SURFACE FINISHES. The thermo-optical properties of the surface finishes are summarized in Table 5.11 below.

Thermo-optical Properties	α/ε Beginning of life	α/ε End of life
MLI I.T.O Kapton	0.3/0.77	0.43/0.77
O.S.R Optical Solar Reflector	0.1/0.80	0.15/0.8
5 mil Teflon G401500	0.09/0.75	0.2/0.75
Internal MLI	n.a./0.05	n.a./0.05
Adapter	0.5/0.8	0.5/0.8
Solar Array Cell Side	0.75/0.82	0.75/0.82
Solar Array Back	0.51/0.71	0.51/0.71

Table 5.11 Thermo-optical properties

COATINGS ON RADIATORS. Considering the direct exposure to the Sun of the radiative areas, Optical Solar Reflectors (OSR's) have been selected as baseline radiator coating to minimise the parasitic heat absorption. They require flat surfaces to be mounted, therefore flat radiators panels have been foreseen mounted on the units base plates according to Fig. 5.12. For the FEEP electronics mounted on the outside, part of their surface will operate as radiator covered by Teflon tape.

5.4.3 TCS Performance

SELECTION OF THE DESIGN CASES. The selection of the design reference cases is based on the following aspects:

- Location of the radiative surfaces
- Mission phase and corresponding orbital data
- Dissipation levels and their distribution in the S/C and in time
- Attitude of the S/C
- Solar aspect angle w.r.t. the radiator surfaces
- Occurrence of eclipses
- View to Earth.

Only the operational phase of the mission was considered: circular equatorial orbit at *520 km* altitude, S/C attitude with the spin axis *(2 Hz)* normal to the orbital plane. Owing to the requirements on inertia moments of the S/C, the location of the equipment must be distributed as far as possible in the central belt of the satellite. This leads to have radiator surfaces directly exposed to the Sun during sunlight, consequently the hot case (sizing case for the radiators) occurs when the Sun is perpendicular to these surfaces and the albedo and infrared input are at their maximum (thermo-optical properties of surface at end of life). Conversely, the cold case (sizing case for heater power) occurs at Summer Solstice, minimum of the solar constant,

albedo and infrared input (thermo-optical properties at beginning of life). The adopted constants for the hot and cold case are in Table 5.12.

Design Case	Solar Constant [W/m²]	Albedo Coefficient	Planet Flux [W/m²]
Hot Case	1381	0.35	271
Cold case	1327	0.20	235

Table 5.12 Design cases

The data above are the input for the calculation of the external heat fluxes, performed by the THERMICA package. The spin has been taken into account by averaging the heat input over *10* spin positions. The fluxes are the external heat input for the Thermal Mathematical Model, built by means of the ESATAN package.

RESULTS FROM THE THERMAL MATHEMATICAL MODEL. A transient analysis was performed; to avoid very long runs, due to a very small integration step, the MLI capacity was set to zero and only that of the structural items, equipment and Test Masses was introduced in the model (a conservative assumption).

The analyses were carried out over several orbits (more than 20) to simulate the long term behaviour of the S/C. The equipment dissipation values (Table 5.13) were introduced under consideration of the different operating modes during eclipses or sunlight phases. Concerning the battery, three different levels were considered corresponding respectively to trickle charge, overcharge and discharge periods, but the values (not available in this project phase) have been roughly estimated and should be reviewed in the next phases. To take into account of uncertainties of the equipment dissipation levels, a margin of *20%* w.r.t those presented below was applied in the model in the hot case simulation, while in the cold case, performed to evaluate the heater power need, no margin was applied. The calculated heater power need is of *10 W* applied on the battery during the orbit except the overcharge period.

All the equipment are maintained in the required ranges with the assumed design. Equipment box temperatures are kept around *20°C* in the hot case and around *5°C* in the cold case, with excursions at orbit frequency of about *±3°C*.

A preliminary mass budget of the Thermal Control equipment is shown in Table 5.14.

FUNCTION	Boxes	Unit Mass [Kg]	Unit Power Sunlight [W]	Power Eclipse [W]
AOCS	Earth Sensor CSS FEEP	1.68 0.28 2.50	1.0 8.0	1.0 8.0
OBDH	ICS	7.80	12.0	12.0
POWER	Ni-Cd Battery PPDU	5.00 8.40	1.3 trickle 8.1 overcharge 11.0	4.7 discharge 7.0
TT&C	Transponder	5.00	7.7	6.0
PAYLOAD	PGB Electronics	9.00	6.0	6.0

Table 5.13 Equipment dissipation

ITEM	Quantity [m²]	Unit mass	Total Mass [Kg]
O.S.R.	0.32	0.78 [Kg/m²]	0.249
MLI 20 layers External	2.49	0.60 [Kg/m²]	1.494
MLI 20 layers Internal	3.89	0.60 [Kg/m²]	2.334
MLI 20 layers Equipment	0.80	0.60 [Kg/m²]	0.480
MLI 10 layers Solar Arrays	3.12	0.36 [Kg/m²]	1.123
White Paint	3.12	0.25 [Kg/m²]	0.780
Black Paint	1.52	0.12 [Kg/m²]	0.182
Thermal Filler	0.26	0.24 [Kg/m²]	0.062
NARMCO Washers	1000	0.0002 [Kg]	0.2
Miscellaneous	n.a.	n.a.	0.6
SUBTOTAL			**7.5**
Contingency Margin (20%)			**1.5**
Total with Margin			**9.0**

Table 5.14 TCS Mass budget

5.4.4 CONCLUSIONS AND CRITICAL AREAS

A passive thermal control of the S/C is feasible with the proposed configuration. The global estimated radiative surface is *0.32 m²* (O.S.R) for the equipment located inside the S/C and *0.02 m²* (Teflon tape) each for the FEEP's located outside. These results are not yet completely

optimized, as they depend mainly on the effective dissipation time history levels, not yet completely known, this optimization should be performed in the detailed design phase. However even if the levels would increase there would be a considerable margin on available area (more than *50%);* possibly, this could lead to a configuration with a prismatic continuous central radiative belt rather than the present one with a radiator tailored for each equipment, diminishing the drag perturbation effects but increasing the S/C structural complexity and the mass.

The calculated heater power need is *10 W* applied on the battery during the orbit except the overcharge period. As this value depends on the radiators size and on the effective dissipation levels, it has to be reviewed in the optimization phase. The analysis demonstrates that the S/C internal environment, with the assumed thermal control design, does not affect radiatively the PGB environment; furthermore, being the conductive link to the main structure through the interface very small (via *2* tiny helical springs, each made of *3 Cu* wires of *0.011 mm²* cross section, glued with epoxy on a steel wire of *0.015 mm²;* see Fig. 2.5), the thermal control of the S/C and of the Payload can be considered as de-coupled.

5.5 SPACECRAFT ATTITUDE CONTROL

The GG satellite is assumed to be a cylinder with the following parameters:

- radius $r = 0.5\ m$
- height $h = 1.3\ m$
- mass $M = 250\ kg$
- moment of inertia about the spin axis $J_z = 32\ kg{\cdot}m^2$
- moment of inertia about a cross axis $J_x = 25\ kg{\cdot}m^2$.

The operational orbit is nominally circular at the altitude of $520\ km$; the maximum eccentricity is on the order of $e \approx 3{\cdot}10^{-3}$. The mean motion is $n = 1.1{\cdot}10^{-3}\ rad/sec$ and the period is $T = 5702\ sec$. The orbit is nominally equatorial; an inclination up to $I = 1^\circ$ is allowed.

In operational conditions, the satellite spins about the orbit normal at a frequency of $2\ Hz$ ($\omega_S = 12.57\ rad/sec$). The direction of the spin axis must be maintained within 1° of the orbit normal. The high momentum bias (about $400\ Nms$) produces a high gyroscopic stability of the spin axis direction.

The spin rate is subjected to:

a) a knowledge requirement (for post-processing): it must be possible to separate the spin rate from the fundamental frequency of the differential mode $\omega_{DM} \cong 1.15{\cdot}10^{-2}\ rad/sec$. This leads to $\Delta\omega/\omega_S \cong 10^{-3}$, equivalent to detecting a phase shift of $\Delta\varphi \cong 6{\cdot}10^{-3}\ rad\ (0.35^\circ)$.

b) a more demanding requirement on the RMS(ω_S) from the drag free control $\Delta\omega/\omega_S \leq 10^{-4}$, equivalent to detecting a phase shift of $\Delta\varphi = 6{\cdot}10^{-4}\ rad\ (0.035^\circ)$ in one spin period (see chapter 6). The DFC requires the lowest possible $\sigma(\omega_s)$, since the RMS of the spin angular frequency determines the residual drag at the orbital frequency. On the other end, the bias of the measurement of ω_s is not as sensitive as the $\sigma(\omega_s)$, since a constant error on the determination of the spin angular frequency is easily removed from the controller input.

The satellite is made up of four co-aligned, co-rotating cylinders, coupled by springs. External torques applied to the outermost cylinder (the 'spacecraft') will tend to change its orientation relative to the cylinder surrounding the test masses (the PGB). The requirements are:

- differential spin rates between the spacecraft and the PGB must not be allowed to produce an angular displacement in the plane perpendicular to the spin axis $> 10^{-2}\ rad$
- tilt of the spin axis of the spacecraft with respect to that of the PGB $< 10^{-2}\ rad$.

The main tasks of the Attitude and Orbit Control System (AOCS) are therefore:

- to remove the initial precession and nutation due to the spacecraft separation from the launcher last stage, and to spin the satellite up when the correct spin axis orientation (perpendicular to the orbit plane) has been reached
- to control the spin rate and the orientation of the spin axis of the spacecraft, relative to the PGB
- to measure the spin rate with a relative accuracy $\Delta\omega/\omega_S = 10^{-4}$
- to measure the orientation of the spin axis and the direction of the Earth, with respect to an inertial frame, both with an accuracy of about $6{\cdot}10^{-3}\ rad\ (0.35^\circ)$.

INITIAL ATTITUDE ACQUISITION. The final stage of the launcher is assumed to be capable of the initial slew maneuvers to rotate the satellite to approximately the required attitude. In general the spacecraft separation from the launcher is not symmetrical and therefore an undesired angular momentum, perpendicular to the satellite symmetry axis, can be generated.

The initial satellite spin rate, also provided by launcher, is not particularly high (up to *0.28 Hz);* thus the spacecraft momentum bias is low and the angular impulse, generated by the non symmetric separation, induces precessional and nutational motions. The satellite must promptly recover the correct orientation of the solar array because the battery can provide power only for a short time (up to about *1 hour*).

High nutation rates require a very long time to be damped passively; quick damping can only be performed by active systems (AOCS actuators).

An initial angular momentum of *56 Nms* (corresponding to an initial spin rate of *0.28 Hz*) and an angular impulse generated at separation of *5 Nms* (commonly accepted for Pegasus XL) will be assumed for sizing the actuators.

ACTUATORS SELECTION FOR THE PRE-OPERATIONAL PHASE

A standard system based on magnetometers and magnetic torquers is not allowed by the magnetic compatibility requirements. For pre-operational attitude control, two propulsion options were traded off:

- additional FEEP thrusters with a higher thrust capability than that needed for drag-free control
- cold gas (Nitrogen) thrusters with a thrust of *20 mN* and Minimum Impulse Bit of 10^{-3} *Ns*.

The FEEP thruster option is ruled out by considerations of available power and duration of the manoeuvres. The cold gas system is not constrained by the available power and can provide much higher control authority with respect to the FEEP solution. Minor disadvantages are the centre of mass shift as the propellant is consumed and the need for a propellant tank, to be located on the symmetry axis. Hence, the cold gas system is the preferred solution.

The envisaged system comprises a gas tank, fill-and-drain valve, pressure transducer, latching valves, four thrusters and piping. The thrusters are located on the top platform and orientated as shown in Fig. 5.13; they can provide the spin-up torque as well as torques about the *X* and *Y* axes. The propellant mass required is 1.5 kg and the subsystem mass is *8.6 kg*. The time required for the maneuvers is 0.8 hours for rate damping and *5.5 hours* for spin-up.

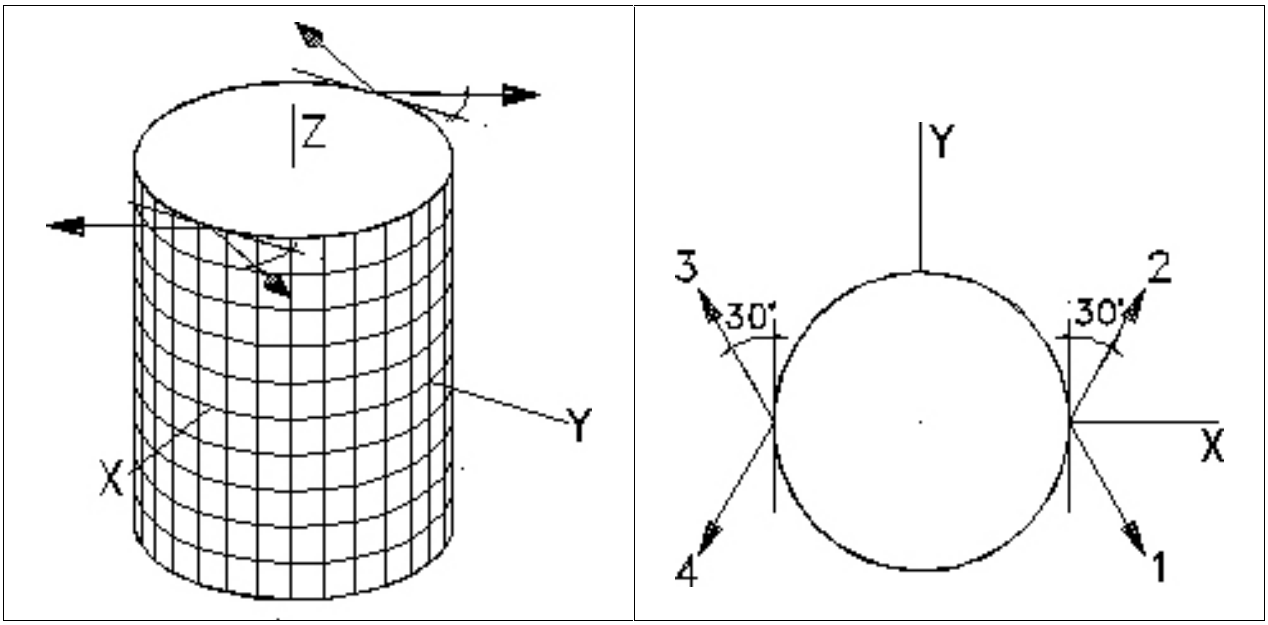

Figure 5.13 Layout of the pre-operational thrusters

ATTITUDE CONTROL IN THE OPERATIONAL PHASE. Effects perturbing the attitude of the spacecraft include nutation, rotation of the inertial direction of the spin axis, and changes of the spin rate. Nutation (free rotation about an axis different from the symmetry axis, coincident by construction with the axis of maximum inertia) is passively damped by the mechanical coupling of the spacecraft with the PGB.

The tilt of the spin axis is negligible in the time span of the mission, because of the high ratio of spin kinetic energy to magnitude of the perturbing torques. Hence, no control of the spin axis direction is required.

The largest effect producing a change in the spin rate of the spacecraft is due to thermal expansion and contraction of the satellite. The eclipse-sun and sun-eclipse transitions induce thermal expansions and contractions; to conserve angular momentum, the spacecraft inertia changes. Such variations of the satellite spin angular frequency produce a differential angular velocity between the spacecraft and the inner Pico Gravity Box; without any spin control, the relative angular displacement is of the order of $1\ rad$ in one orbital period. The effects due to drag and to solar radiation pressure are negligible with respect to the inertia thermal variation.

The thermal expansion has been modeled assuming that the thermal variation of the inertia is equivalent to the motion of 4 small bodies, symmetrically placed in the equatorial plane of the spacecraft. The distance of the four bodies from the spin axis of the spacecraft is maximum in sunlight phase (maximum expansion of the satellite, maximum inertia) and null in the eclipse phase (maximum contraction of the satellite, minimum inertia). The characteristic time scale of the motion of the four small bodies depends on the thermal time constant of the system, which means on the steady state thermal excursion of the spacecraft and on its thermal penetration depth.

A compensating system of masses, such as that described in Sec. 5.2, can reduce the inertia variation (by expanding/contracting in the opposition with respect to the spacecraft outer shell) to about 10% of the total effect, in the worst case. This residual 10% variation needs an active control. A controller (Proportional-Derivative controller plus low pass filter) capable to compensate the motion of the four bodies was implemented using DCAP; the results show that the spin frequency variations after the control are below the scientific requirements.

Two symmetrically placed pairs of light-emitting diodes can be used to detect the relative phase between Spacecraft and PGB, with a resolution better than $10\ \mu m$ on a distance of $30\ cm$, which is $43''$ of degree. The phase coming from the average of the two sensor pairs can be used as input for the spin controller.

CONFIGURATION OF THE DRAG FREE CONTROL THRUSTER. The GG drag-free control is treated presented in Chap. 6. Fig. 5.14 shows a possible layout of the FEEP thrusters, providing forces both in the radial and in the longitudinal direction, as well as small torques for residual spin control.

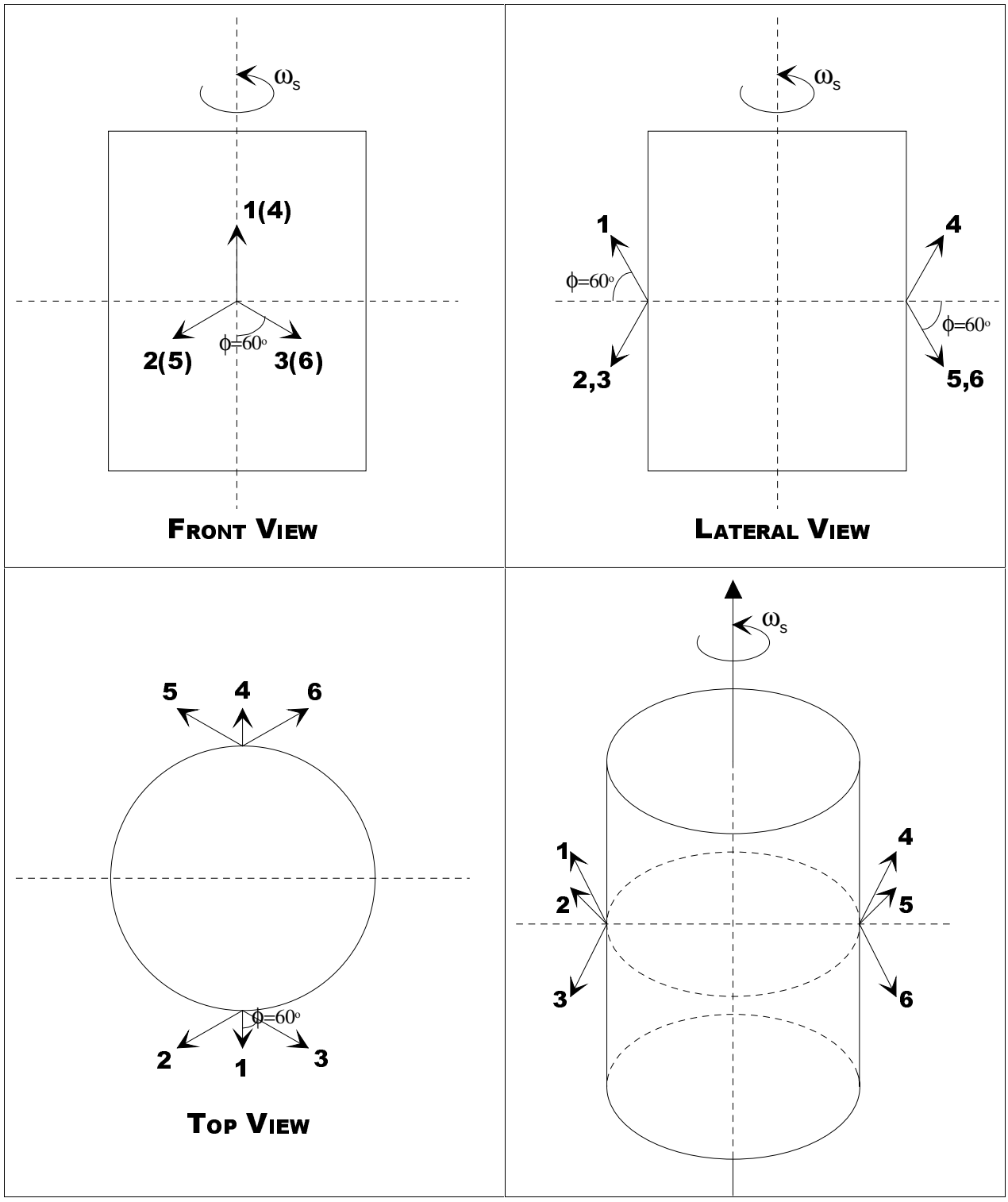

Figure 5.14 Layout of the FEEP thrusters

ATTITUDE SENSORS SELECTION. An Earth sensor, able to measure the Earth elevation angle, is preliminarily baselined for GG. For a satellite with momentum bias perpendicular to the orbit plane, there is no indetermination in yaw angle measurement with just an Earth sensor; the satellite orientation is inertially fixed (because of the gyroscopic stiffness) and therefore an error in yaw angle would be detected, after a quarter of orbit, as an error in roll.

An Earth sensor must perform a scanning to detect the Earth limbs and then to derive the attitude angle; the satellite spin can be exploited to perform the required scanning motion (the sensor would be fixed to the satellite with the two optical axes perpendicular to the spin direction). Standard Earth sensors can provide a measurement accuracy compatible with the requirement. For this assessment, we assume the Officine Galileo EES (Earth Elevation Sensor), with the following characteristics:

- mass = $1.4\ Kg$
- power consumption = $0.7\ W$
- systematic error = $0.05\ ^\circ$
- random error = $0.01\ ^\circ (3\sigma)$.

The ESS and a Sun Elevation Sensor can be accommodated in the same housing. The Sun Elevation Sensor is more accurate than the EES (3σ random error $= 0.01^\circ$ and systematic error $= 0.035^\circ$) and can guarantee partial attitude determination redundancy in case of EES failure.

5.6 ON BOARD DATA HANDLING

The characteristics of the GG experiment, requiring highly integrated test mass position control and drag-free control, without any traditional attitude control tasks in the operational phase, naturally lead to a decentralised computer architecture: the payload data processing and control tasks are executed in a dedicated payload computer while the spacecraft data management and pre-operational attitude control are handled by the platform control system.

The spacecraft data management will be based on the Integrated Control System (ICS) architecture adopted in the PRIMA bus. The ICS includes a Spacecraft Control Unit (SCU) that handles the ground link (telemetry and command) and executes the software performing the platform attitude control, data handling and fault detection and recovery tasks. The SCU software uses a 1553 bus to collect attitude, surveillance and telemetry data and to distribute commands. Attitude sensors and actuators are interfaced through a Remote Unit (RU) that also handles the platform and payload equipment. Data are stored in a modular solid-state Mass Memory Unit. Fig. 5.15 shows the block diagram.

To estimate the telemetry and mass memory storage requirements, two operational modes are introduced:

- Normal scientific mode
- High rate mode (calibration).

In the normal scientific mode, the demodulation of all signals is executed on board at the spin frequency *(2 Hz)* and only the demodulated signals are transmitted to the ground (hence, at much lower frequency). The exception is the reference spin signal (the same that is used on board for demodulation) that is sampled at *30 Hz* frequency and transmitted to Earth for correlation in the data processing. During calibration, and exceptionally to assess the operation of the payload system, the raw data (non demodulated) are collected for up to *10 minutes* and later transmitted during the ground contact periods. Table 5.15 shows the housekeeping data rate estimate and Table 5.13 shows the payload data rate estimate.

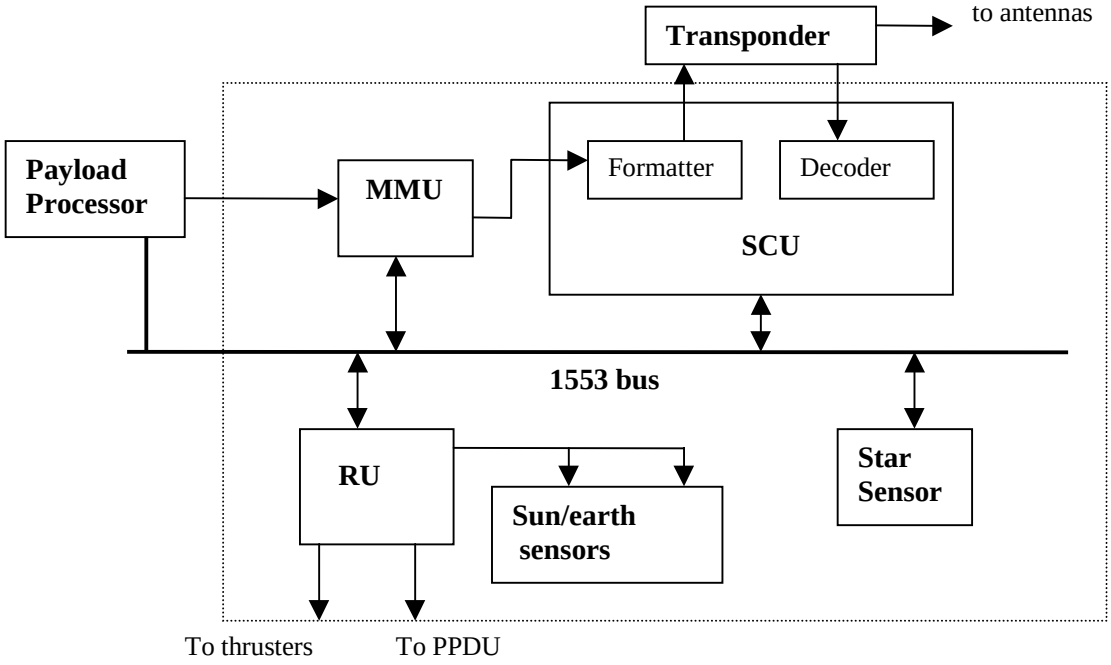

Figure 5.15 ICS block diagram

Type	No. records	Record length (bits)	Normal Mode		High rate mode	
			Frequency (Hz)	Total data rate (bits/s)	No. x Frequency	Total data rate (bits/s)
Satellite housekeeping	100	16	1/60	27		27
Payload housekeeping	20	16	1/60	5		5
Thruster commands	8	16	2	256	8x20	2560
Damper commands	3	16	20	960	12x20	3840
Total data rate				**1248**		**6432**

Table 5.15 Housekeeping and auxiliary data rate budgets

Type	No. records		Normal Mode	
		Record length (bits)	Frequency (Hz)	Total data rate (bits/s)
Position of test masses relative to each other [1]	2	16	100/500	6.4
Position of test masses relative to PGB [2]	2x3	16	20/100	19.2
Spin reference signal [3]	3	16	15/0.5	1440
Temperature [1]	1	16	20/500	0.64
Spin axis attitude [1]	2	16	20/500	1.28
Phase difference between PGB and spacecraft [2]	1	16	20/100	3.2
Total data rate				**1471**

[1] Natural test mass differential oscillation period = 500s
[2] Natural PGB oscillation period = 100s
[3] Spin period = 0.5 s

Table 5.16 Scientific data rate budget

The total data rate in the normal scientific mode, excluding coding and packet overheads, is *1.25+1.5 kbps*, equivalent to about *16 Mbit/orbit*, and the normal telemetry rate (before coding and packetising) is *26 kbps*, assuming regular *10-minute* passes, once per orbit, above the San Marco equatorial station. An on board mass memory sized for *24-hour* autonomy would amount to about *240 Mbit*. The whole *24-hour* memory contents could be downloaded to the ground station in one single pass of 10' duration at a rate of about half the *1 Mbps* maximum rate permitted by the current ESA S-band stations.

In the high-rate mode, the whole scientific data set is stored before demodulation, and the total data rate is close to *100 kbps*. However, since *10 minutes* of data collection are considered sufficient for payload status assessment, the telemetry rate is on the order of *100 kbps* and the mass memory storage capacity required for this mode is *60 Mbit*.

5.7 TRACKING, TELEMETRY AND COMMAND

The primary functions performed by the Radiofrequency subsystem are:

- Perform phase demodulation on the incoming telecommand signal and provide the video signal to the on board computer
- Perform phase modulation on the telemetry signals and transmit these signals in S band through the antennas
- Provide reception and coherent/ non coherent retransmission of ranging signals in order to perform range and range rate measurements.

The GG radiofrequency subsystem comprises the following units:

- two Antennas
- Radiofrequency Distribution Unit (RFDU), a switch connecting the transponder to the antennas
- one Transponder, made up of a receiver section and a coherent transmitter section.

The following assumptions have been taken.

- The GG requirements are in agreement with the Radiofrequency and modulation ESA standard and S+S/X bands coherent transponder specifications.
- The nominal bit rate of the telecommand link shall be $2\ kbps$, and all the link performances shall be measured on the basis of this reference figure.
- The telemetry data comprise two major categories: (i) science telemetry, including scientific data and all the ancillary data necessary for complete and unambiguous interpretation of the scientific observations; (ii) housekeeping data, for the purpose of: verification of commanded functions; monitoring of the spacecraft and payload status; failure detection, diagnosis and recovery actions and for general mission operations and maintenance functions.
- All the telemetry data are collected and stored by the Mass Memory Unit for subsequent transmission during periods of visibility with the Ground Station. We assume an orbit period of $95\ minutes$ and a requirement of $24\ hour$ autonomy without loss of scientific data.
- The initiation of the telemetry transmission shall be activated only upon reception from the Ground of a “start telemetry” command.
- The telemetry data shall assure at least a Bit Error Rate (BER) of $10^{-8}\ bits$.
- The maximum telemetry bit rate is $1\ Mbps$, including the possible adoption of Reed Solomon coding to improve the telemetry link margin.
- The protocol telemetry shall be managed by the on board data handling.
- During the pre-operational phase the telemetry data are composed by only housekeeping data and spacecraft on board time.
- All the performances of the transponder shall be in agreement with the ESA TTC PSS 48 standard. The RF subsystem shall provide an uplink to downlink carrier frequency ratio of $221/240$.
- The GG antennas shall provide a continuous omni-directional coverage for any spacecraft attitude.

EQUIPMENT SELECTION The RF subsystem on board GG is completely standard and any S-band architecture eventually adopted in the PRIMA bus will be applicable. For the purposes of this design exercise, the following assumptions have been made.

Antennas: quadrifilar helical antenna (see, e.g., BeppoSAX) with peak gain over *1 dBi* and *90°* beam width with *-3 dBi* at the edge. For global coverage, two antennas are used, one located on top of the spacecraft and one on the bottom.
Radio Frequency Distribution Unit (RFDU): the RFDU circuit losses are less than *0.2 dB* with a TX signal below *2.5 W*. The dimensions are *48·33·55 mm* and the mass is *200 g*. The average electrical consumption is lower than *0.1 W*.
Transponder: standard coherent transponder design compatible with the ESA standard. The transmitter is on during the visibility time with the Ground Station. The transponder interface with the decoders which belong inside the OBDH subsystem is via RS422 interface.

Usually all units in the radiofrequency layout are doubled to obtain electrical layout tolerance to any single failure, except the RFDU which is internally redundant, and the reliability of which is very high. For a low cost approach, we assume only one transponder on board the spacecraft, a solution frequently adopted in small spacecraft to save mass and power.

LINK BUDGET In the evaluation of the link budget we assume that the maximum amount of data (scientific and housekeeping) to be transmitted in a single ground station pass is *240 Mbits*. The average visibility time is *600 sec* per orbit. Taking into account the synchronisation, the tracking operations and Reed-Solomon coding overhead, different rates of telemetry in the range of: *1.0 - 0.5 Mbps* can be selected. In particular, Reed-Solomon coding can be added in real time when the data are transmitted; use of this coding increases the bandwidth by *1.14* times.

The GG link budget is evaluated with the ESA database layout and includes a detailed evaluation of the losses on board the spacecraft. The maximum Power Flux Density limits are never exceeded during transmission. A summary of the link budget results is in Table 5.17 below.

		NOM	ADV	FAV	mean-3sigma	Margin-w.c. RSS
Uplink section						
Ground Station EIRP	dBW	68.76	68.21	68.81		
Margin Basic Uplink	dB	46.90	40.79	48.29	41.08	42.26
Margin carrier recovery	dB	52.43	42.40	55.58	45.09	44.33
Margin telecommand recovery	dB	44.57	34.92	47.45	37.31	36.48
Margin transponder ranging-channel	dB	38.95	41.85	30.05		
Downlink section						
Spacecraft EIRP	dBW	-8.75	-12.34	-7.45		
Margin over Power Flux Density	dB	0.50	-3.24	7.43		
Margin carrier recovery	dB	19.22	11.02	23.79	12.11	13.89
Margin telemetry recovery with BER= 10^{-8}, TX power =0.3 W, Reed-Solomon coding	dB	7.21	1.52	9.50	1.43	2.90
Requirement					**0 dB**	**1 dB**

Table 5.17 Link budget summary

The introduction of Reed Solomon coding allows to increase the link margins without exceeding the allowed Power Flux Density limit, while meeting the required value of BER=10^{-8}. In particular, both the carrier and the telecommand recovery present positive margins greater than the minimum margin required by ESA.

In the downlink budgets the carrier and the telemetry recovery of *1.0 dB* for the worst case and the nominal minus RSS case (with these input parameters, *2.90 dB*) and *0 dB* for the mean value minus three sigma (with these input parameters, *1.43 dB)* assure good link margins. The reduction of the internal RF losses on board GG and the adoption of Reed Solomon coding leads to only *-5.23 dBW (0.3 W)* radiofrequency power.

5.8 POWER SUPPLY

The purpose of the Electrical Power Subsystem (EPS) is to generate and to distribute electrical power to all the units on board the spacecraft. Power is generated during the sunlight period (59 minutes), while during the eclipse period (36 minutes) a battery supplies the required energy. From a functional point of view, the EPS is made up of:

(i) Solar Array

(ii) Sequential Switching Shunt Regulator (S^3R), providing a regulated main bus voltage in output

(iii) Battery, to provide electrical energy during ascent phase and the eclipses

(iv) Battery Charge Regulator (BCR) and Battery Discharge Regulator (BDR)

(v) Power Protection and Distribution Unit (PPDU), to distribute the electrical power to all the subsystems in the spacecraft. Each outlet is protected against short circuit and overcurrent by electronic fuses.

A possible implementation of the EPS for GG is described below (see the block diagram of Fig. 5.16). The final subsystem architecture will be based on that provided by the PRIMA bus.

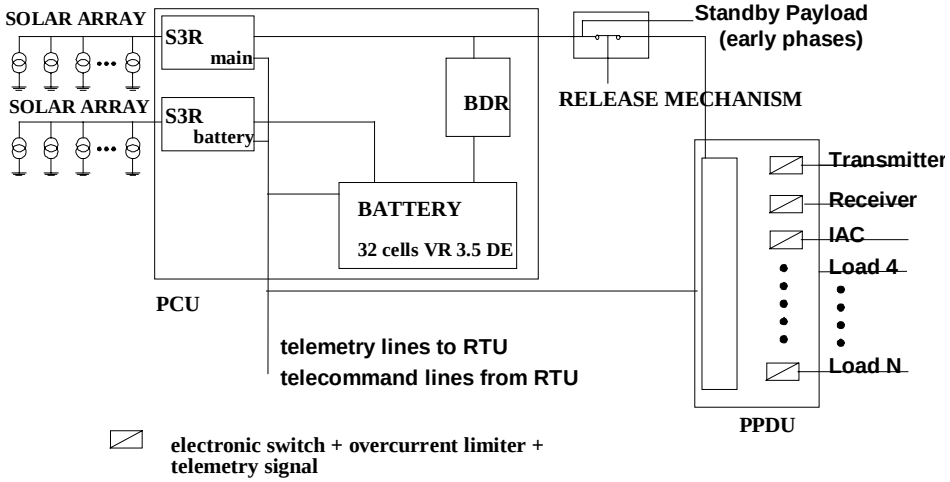

Fig. 5.16 Power subsystem block diagram

Gallium Arsenide (GaAs) cells are provided as part of the PRIMA bus complement, with photovoltaic conversion efficiency of *19%*. Hence, after accounting for radiation, pointing and packing factor losses, as well as for a small positive power contribution from the Earth reflected sunlight, the specific power is on the order of *190 W/m²*. The body mounted solar array consists of two cylindrical sections with a total efficient area of *0.97 m²;* hence the power delivered by the array is *185 W*.

A preliminary assessment of the power demand of the spacecraft gives about *110 W* (see Table 5.20). The mission consists of one running experiment, therefore there is no significant difference between the power demand in sunlight and in eclipse. *72 W* are needed to recharge the battery during the sunlight period, compatible with the array power but without any system margin. If Pegasus remains the reference launch vehicle, the power demand must be kept under strict control in the detailed design phase of the project, since the XL fairing diameter and height do not allow any significant increase of solar array size; on the other hand, ample margins for increasing the solar array area exist in the option of the VEGA (or any other) launcher.

A suitable battery comprises *32* cells with a *3.5 Ah* capacity. Such cells, already space qualified, are produced by SAFT (VR 3.5 DE). The overall weight, including *13%* contingency margin in the structure, is *5 kg* and the volume is *2.5 liters* (*260·150·80 mm* as preliminary assumption). This battery presents an equivalent magnetic moment of $M_m = 0.049\ Am^2$. This battery is sufficient for up to *1 hour* ascent plus 1 orbit for activation of all on board subsystems, under the assumption of a pre-operational power demand as in Table 5.9-3.

For the Battery Discharge Regulator a simple diode (internally redundant) could be sufficient. The diode is active when the voltage on the main bus is under the battery voltage. This solution is lighter and cheaper with respect to the common approach in which a dedicated electronic circuit maintains constant the main bus voltage during the discharge of the battery.

For the battery charge regulation, a hybrid bus using two separate S^3R's: one for the main bus and one for the battery charging, could be adopted, with advantages in terms of mass (no BCR modules) and power consumption. The S^3R is a switching system with one dump always switching on/off and the other dumps either on or off depending on the solar array power available and the satellite load requirements. The use of hexfets, or similar technology, simplifies the drive to the switching devices and further reduces the power dissipation. Hence it is possible to include in a single box S^3R, BDR and the PPDU. The bus voltage is *28 V* ± some percent during the sunlit phase, while in eclipse it decreases from *28 V* to *24 V*.

A cost saving implementation of the Power Protection and Distribution Unit would be based on the following rules: (i) a single, non redundant, outlet for each subsystem; (ii) the central computer is in charge of telemetry acquisition from each outlet, via dedicated lines. Each outlet can be switched on/off via telecommand except the receiver, the OBDH and the AOCS sensors. Further each outlet has the capability to withstand a short circuit and hence to reduce the output current with fold back protection.

On the basis of the previous description, a single box would be sufficient, including all the functions in the EPS, except the battery. The preliminary dimensions of this unit are *225·175·160 mm* and the weight is close to *7 Kg*. The few telemetry and telecommand lines are activated directly by the OBDH.

5.9 SATELLITE BUDGETS

Equipment	Q.ty	Dimensions [mm] L x W x H	Mass [kg]	Margin [kg]	Total Mass [kg]
Inner Test Mass	1	dia. 98 x 98	10.	0.	10.
Outer Test Mass	1	dia. 220 x 212	10.	0.	10.
PGB	1	dia. 560 x 550	60.	2.	62.
Capacitors, Inch Worms, Rods, etc.			3.5	1.5	5.
PGB Electronics	1	250 x 170 x 70	7.	2.	9.
Payload Data Processor	1	282 x 260 x 210	7.8	1.6	9.4
Total P/L					**105.4**
Integrated Control System	1	280 x 260 x 210	10.	2.	12.
Total OBDH					**12.**
Transponder & Antennas	1	230 x 220 x 155	4.8	1.	5.8
Total RF					**5.8**
Solar Array	2	dia. 1040 x 465	5.2	1.	12.4
PPDU	1	225 x 175 x 160	7.3	1.1	8.4
Battery	1	260 x 150 x 80	4.3	0.7	5.
Total EPS					**25.8**
CSS	1	86 x 86 x 53	0.25	0.05	0.3
Earth & Sun Sensor	1	166 x 150 x 127	1.4	0.3	1.7
Total Attitude Control					**2.**
FEEP Thrusters	6	70 x 50 x 50	0.3	0.06	2.2
FEEP Electronics	2	250 x 140 x 200	5.5	1.1	13.2
Total FEEP					**15.4**
Nitrogen Thrusters	4	50 x 10 x 10	0.1	0.01	0.4
Nitrogen Propellant			1.5	0.7	2.2
Nitrogen Tank	1	dia. 200	1.5	0.3	1.8
Lines, Valves etc.			1.8	0.4	2.2
Total Auxiliary Propulsion					**6.6**
Total Harness			**5.**	**1.**	**6.**
Total Thermal Control			**7.5**	**1.5**	**9.**
Satellite Structure	1		47.9	9.6	57.5
Mass Compensation System	1		5.	1.	6.
Total Structure					**63.5**
Total SVM					**146.1**
Total Satellite					**251.5**
System margin on P/L (20 %)					**21.1**
System margin on SVM (20 %)					**29.2**
G R A N D T O T A L					**301.8**

Table 5.18 Satellite Mass Budget

	Spacecraft only [1]	Total satellite
Centre of mass (mm) [2]		
Z	424.	424.
X, Y	< 0.2	< 0.12
Moments of Inertia (kg m²) [3]		
I_{ZZ}	27.46	32.25
I_{XX}	21.09	25.18
I_{YY}	21.77	25.86

[1] Excluding PGB and test masses

[2] Reference frame with origin at the intersection of the separation plane with the symmetry axis (Z)

[3] I_{jj} = moments of inertia about the principal axes

Table 5.19 Centre of Mass and Moment of Inertia Budget

	Pre-operational (W)	Operational (W)
Payload		
PGB electronics	0	6
FEEP electronics	0	60
Subtotal Payload	**0**	**66**
Service Module		
RF	8	8
Integrated Control System	12	12
Heaters	10	10
AOCS sensors	1	1
Harness	4	4
EPS	11	11
Subtotal Service Equipment	**46**	**46**
Total Satellite	**46**	**110**

Table 5.20 Satellite Power Budget

6. STABILIZATION AND DRAG FREE CONTROL

6.1 THEORETICAL ANALYSIS AND CONTROL LAWS

The complete GG system of *6* bodies has been simulated using DCAP (Dynamics and Control Analysis Package) software developed by ALENIA SPAZIO under ESA contract. The dynamical model is schematically represented in Fig. 6.1. The *6* bodies of the model are defined as follows:

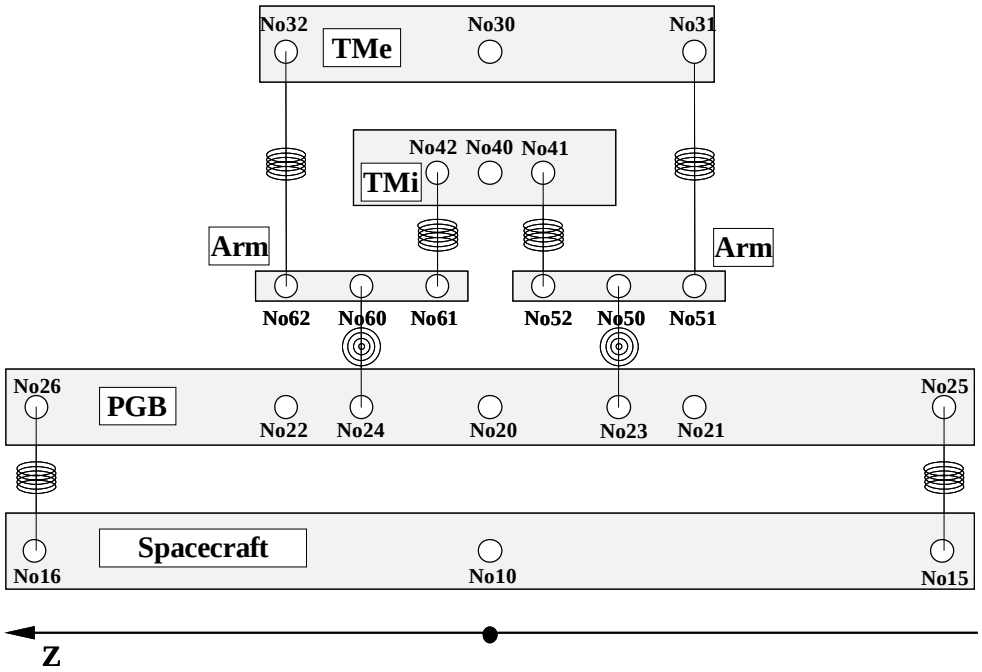

Figure 6.1 Planar 6-body model of the GG system with springs, gimbals and the related connections. The 6 bodies are: the spacecraft, the PGB laboratory, 2 test masses and 2 gimballed arms. The spin angular velocity of the spacecraft is around the Z-axis.

- Body 1 is the Spacecraft. Its motion w.r.t. inertial space is defined by the freedoms of Hinge 1 (Hi_1), connected to body reference. The X axis is the along-track direction, Y axis points towards the Earth and the Z axis is the spin axis of the spacecraft.
- Body 2 is the Pico-Gravity Box (PGB). PGB relative freedoms w.r.t. S/C are defined by Hinge 2 (Hi_2) connecting the nodes 10 and 20 (No10-No20).
- Body 3 is the outer (external) test mass (TMe). TMe relative freedoms w.r.t. PGB are defined by Hinge 3 (Hi_3) connecting the nodes 20 and 30 (No20-No30).
- Body 4 is the inner test mass (TMi). TMi relative freedoms w.r.t. PGB are defined by Hinge 4 (Hi_4) connecting the nodes 20 and 40 (No20-No40).
- Bodies 5-6 are the gimballed arms. The rotational freedoms of the arms w.r.t. PGB are defined by Hinges 5 and 6 (Hi_5, Hi_6), connecting nodes 23-50 and 24-60 respectively. No23 and No24 on PGB identify the gimbal points on the Pico Gravity Box.

This type of multi-body connection grants an open-loop kinematics topology, with no need for cut-joint hinges. All hinges are described by a Euler sequence Type 1, *x-y-z*. The active dofs (degrees of freedom) defined by hinges can be differently set depending on the type of simulation, i.e. a full 3D simulation including conical and cylindrical modes or a reduced 2D simulation with the cylindrical modes only.

2D SIMULATION WITH CYLINDRICAL MODES. The S/C, PGB and TMs have *x-y* translational and *z* rotational dofs only, and no conical modes. The gimbals allow conical movements of the coupling arms around their midpoints .

Hinge	Transl. Dofs (x,y,z)	Rotational Dofs (x,y,z)
1÷4	F, F, L	L, L, F
5÷6	L, L, L	F, F, L
Note : L=Locked F=Free		

3D SIMULATION INCLUDING CONICAL AND CYLINDRICAL MODES. The S/C, PGB and TMs have *x-y-z* translational and *x-y-z* rotational dofs. The gimbals allow conical movements of the coupling arms around their midpoints .

Hinge	Transl. Dofs (x,y,z)	Rotational Dofs (x,y,z)
1÷4	F, F, F	F, F, F
5÷6	L, L, L	F, F, L
Note : L=Locked F=Free		

6.1.1 MASS PROPERTIES

The mass properties used are consistent with the model used for the GG Pre Phase A Study (1996) and are recalled in Table 6.1. Two cases are analyzed for the gimballed arms: with and without a Pt/Ir ring respectively. In the first case they have $J_p > J_t$, while in the second they have $J_p < J_t$, that is, they would be unstable if isolated due to their pencil-like shape. The purpose is to determine whether the gimballed coupling arms inserted in the GG system (see Fig. 2.1) require rings for stabilizing the rotation or not. The result of this work (see Sec. 6.1.14) is that once the test masses are stabilized, also the coupling arms are (the test bodies are much more massive than the arms); therefore, rings are not needed, as it was predicted during the GG Pre Phase A analysis (1996).

ITEM	BODY ID	MASS [kg]	$J_t=J_x=J_y$ [$kg \cdot m^2$]	$J_p=J_z$ [$kg \cdot m^2$]
S/C	1	122.071	19.616	29.263
PGB	2	43.647	2.224	3.23305
TMe	3	10.0	0.0752	0.0754
TMi	4	10.0	0.0163	0.0165
Gimballed arms w/o ring	5÷6	$2.18 \cdot 10^{-2}$	$8.29 \cdot 10^{-6}$	$8.54 \cdot 10^{-7}$
Gimballed arms with ring	5÷6	$7.93 \cdot 10^{-2}$	$7.81 \cdot 10^{-6}$	$8.39 \cdot 10^{-6}$

Table 6.1 Mass Properties

6.1.2 GEOMETRICAL PROPERTIES

The geometrical data are set for a total PGB height of $0.7\ m$, a TMe height of $0.21206\ m$, a TMi height of $0.10603\ m$. The gimbal points on PGB have Z coordinate of $\pm 0.53015\ m$. The initial spring offset, i.e., the distance between bodies C.G. and spring mounting point is set to $1\mu m$ in x-axis for the S/C-PGB and/or PGB-TMs connections. Additional errors (mounting/mis-alignment) can be introduced in mounting points. The geometry for the DCAP nodes is summarized in Table6-2.

Node ID	Body ID	X [m]	Y [m]	Z [m]
10	1	0.0	0.0	0.0
15-16	1	$1.0\cdot10^{-6}$	0.0	±0.35
20	2	0.0	0.0	0.0
21-22	2	0.0	0.0	±0.10603
23-24	2	0.0	0.0	±0.053015
25-26	1	0.0	0.0	±0.35
30	3	0.0	0.0	0.0
31-32	3	0.0	0.0	±0.10603
40-41-42	4	0.0	0.0	0.0
50	5	0.0	0.0	0.0
51-52	5	0.0	0.0	±0.053015
60	6	0.0	0.0	0.0
61-62	6	0.0	0.0	±0.053015

Table 6.2. Geometrical Properties of the GG system simulated with DCAP software.

6.1.3 SENSORS

The sensors in DCAP are a way to monitor the dynamic state of the system, performing an ideal measurement. A set of sensors has been defined both for active control and post-processing purposes.

- Sen20, Sen201, Sen 202. Relative position of No20 w.r.t No10 in Spacecraft frame (modulus, x and y components). Sen 201 gives the ideal measurement of a capacitance plate between S/C and PGB aligned with Y axis.
- Sen30, Sen301, Sen 302. Relative position of No30 w.r.t No20 in PGB frame (modulus, x and y components). Sen 301 gives the ideal measurement of a capacitance plate between PGB and TMe, aligned with Y axis.
- Sen40, Sen401, Sen 402. Relative position of No40 w.r.t No20 in PGB frame (modulus, x and y components). Sen 401 gives the ideal measurement of a capacitance plate between PGB and TMi, aligned with Y axis.
- Sen341, Sen 342. Relative position of No40 w.r.t No30 in TMe frame (x and y components). These sensors give the differential displacements.

6.1.4 ACTUATORS AND FUNCTION GENERATORS. DEFINITION OF EXTERNAL DISTURBANCE

The external disturbance is defined in the following way. The referring orbit is a $520\ km$ circular orbit in the equatorial plane, with orbital angular velocity ω_{orb} and orbital period T_{orb}:

$$\omega_{orb}=1.102\cdot10^{-3}\ rad/sec=1.754\cdot10^{-4}\ Hz,\quad T_{orb}=5701.64\ sec \tag{6.1}$$

For the purposes of the present analysis the orbital motion of the satellite can be neglected, and also the gravity gradients components; the orbiting reference system is therefore approximated by an inertial reference frame. The following scaling has been applied to the disturbances.

- *1.0* for the main drag component (mean value of the drag); is D.C. having neglected the orbital motion
- *0.4* for the harmonic at $2\omega_{orb}$; becomes at ω_{orb} having neglected the orbital motion
- $\sigma = 0.1$ for drag noise at all frequencies

The residual drag disturbance (after Drag Free Control) has been set to $5 \cdot 10^{-9}\ N$ in order to study the effects of measurement noise. The disturbance signals are built up using DCAP function generators, which are interconnected to actuators in order to provide the requested forcing function. We have:

- Fun11, Fun12. The DC component converts to a signal at frequency $\omega_s = 2\pi/T_s\ rad/s$ in body reference, with T_s the signal period. The function generators define the signals $1.0 \cdot cos(\omega_s t)$ and $-1.0 \cdot sin(\omega_s t)$ respectively.
- Fun15, Fun16. The ω_{orb} component converts to a signal at frequency $(\omega_s - \omega_{orb}) = (2\pi/T_s - 1.102 \cdot 10^{-3})\ rad/s$ in body reference if the S/C is co-rotating with the Earth. The function generators define the signals $0.4 \cdot cos((\omega_s - \omega_{orb})t)$ and $-0.4 \cdot sin((\omega_s - \omega_{orb})t)$ respectively.
- Fun13, Fun14. The components disturbance white noise with zero mean and *0.1* sigma.

The actuators in DCAP provide a way of exerting forces or torques on the system. A "jet" actuator is characterized by an application point and a direction for an external force.

- Act11, Act12. The external force acts on S/C at No10 location; the actuators act in *x* and *y* direction respectively.

The excitation level is introduced as interconnection gain. Six interconnects Int11÷Int16 are defined according to the following scheme.

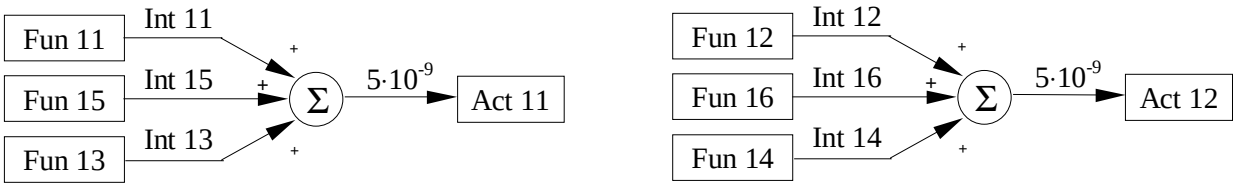

Figure 6.2 Interconnects defining the drag force components x and y (with noise).

6.1.5 PASSIVE DEVICES

Devices in DCAP define stiffness and damping according to different models. A linear device connecting two nodes on one axis provides a restoring force proportional (*k*) to the distance between nodes on that axis and (*c*) to the relative speed of the nodes on that axis. With similar definition, a device can be selected to be acting on a relative degree of freedom at hinge level. By convention, in the definition of DCAP items the rotational freedoms come first ($x \div z = 1 \div 3$) followed by the translational ones ($x \div z = 4 \div 6$). These forms allow us to define the elastic connections between bodies. With reference to the scheme of Fig. 6.1 we have:

- De23, De24, De72. Elastic connection of PGB to S/C, between No15-25 (k_t), with Device72 added for the 3D simulation.

- De25, De26, De73. Elastic connection of PGB to S/C, between No16-26 (k_t), with Device73 added for the 3D simulation.
- De33, De34, De74. Elastic connection of TMe to gimbals, between No 51-31 (k_t), with Device74 added for the 3D simulation.
- De35, De36, De75. Elastic connection of TMe to gimbals, between No 62-32 (k_t), with Device75 added for the 3D simulation.
- De43, De44, De76. Elastic connection of TMi to gimbals, between No 52-41 (k_t), with Device 76 added for the 3D simulation.
- De45, De46, De77. Elastic connection of TMi to gimbals, between No61-42 (k_t), with Device 77 added for the 3D simulation.
- De51, De52. Elastic connection of lower gimbal (Body 5) to PGB. The bending stiffness act on Hi5 rotational freedoms *(x,y)* between No23-50 (k_θ).
- De61, De62. Elastic connection of upper gimbal (Body 6) to PGB. The bending stiffness act on Hi6 rotational freedoms *(x,y)* between No24-60 (k_θ).
- De20, De30, De40. Elastic connection defining the torsional stiffness along *z* (k_ψ). The three devices respectively define the stiffness between S/c and PGB (Hi2), TMe and PGB (Hi 3), TMi and PGB (Hi4) along the *z* rotational dof (#3).

The local bending stiffness of springs is neglected, being overcome by the offset of mounting. Exception is made for the inner mass, where the connecting points are coincident (No40≡ No41≡ No42).

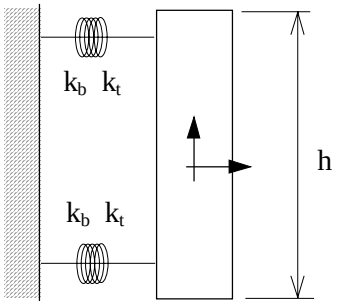

k_b : rotational (bending) local stiffness
k_t : translational stiffness

With respect to mid-point: $\bar{k}_b = 2k_b + k_t \frac{h^2}{2} \cong k_t \frac{h^2}{2}$

- De41, De42. bending connection of inner mass (TMi). The bending stiffness act on Hi4 rotational freedoms (x,y) between No20-40 (k_b).

The corresponding numerical values are given in Table 6.3. As far as the damping coefficient is concerned, we must distinguish between *x,y* translations, where the springs deform in supercritical rotation at rates close to the spin rate $(\omega_s\text{-}\omega_k,\ \omega_k << \omega_s)$, and *z* translation where instead springs deform at rate ω_k. Given a quality factor Q_k of an oscillator of mass m_k, spring constant k and natural frequency ω_k (in *rad/sec*), the damping coefficients are defined as:

$$c_k = \frac{k}{Q_k \omega_k} \quad \text{for subcritical motion } (z). \tag{6.2}$$

$$c_{eq_k} = \frac{k}{Q_k \left|\omega_s - \omega_k\right|} \cong \frac{k}{Q_k \omega_s} \quad \text{for supercritical motion } (x,y). \tag{6.3}$$

The damping coefficients are given in Table 6.3, having used $Q_{PGB}=90$ (the mechanical quality factor of the PGB suspensions) and $Q_{TM}=500$ (the mechanical quality factor assumed in this analysis for the suspensions of the test masses). Note that while $Q_{PGB}=90$ is the value measured experimentally for the suspension springs of the PGB, Q measurements for the

suspension springs of the test masses have yielded values *16000÷19000* (see Sec. 2.1.5), i.e., much better than the value $Q_{TM}=500$ assumed here. The problem is that, with the measured values the whirl motions of the test masses grow so slowly (Eq. 2.20) that the numerical control would take far too long to stabilize the system. For this reason, in all the present analysis we assume a much poorer mechanical quality for the suspensions of the test masses (by a factor of *4*)*;* therefore, the simulations refer to a dynamical control problem more difficult than the control problem of the actual GG system.

	STIFFNESS	DAMPING
Translational (PGB)	$k_t=1.0\cdot10^{-2}$ N/m	$c_{tPGB}=3.537\cdot10^{-6}$ Ns/m
Translational (TMs)	$k_t=1.0\cdot10^{-2}$ N/m	$c_{tTM}=6.366\cdot10^{-7}$ Ns/m
Bending (PGB)	$k_b=1.0\cdot10^{-7}$ Nm/rad	$c_{bPGB}=3.54\cdot10^{-11}$ Nms/rad
Bending (TMs)	$k_b=1.0\cdot10^{-7}$ Nm/rad	$c_{bTM}=6.37\cdot10^{-12}$ Nms/rad
Torsional (PGB)	$k_\psi=1.9\cdot10^{-6}$ Nm/rad	$c_{\psi PGB}=0$ Nms/rad
Torsional (TMs)	$k_\psi=1.9\cdot10^{-6}$ Nm/rad	$C_{\psi TM}=0$ Nms/rad
Gimbals	$k_\theta=4.0\cdot10^{-6}$ Nm/rad	$c_\theta=0$ Nms/rad

Table 6.3 Passive Devices Numerical Values (with $Q_{PGB}=90$, $Q_{TM}=500$). Note that we assume $Q_{TM}=500$, which is about 1/4 of the measured value, in order to make the whirl instability of the test masses grow faster so as to speed up the numerical simulations. The problem is easier if instabilities are slower, so our analysis is carried out under conservative assumptions.

Additional devices must be introduced for translations in z direction, without stiffness, defining the missing sub-critical damping. This can be done only at hinge level (*z* translation, dof #6).

- De26, De36, De46. (To be Implemented) Damping connection along *z*, at hinge level (Hi2,3,4 respectively).

All the set of devices described above define the passive elastic connections of the GG model.

6.1.6 ACTIVE DEVICES (USER DEFINED)

The implementation of active damping of whirling motion can be introduced in DCAP in different ways. We have chosen to add special devices ("user-defined" via Fortran routines), whose command is computed in the subroutines that implement the stabilization scheme will described in the following sections. These devices act in parallel to the passive ones for the supercritical dofs. A mnemonic identification number has been set, according to the following example.

De24 connects No15-25, i.e., Bo 1÷2, in x direction. Using the hinge ID number to identify the connecting bodies (Hi2) and the dof ID number (x=4), the device number is *24*. The additional user device is defined by adding a third digit (1), resulting in an ID number of *241*. This rule becomes important in the user-defined routine which identifies the applicable dofs and application points relying on device ID number.

- De241, De251. Stabilizer between S/C and PGB.
- De341, De351. Stabilizer between PGB and TMe.
- De441, De451. Stabilizer between S/C and TMi.

6.1.7 CONTROLLER

A User-Defined Discrete Controller (USDC) with sampling rate of $T_s/10\ sec$ (with T_s the GG spin period) is defined to implement the stabilization logic and the related filtering processes. The

controller adds errors to the measurements, performs filtering and computes the magnitude and phasing of the stabilization forces in the rotating frames; actuation of forces is executed by user-devices described above.

USDC has 3 inputs (relative displacements in *x,* see 6.1.8) and 22 outputs. The outputs are used mainly for checking purposes and for Drag Free Control. Details on USDC definition can be found in Section 6.2.

6.1.8 INTERCONNETS

Besides the interconnects used to activate external disturbance (see Sec. 6.1.4), three additional interconnects are used to feed the controller with the relative displacement signals. In this first implementation, only one plate is used, assuming it to be aligned with *x* direction of inboard body. The nominal sensors measurements are fed to USDC with:

- In201, In301, In401. The ideal measurements of sensors Se201, Se301, Se401 (see 6.1.3) are connected to the three inputs of user discrete controller.

6.1.9 CONSTANT DATA (CNTDTA)

The easiest way to pass data to user defined routines is through “constant data” blocks. Each CNTDTA has an ID number and a value (double precision) associated to it. The following sets of data have been defined:

- Cn 1. Spin Period
- Cn 2÷4. Coefficient of non rotating damping for PGB, TMe and TMi.
- Cn 5÷7. Whirling modes frequency, in rad/s, for PGB and common mode TMe and Tmi. These values are used for Fourier filter on the whirling period
- Cn 10. Standard deviation σ_ω for noise in the angular rate measurement from Earth Elevation Sensor (E.E.S.), relative to spin rate ($Cn10=\sigma_\omega/\omega_s$).
- Cn 11. Sensor 201 RMS for the displacement measurement noise in the small read-out capacitance plates driving the stabilization loop of the PGB.
- Cn 12. P.S.D. for the rate measurement noise in the small read-out capacitance plates driving the stabilization loops. This value is obsolete and it was used only in old continuous stabilization schemes.
- Cn 13. P.S.D. for the noise in stabilization force introduced by the active capacitance plates.
- Cn 14. Bias in the displacement measurement.
- Cn 15. Angular misalignment between the measurement plates and the reference direction (x). This gives a systematic phase error, an angular bias, in the reconstructed signal.
- Cn 16. RMS of sensors 301 and 401 for the displacement measurement noise in the small read-out capacitance plates driving the stabilization loops of TMi and TMe with respect to the PGB.
- Cn 101. Time range, starting at $t = 0\ sec$, during which the non rotating damping coefficient of the PGB is amplified to rapidly reduce the Pico Gravity Box whirling motion.
- Cn 102. Amplification factor of the non rotating damping coefficient of the PGB, utilized in the time range specified by Cn101.
- Cn 103. Time range during which the non rotating damping coefficient of the Test Masses is amplified to rapidly reduce their whirling motion. The initial instant of amplification is set by Cn 105.
- Cn 104. Amplification factor of the non rotating damping coefficient of the TMs, utilized in the time range specified by Cn103.
- Cn 105. Delay time of the amplification of the non rotating damping coefficient of the Test Masses (initial time of the amplification of TMs C_{NR}).

- Cn 106. Instant at which the PGB whirling control force is turned off.
- Cn 107. Instant at which the PGB whirling control force is turned on again (Cn 107 > Cn 106).
- Cn 108. Instant at which the TMs whirling control forces are turned off.
- Cn 109. Instant at which the TMs whirling control forces are turned on again (Cn 109 > Cn 108).
- Cn 110. Gain of the Notch filter (Drag Free Control).
- Cn 111. RMS of the Drag Free Control actuator (FEEP thrusters).
- Cn 111. Bias of the Drag Free Control actuator (FEEP thrusters).

6.1.10 EIGENFREQUENCIES

With the model set-up outlined in the previous sections, a linearization has been performed in order to determine the eigenfrequencies of the system. The eigenvalue problem has been solved for the zero-spin rate case *($\omega_s=0$),* in order to determine the whirling frequencies; linearization at non zero spin cannot be performed in DCAP and has been done with the DYNROT software by Prof. Genta and Dr. Brusa at Politecnico di Torino. We have checked that the results reported in Table 6.4 are essentially unchanged, as expected.

The complete model has 6 rigid-body dofs plus 22 flexible dofs (18 for the PGB. TMe, TMi plus 4 for the gimbals conical modes). The results are shown in Table 6.4; it can be noticed that the different configurations of the gimballed arms (with and without rings) do not affect the other frequencies; they obviously affect the local modes of the arms. If the gimbals are supposed to be mounted on a rigid fixture, with equivalent bending stiffness k'_θ given by

$$k'_\theta = 2k_b + k \cdot h^2/2 + k_\theta \cong k \cdot h^2/2 + k_\theta = 0.01 \cdot 0.10603^2/2 + 4.0 \cdot 10^{-6} = 6.0212 \cdot 10^{-5}\ Nm \qquad (6.4)$$

and with the values for J_t given in Table 6.1, the eigenfrequencies are *85.22* and *87.81 rad/sec*, thus confirming the local nature of these modes.

The configuration of gimballed arms without the stabilizing ring is expected to affect the test-masses differential modes with larger contributions. Any misalignment of the J_p axis w.r.t. spin axis is amplified by inertial moments, for a given θ_0 initial out-of-phase angle if the configuration is unstable ($J_p<J_t$). Since the conical motion of the gimballed arms directly induces differential motion in the test masses, the two configurations have been analyzed in order to evaluate the effects on differential motion and define a baseline design. It is found that, due to the much smaller mass of the coupling arms compared to the mass of the test bodies which they couple, they are in fact stabilized once the test bodies themselves are stabilized by the active control of their whirl motions. Therefore, in the remainder of this Chapter, all the 6-body simulations refer to coupling arms without rings.

	Without Pt/Ir Ring			**With Pt/Ir Ring**			
#	Freq. [rad/sec]	Freq. [Hz]	T [sec]	Freq. [rad/sec]	Freq. [Hz]	T [sec]	Type
7	7.975E-4	1.269E-4	7878.50	7.975E-4	1.269E-4	7878.50	Rz PGB
8	3.504E-3	5.577E-4	1793.15	3.504E-3	5.577E-4	1793.15	Rx Tmi
9	3.504E-3	5.577E-4	1793.15	3.504E-3	5.577E-4	1793.15	Ry Tmi
10	5.079E-3	8.084E-4	1237.09	5.079E-3	8.084E-4	1237.09	Rz Tme
11	1.076E-2	1.712E-3	583.99	1.076E-2	1.712E-3	583.99	Rz Tmi
12	1.153E-2	1.835E-3	545.08	1.153E-2	1.835E-3	545.08	DIFFERENTIAL x
13	1.153E-2	1.835E-3	545.08	1.153E-2	1.835E-3	545.08	DIFFERENTIAL y
14	2.125E-2	3.383E-3	295.64	2.125E-2	3.383E-3	295.64	Tx PGB
15	2.125E-2	3.383E-3	295.64	2.125E-2	3.383E-3	295.64	Ty PGB
16	2.125E-2	3.383E-3	295.64	2.125E-2	3.383E-3	295.64	Tz PGB

17	3.339E-2	5.315E-3	188.15	3.339E-2	5.315E-3	188.15	Rx PGB
18	3.339E-2	5.315E-3	188.15	3.339E-2	5.315E-3	188.15	Ry PGB
19	4.195E-2	6.676E-3	149.79	4.195E-2	6.676E-3	149.79	Rx Tme
20	4.195E-2	6.676E-3	149.79	4.195E-2	6.676E-3	149.79	Ry Tme
21	4.472E-2	7.118E-3	140.50	4.472E-2	7.118E-3	140.50	DIFFERENTIAL z
22	5.556E-2	8.843E-3	113.09	5.556E-2	8.843E-3	113.09	COMMON x
23	5.556E-2	8.843E-3	113.09	5.556E-2	8.843E-3	113.09	COMMON y
24	5.556E-2	8.843E-3	113.09	5.556E-2	8.843E-3	113.09	COMMON z
25	8.522E+1	1.356E+1	0.0737	8.783E+1	1.398E+1	0.0715	Gimballed arm 1 x
26	8.522E+1	1.356E+1	0.0737	8.783E+1	1.398E+1	0.0715	Gimballed arm 1 y
27	8.522E+1	1.356E+1	0.0737	8.783E+1	1.398E+1	0.0715	Gimballed arm 2 x
28	8.522E+1	1.356E+1	0.0737	8.783E+1	1.398E+1	0.0715	Gimballed arm 2 y

Table 6.4 Eigenfrequencies of the GG 6-body system at zero spin rate as computed with DCAP.

6.1.11 WHIRLING STABILIZATION

The stabilization of whirl motion (see Sec. 2.1.5 for a physical introduction) can be implemented by building in a rotating frame a damping command proportional to the relative velocity between bodies in the inertial (non-rotating) reference frame. A simple way to show this capability is by examining the problem of 2 bodies connected by a dissipative spring. Let us consider $\underline{r}_s$ the vector pointing to the Spacecraft center of mass, $\underline{r}_p$ the vector pointing to the PGB center of mass, $\underline{\varepsilon}$ the vector locating the suspension point of the spring with respect to the Spacecraft center of mass, S the Suspension point of the spring (see Fig. 6.3). The spacecraft is rotating around the z-axis, which is perpendicular to the xy plane. The rotation is counter-clockwise. In the inertial reference frame the equations of motion read:

$$\begin{cases} m_s \ddot{\underline{r}}_s = -k(\underline{r}_s - \underline{r}_p + \underline{\varepsilon}(t)) - c_r(\dot{\underline{r}}_s - \dot{\underline{r}}_p - \underline{\omega}_s \times (\underline{r}_s - \underline{r}_p)) - \underline{F}_{ext} \\ m_p \ddot{\underline{r}}_p = -k(\underline{r}_p - \underline{r}_s + \underline{\varepsilon}(t)) - c_r(\dot{\underline{r}}_p - \dot{\underline{r}}_s - \underline{\omega}_s \times (\underline{r}_p - \underline{r}_s)) \end{cases} \tag{6.5}$$

being $\underline{\varepsilon} = \underline{\varepsilon}(t)$ a rotating vector in the inertial frame (fixed in the reference frame corotating with the spacecraft) and $\underline{\omega}_s$ the spin angular velocity. These equations show clearly the nature of rotating damping, namely damping between the rotating bodies. Using: $\underline{x} = \underline{r}_p - \underline{r}_s$ (relative position vector); $m_r = m_s\, m_p /(m_s + m_p)$ (reduced mass), $\omega_0^2 = k/m_r$ (natural frequency of oscillation), $c_r = k/(Q\omega_s)$ (coefficient of rotating damping, with Q the mechanical quality factor of the spring), we can write the equation for the relative motion of the two bodies:

$$\ddot{\underline{x}} = -\omega_0^2(\underline{x} - \underline{\varepsilon}(t)) - \frac{\omega_0^2}{\omega_s Q}(\dot{\underline{x}} - \underline{\omega}_s \times \underline{x}) - \frac{\underline{F}_{ext}}{m_s} \tag{6.6}$$

The solution of the equation of relative motion is:

$$\underline{x}(t) = \frac{\omega_0^2 \underline{\varepsilon}(\omega_s t)}{\omega_0^2 - \omega_s^2} + \underline{x}_{drag}(t) + \underline{x}_{whirl}(\omega_w t) \tag{6.7}$$

with:

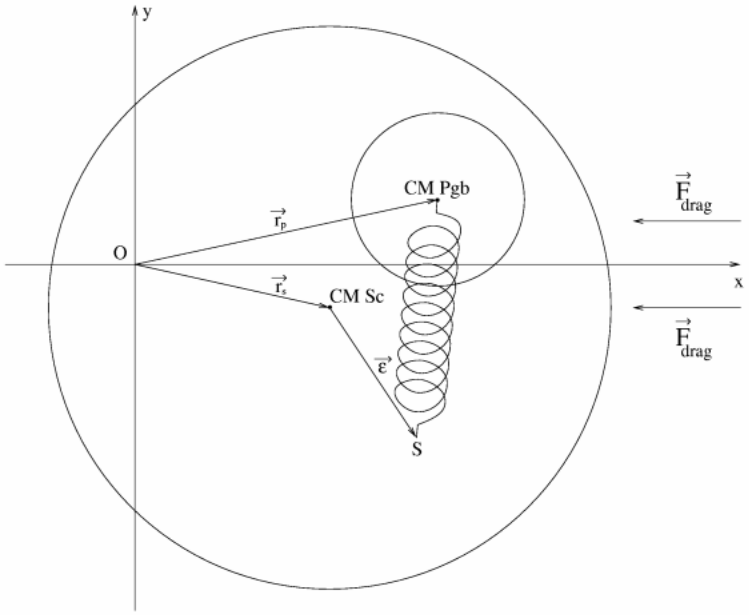

Figure 6.3 Schematization of the two-body model problem.

$$\underline{x}_{drag} = -\frac{F_{ext}}{m_s}\frac{1}{\omega_0^2 + \omega_0^2/Q^2}\hat{i} - \frac{F_{ext}}{m_s}\frac{1}{\omega_0^2 + \omega_0^2/Q^2}\frac{1}{Q}\hat{j} \tag{6.8}$$

the vector describing the displacement of the equilibrium position due to the action of the external drag and $\underline{x}_{whirl}\,(\omega_w t)$ the exponential term giving rise to the spirals shown in Fig. 6.4.

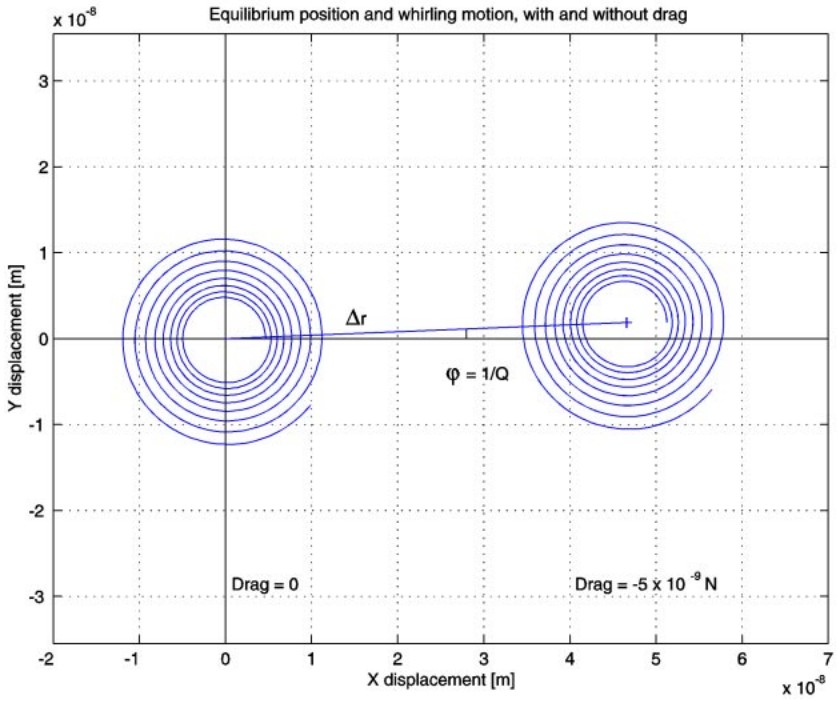

Figure 6.4 Simulation of the 2-body system with and without an external residual drag. It shows how the effect of an external force (e.g. air drag) is that of displacing the equilibrium position of the system. A small phase lag appears

due to energy losses in the suspensions (finite Q), as expected. Due to these losses the whirl instability builds up in either case around the corresponding equilibrium position.

The 2-body system is unstable. The simplest way to stabilize it is adding some Non Rotating Damping (i.e. damping between non rotating parts of the system), which is mathematically expressed by the terms containing C_{nr} (the equations refer again to the inertial reference frame):

$$\begin{cases} m_s \ddot{\underline{r}}_s = -k(\underline{r}_s - \underline{r}_p + \underline{\varepsilon}(t)) - c_r(\dot{\underline{r}}_s - \dot{\underline{r}}_p - \underline{\omega}_s \times (\underline{r}_s - \underline{r}_p)) - C_{nr}(\dot{\underline{r}}_s - \dot{\underline{r}}_p) - \underline{F}_{ext} \\ m_p \ddot{\underline{r}}_p = -k(\underline{r}_p - \underline{r}_s + \underline{\varepsilon}(t)) - c_r(\dot{\underline{r}}_p - \dot{\underline{r}}_s - \underline{\omega}_s \times (\underline{r}_p - \underline{r}_s)) - C_{nr}(\dot{\underline{r}}_p - \dot{\underline{r}}_s) \end{cases} \quad (6.9)$$

$$\ddot{\underline{x}} = -\omega_0^2(\underline{x} - \underline{\varepsilon}(t)) - \frac{\omega_0^2}{\omega_s Q}(\dot{\underline{x}} - \underline{\omega}_s \times \underline{x}) - \frac{C_{nr}}{m_r}\dot{\underline{x}} - \frac{\underline{F}_{ext}}{m_s} \quad (6.10)$$

These equations are useful to see the difference between *Rotating Damping* (term with c_r), and *Non Rotating Damping* (term with C_{nr}, which is the number defined by Cn 2 - Cn 4); see Fig. 2.16 for a physical explanation. In the space experiment everything is corotating with the spacecraft, so we need to recast these equations in the rotating reference frame:

$$\begin{cases} m_s \ddot{\underline{r}}_s = -k(\underline{r}_s - \underline{r}_p + \underline{\varepsilon}) - c_r(\dot{\underline{r}}_s - \dot{\underline{r}}_p) - C_{nr}(\dot{\underline{r}}_s - \dot{\underline{r}}_p + \underline{\omega}_s \times (\underline{r}_s - \underline{r}_p)) + m_s\omega_s^2\underline{r}_s - 2m_s\underline{\omega}_s \times \dot{\underline{r}}_s - \underline{F}_{ext}(t) \\ m_p \ddot{\underline{r}}_p = -k(\underline{r}_p - \underline{r}_s + \underline{\varepsilon}) - c_r(\dot{\underline{r}}_p - \dot{\underline{r}}_s) - C_{nr}(\dot{\underline{r}}_p - \dot{\underline{r}}_s + \underline{\omega}_s \times (\underline{r}_p - \underline{r}_s)) + m_p\omega_s^2\underline{r}_p - 2m_p\underline{\omega}_s \times \dot{\underline{r}}_p \end{cases} \quad (6.11)$$

$$\ddot{\underline{\zeta}} = -\omega_0^2(\underline{\zeta} - \underline{\varepsilon}) - \frac{\omega_0^2}{\omega_s Q}\dot{\underline{\zeta}} - \frac{C_{nr}}{m_r}\dot{\underline{\zeta}} - \frac{C_{nr}}{m_r}\underline{\omega}_s \times \underline{\zeta} + \omega^2\underline{\zeta} - 2\underline{\omega}_s \times \dot{\underline{\zeta}} - \frac{\underline{F}_{ext}(t)}{m_s} \quad (6.12)$$

with $\underline{\zeta}$ and $\dot{\underline{\zeta}}$ the relative displacement and its rate of change in the rotating reference frame. The minimum C_{nr} for stabilizing the whirling motion is $C_{nr} = c_r\ \omega/\omega_0$.

6.1.12 WHIRLING STABILIZATION CONTROL LAW

We have seen in the previous Section that the stabilization of whirl motion can be implemented by building in the rotating frame a damping command proportional to the relative velocity between the bodies in the inertial (non-rotating) reference frame

$$\underline{F}_{NR} \propto \dot{\underline{\zeta}} + \underline{\omega}_s \times \underline{\zeta} \tag{6.13}$$

A more compact complex notation can be used by replacing the vector with a complex number $(\zeta=\xi+i\eta)$ and the cross product operator $\underline{\omega_s}\times$ by $i\omega_s$ $(i=\sqrt{-1})$, giving

$$F_{NR} = F_{NR_X} + iF_{NR_y} = \dot{\zeta} + i\omega_s \zeta\,, \tag{6.14}$$

all in the rotating frame. Conversely, if $Z = X + iY$ is the displacement in the inertial frame, the relative velocity in rotating frame, on which rotating damping acts, can be defined as $\dot{Z} - i\omega_s Z$.

The main drawback of a continuous approach is that the whirl motion builds up with long time constants, and consequently the rate of change of the relative amplitude is highly dominated by the measurement noise. The tangential component of the stabilization signal instead must be built from the difference of two large terms, i.e., $(\omega_s-\omega_n)t$ and $\omega_s t$, affecting the phasing of the compensation command. Furthermore, any bias in the measurement is amplified by the pre-multiplication of ω_s.. A modified approach based on signal filtering has therefore been introduced.

Let us see the solution of the equation motion (relative displacement of the bodies) in the rotating reference frame; in absence of non rotating damping it reads:

$$\underline{\zeta}(t) = \frac{\omega_0^2 \underline{\varepsilon}}{\omega_0^2 - \omega_s^2} + \zeta_{drag}(t) + \underline{\zeta}_{whirl}((\omega_w - \omega_s)t) \tag{6.15}$$

The first term is a fixed vector in the rotating reference frame which depends on the initial offset of the mounting point of the springs; the second term is a vector corotating with the drag force (with the angular velocity ω_s as seen in the rotating frame) and with a phase lag ϕ with respect to the drag depending on the mechanical quality factor of the spring, $\tan(\phi) = 1/Q$; we have assumed a drag defined by a DC component plus a term at orbital frequency in the inertial reference frame, so, $\zeta_{drag}(t)$ has ω_s and $(\omega_s-\omega_{orb})$ angular frequencies (in the rotating reference frame). The third term, describing the growing spiral of the whirl motion, has $(\omega_s-\omega_w)$ angular frequency. The idea is of using the precise signature of the growing whirling motion to build a control law capable of stabilizing the system. The starting point is sampling the relative displacement signal within every spin period T_s, with N points, and to analyze the harmonic at T_s in order to reconstruct the modulating signal amplitude and phase: note that in this way any bias is removed (it is a constant additional term of $\zeta(t)$). Given N sampled points of the displacement $\zeta(t)$ in the spin period interval $T_s=\omega_s/2\pi$:

$$\begin{cases} \zeta_k = \zeta(t_k) \\ t_k = \dfrac{k-1}{N-1} T_s \quad (k = 1, N) \end{cases} \tag{6.16}$$

the fundamental harmonic can be obtained from Fourier integral as

$$\hat{\zeta}(t) = C \cdot \cos\frac{2\pi t}{T_s} - S \cdot \sin\frac{2\pi t}{T_s} = A \cdot \cos\left(\frac{2\pi t}{T_s} + \varphi\right)$$
$$S \equiv \frac{2}{\pi} \cdot \sin\frac{\pi}{N-1} \cdot \sum_{k=1}^{N-1} \zeta_k \cdot \cos\frac{2\pi t_k}{T_s} = \frac{2}{\pi} \cdot \sin\frac{\pi}{N-1} \cdot \sum_{k=1}^{N-1} \zeta_k \cdot \cos\frac{2\pi(k-1)}{N-1}$$
$$C \equiv \frac{2}{\pi} \cdot \sin\frac{\pi}{N-1} \cdot \sum_{k=1}^{n} \zeta_k \cdot \sin\frac{2\pi t_k}{T_s} = \frac{2}{\pi} \cdot \sin\frac{\pi}{N-1} \cdot \sum_{k=1}^{N-1} \zeta_k \cdot \sin\frac{2\pi(k-1)}{N-1} \qquad (6.17)$$
$$A \equiv \sqrt{C^2 + S^2} \quad \varphi \equiv tan^{-1}\left(\frac{S}{C}\right)$$

From the difference between the corresponding values in two spin periods, the velocity of the modulating signal is then reconstructed. We obtain in fact a pair of values (A_k, φ_k) for each spin period. The first harmonic filtered amplitude A_k and phase φ_k can be used with A_{k-1}, φ_{k-1} at previous step $(t_{k-1}=t_k-T_s)$ to determine the relative velocity in the inertial frame. The velocity signal V_k and its phase φ_{V_k} are determined according to the following sketch.

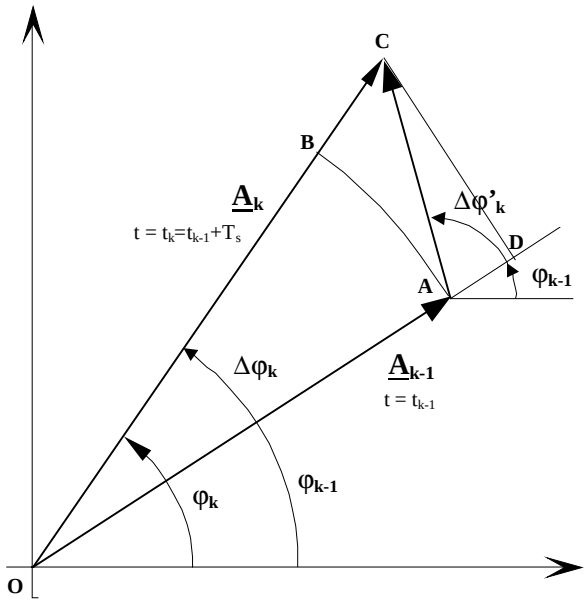

$$\overline{BC} = \Delta A_k$$
$$\overline{OA} = \overline{OB} = A_{k-1}$$
$$\overline{OC} = A_k = A_{k-1} + \Delta A_k$$
$$\overline{AC} = A_{k-1}\sqrt{2\left(1+\frac{\Delta A_k}{A_{k-1}}\right)(1-\cos\Delta\varphi_k) + \left(\frac{\Delta A_k}{A_{k-1}}\right)^2} \cong$$
$$\cong A_{k-1}\sqrt{\Delta\varphi_k^2 + \left(\frac{\Delta A_k}{A_{k-1}}\right)^2}$$
$$\Delta\varphi'_k = tan^{-1}\frac{\left(1+\frac{\Delta A_k}{A_{k-1}}\right)\sin\Delta\varphi_k}{\left(1+\frac{\Delta A_k}{A_{k-1}}\right)\cos\Delta\varphi_k - 1} \cong tan^{-1}\frac{A_{k-1}\Delta\varphi_k}{\Delta A_k}$$
$$\varphi_{V_k} = \varphi_{k-1} + \Delta\varphi'_k \qquad (6.18)$$

The estimated amplitude (A_k, φ_k) and velocity information (V_k, φ_{V_k}) will be delayed by one revolution (T_s), since one T_s is needed to sample the starting data. Moreover, no velocity can be estimated in the first two spin periods of the simulation. The following formulas will apply:

$$\begin{cases} \varphi_{A_k} = \varphi_{\underset{A_k}{\circ}} = \varphi_k \\ \varphi_{V_k} = \varphi_{k-1} + \Delta\varphi'_k = \varphi_{k-1} + tan^{-1} \dfrac{\left(1+\dfrac{\Delta A_k}{A_{k-1}}\right) sin\Delta\varphi_k}{\left(1+\dfrac{\Delta A_k}{A_{k-1}}\right) cos\,\Delta\varphi_k - 1} \cong \hat{\varphi}_{V_k} \\ \hat{\varphi}_{V_k} = \varphi_{k-1} + tan^{-1} \dfrac{A_{k-1}\Delta\varphi_k}{\Delta A_k} \end{cases} \tag{6.19}$$

and

$$\begin{cases} V_k = \dfrac{A_{k-1}}{T_s}\sqrt{2\left(1+\dfrac{\Delta A_k}{A_{k-1}}\right)(1-cos\,\Delta\varphi_k\,) + \left(\dfrac{\Delta A_k}{A_{k-1}}\right)^2} \cong \hat{V}_k \\ \hat{V}_k = \dfrac{A_{k-1}}{T_s}\sqrt{\Delta\varphi_k^2 + \left(\dfrac{\Delta A_k}{A_{k-1}}\right)^2} \\ \overset{\circ}{A}k = \dfrac{\Delta A_k}{T_s} \end{cases} \tag{6.20}$$

A number of 11 points over T_s has been found to be a good compromise in treating noisy signals. The implemented discrete sampler is in fact operating at $10/T_s\,Hz$.

The simplified analysis for a two-body system shows that the reconstructed velocity is predominantly driven by the noise. This can be easily understood: the whirl motion grows so slowly that its velocity cannot possibly be estimated with good accuracy by analyzing variations in just one spin period of $0.5\,sec$. Therefore, in order to improve the resolution of the forces the natural solution is to perform a second Fourier harmonic analysis at the whirl period T_w. This is feasible thanks to the following fact.

The solution to the eigensystem for uncontrolled whirling of a system with high quality factor can be simplified to $\pm(\omega_n/2Q)\pm i\cdot\omega_n$; the ratio of the time constant for the divergent forward whirling mode to the whirling period is therefore Q/π, i.e., the time-to-double is $0.32\cdot Q$ times larger than T_w. By using a $Q=90$ for the PGB, and its natural period of $296\,sec$, the signal doubles in $\approx 28.6\cdot Tw$ ($2.4\,hours$). This suggests that there is enough time to collect samples over the whirl period and run the filter extracting an approximate sinusoidal signal that will be very close to the marginally divergent real signal. Even if the driving velocity signal will be applicable to previous period and the whirling will have increased, we must recall that we are handling a "stabilization" problem, where a minimum gain grants stability; therefore, a slightly larger margin on the gains completely overrides the problem. Note that $Q=90$ is the lowest Q in the GG system; hence this is the fastest growing whirl instability and therefore the most difficult to handle.

The formulas for this second harmonic analysis are the same of the first Fourier filter, after substituting T_s with T_w and $\zeta_k(t_k)$ with the discretised velocity along the x and y axes. An example of the capability of this double-filter control is shown in the following pictures. A sample of $1000\,sec$ of simulated evolution of the 2-body system S/C-PGB has been considered first in the ideal condition (perfect reading and actuating sensors), then in a realistic situation

(imperfect sensors). A residual drag of $5\ 10^{-9}\ N$ DC plus $2{\cdot}10^{-9}\ N$ at orbital frequency, with 10% noise on both components, a mechanical quality factor $Q = 90$, and a non Rotating damping coefficient have been used in both the simulations; the spinning frequency is $\nu_s = 2\ Hz$. Figures 6.5÷6.8 show the results obtained in reconstructing the slow whirl velocity to be damped and demonstrate the validity of our strategy in the 2-body model case (both ideal and with realistic error sources; see Chap. 3 for experimental results on the accuracy of capacitance sensors).

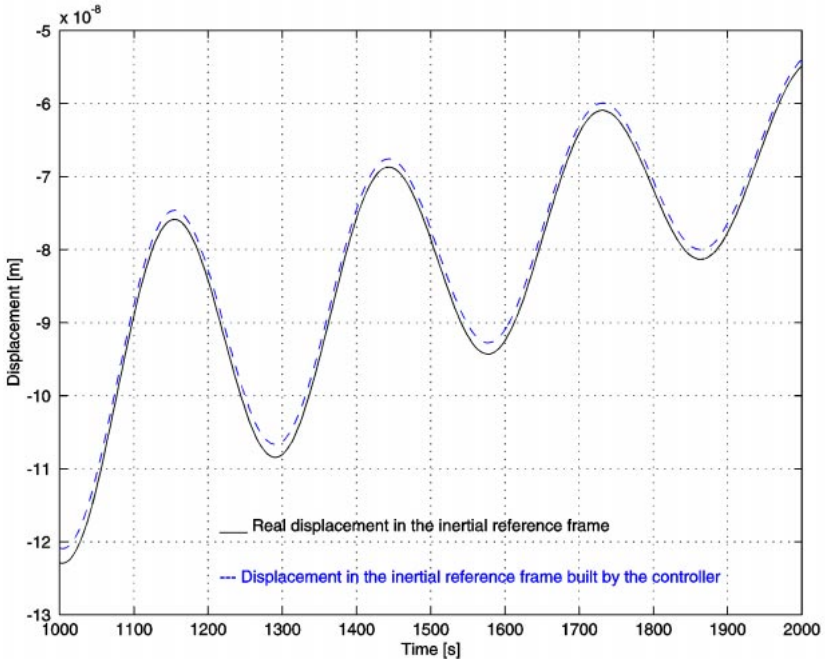

Figure 6.5 Actual relative displacement S/C-PGB in the inertial frame as predicted with DCAP, to be compared with the relative displacement as reconstructed by the controller from measurements of the rotating sensors after the first Fourier filter (ω_S filter, dashed curve); case of ideal, perfect, sensors.

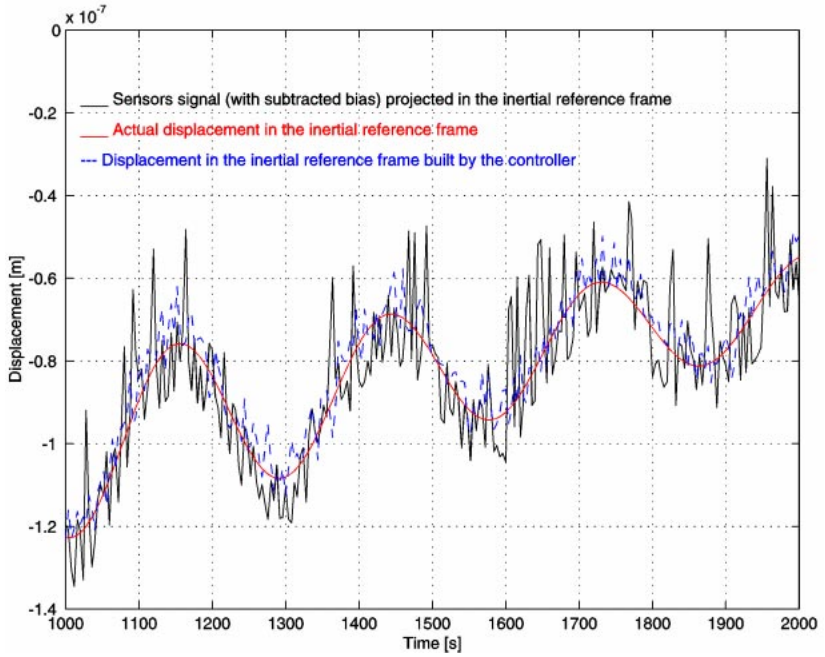

Figure 6.6 Actual relative displacement S/C-PGB in the inertial frame as predicted with DCAP, to be compared with the relative displacement reconstructed by the controller from measurements of the rotating sensors after the

first Fourier filter (ω_s filter). The errors included were: errors on sensors RMS = 10^{-2} μm, bias = 10 μm, angular bias = 1^o, RMS(ω) = 10^{-4} ω. The bias has been removed from the sensor signal curve due to the scale (10 μm vs 10^{-7} m). The improvement due to the Fourier filter is apparent: The bias is cancelled out, the RMS is partially filtered out.

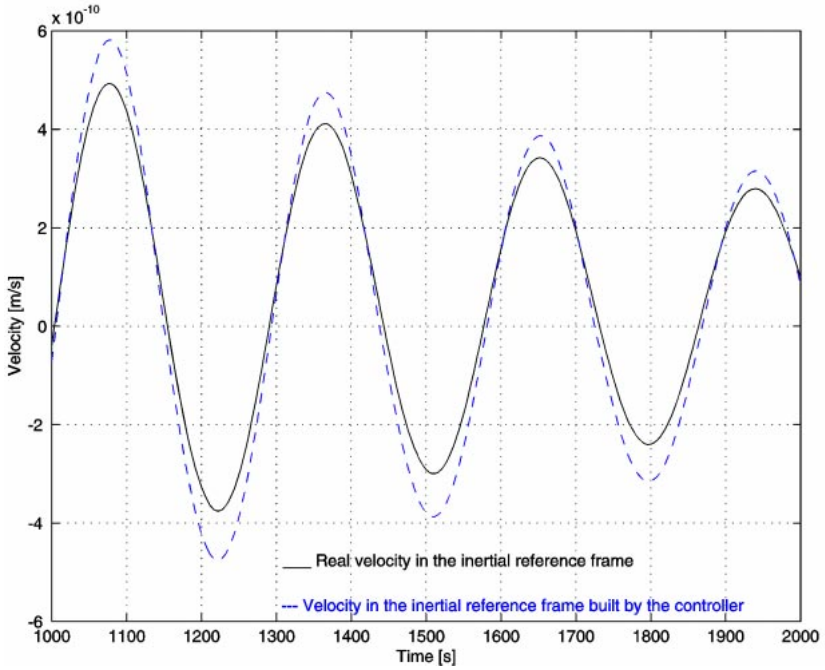

Figure 6.7 Actual relative velocity S/C-PGB in the inertial frame, as predicted with DCAP, to be compared with the relative velocity as reconstructed by the controller after the second Fourier filter (ω_w filter): case of ideal, perfect, sensors.

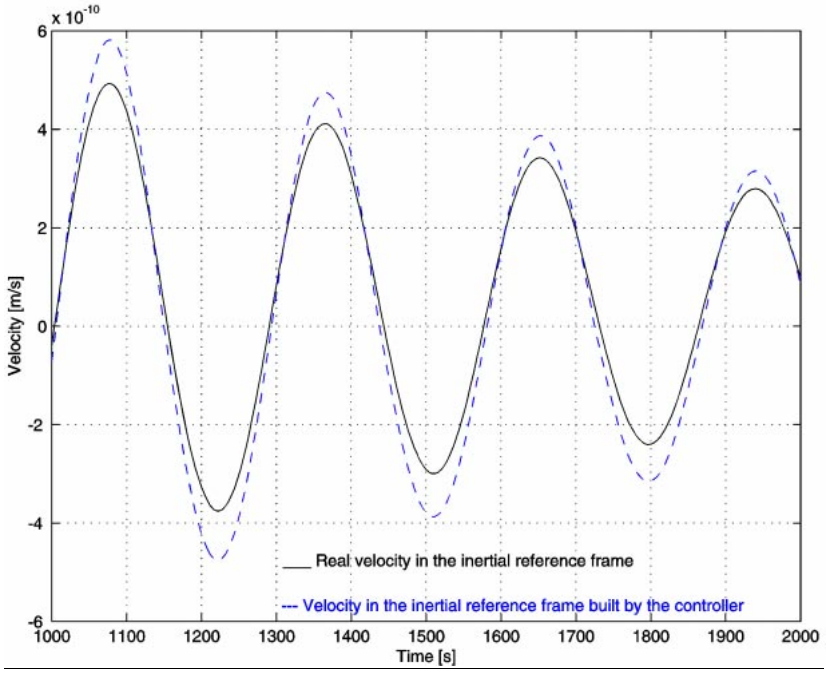

Figure 6.8 Actual relative velocity S/C-PGB in the inertial frame as predicted with DCAP, to be compared with the relative velocity as reconstructed by the controller after the second Fourier filter (ω_w filter). The errors included were: errors on sensors RMS = 10^{-2} μm, bias = 10 μm, angular Bias = 1°, RMS(ω) = 10^{-4} ω. Note that, to the scale

used, this figure is identical to the previous one, obtained with no errors; only by computing the difference of the velocities reconstructed in the two cases it is found that they are not identical. This result is very important. It shows the effectiveness of applying a second Fourier filter at the frequency of whirl in order to get rid of noise caused by error sources in the reconstruction of the whirl velocity; an accurate reconstruction of the whirl velocity is essential in order to be able to damp it without introducing large, spurious disturbances.

6.1.13 NON ROTATING DAMPING IN PULSED MODE

The continuous compensation described in Sec. 6.1.12 requires a stabilization force to be operated by the active plates in the form of a sinusoidal signal . An equivalent scheme, based on pulsed operation, has been conceived and implemented.

$$\underline{F}_{NR} = -C_{NR}\left(\dot{\underline{r}} + \underline{\omega}_s \times \underline{r}\right) \tag{6.21}$$

or, in Laplace domain (operator s) and complex notation $\left(i = \sqrt{-1}\right)$,

$$F_{NR}(s) = -C_{NR}(s + i\omega_s)\cdot r(s) \tag{6.22}$$

In order to limit the noise amplification due to the derivative term and the amplification of displacement readout biases through the ω_s term, the integral estimate of velocity and pulsed command mode are introduced. The attracting force is applied in the form of sinusoidal pulses of width $\pm\pi/4$ across velocity phase $(\varphi_V+\pi)$, with two pulses in one turn, one for each actuator as in the sketches shown next page. The pulses must be sized $2\cdot C_{NR}\cdot|V|$ in order to provide the equivalent stabilization of the continuous command. In the reference frame of the spacecraft, with the phase reference (t_0) given by sensor plate S1, the required control forces are:

$$\begin{aligned}
&\varphi_V - \frac{3\pi}{4} \le \omega_s(t-t_0) \le \varphi_V - \frac{\pi}{4} \Rightarrow \begin{cases} F_{NRx} = 0 \\ F_{NRy} = 2C_{NR}\left|\hat{V}\right| cos\,2(\omega_s t - \varphi_V) \end{cases} \\
&\varphi_V - \frac{\pi}{4} \le \omega_s(t-t_0) \le \varphi_V + \frac{\pi}{4} \Rightarrow \begin{cases} F_{NRx} = -2C_{NR}\left|\hat{V}\right| cos\,2(\omega_s t - \varphi_V) \\ F_{NRy} = 0 \end{cases} \\
&\varphi_V + \frac{\pi}{4} \le \omega_s(t-t_0) \le \varphi_V + \frac{3\pi}{4} \Rightarrow \begin{cases} F_{NRx} = 0 \\ F_{NRy} = 2C_{NR}\left|\hat{V}\right| cos\,2(\omega_s t - \varphi_V) \end{cases} \\
&\varphi_V + \frac{3\pi}{4} \le \omega_s(t-t_0) \le \varphi_V + \frac{5\pi}{4} \Rightarrow \begin{cases} F_{NRx} = -2C_{NR}\left|\hat{V}\right| cos\,2(\omega_s t - \varphi_V) \\ F_{NRy} = 0 \end{cases}
\end{aligned} \tag{6.23}$$

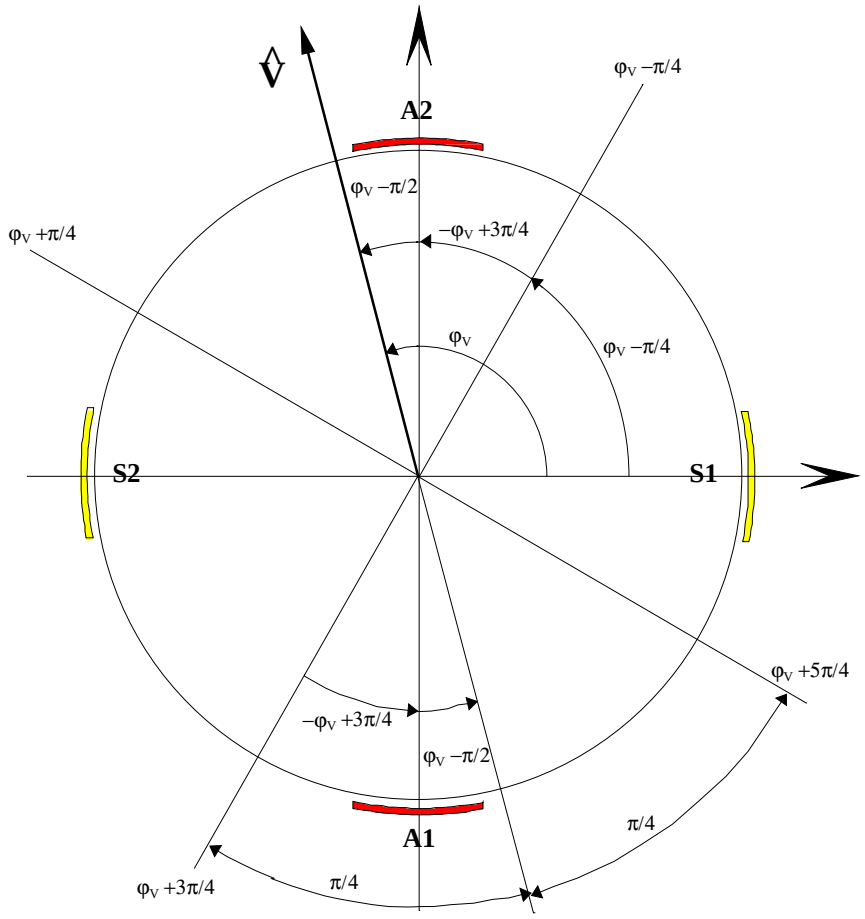

The velocity vector **V** with the reference sensor S1, and the actuators devices A1 and A2.

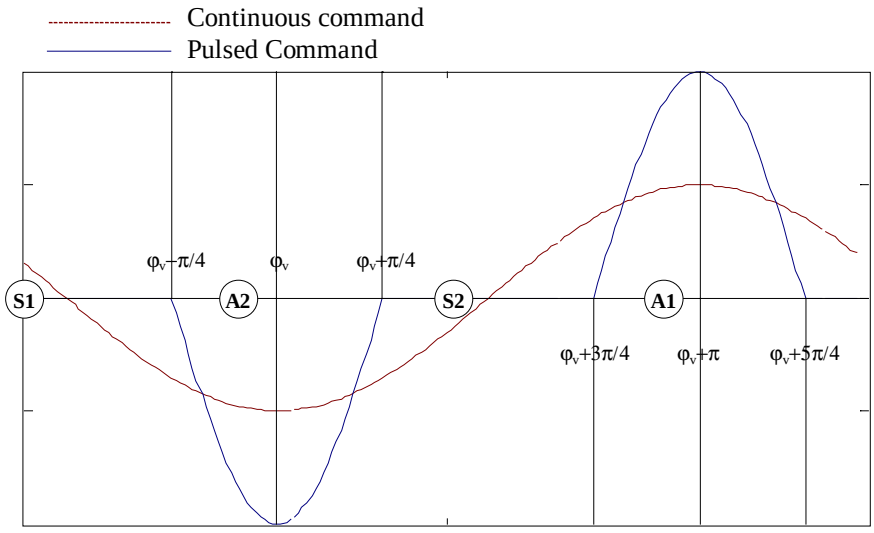

Definition of the whirl stabilization command in pulsed mode.

6.1.14 2-BODY AND 6-BODY RESULTS

In this Section we apply the control laws in order to damp whirl motions in the 2-Body model case made by the PGB laboratory and one test mass (PGB-TM) and in the full 6-body GG system. In both cases we first we assume using ideal, perfect sensors, and then introduce realist errors as follows:

- RMS of the readout capacitors $= 10^{-2}\ \mu m$
- Bias of the readout capacitors $= 10\ \mu m$
- Angular Bias of the readout capacitors $= 1^{o}$
- RMS of the Earth Elevation Sensor, RMS$(\omega_s) = 10^{-4}\ \omega_s$.
- $\varepsilon = 1\ \mu m$ (initial offset of the spring)

Let us first consider the 2-body system PGB-TM which has: $m_{PGB} = 43.647\ kg$, $m_{TM} = 10\ kg$, $\omega_s = 2\ Hz$, $k = 0.02\ N/m$, $Q = 500$, $C_{NR} = 0.009\ Ns/m$. Note that this value for the coefficient of non rotating damping C_{NR} is about 11 times larger than the minimum value required for stability. This allows us to damp the system more rapidly, hence saving CPU time; the smallest coefficient we have tested was a factor 2.5 larger than the minimum and was enough to stabilize the system. The residual drag acting on the PGB has a DC component equal to $1.72\ 10^{-9}\ N$; plus an orbital frequency term which is 40% of the DC component and a 10% of noise on both components (which are the scaled values of the 6-body system).

All plots are shown in the non rotating frame.

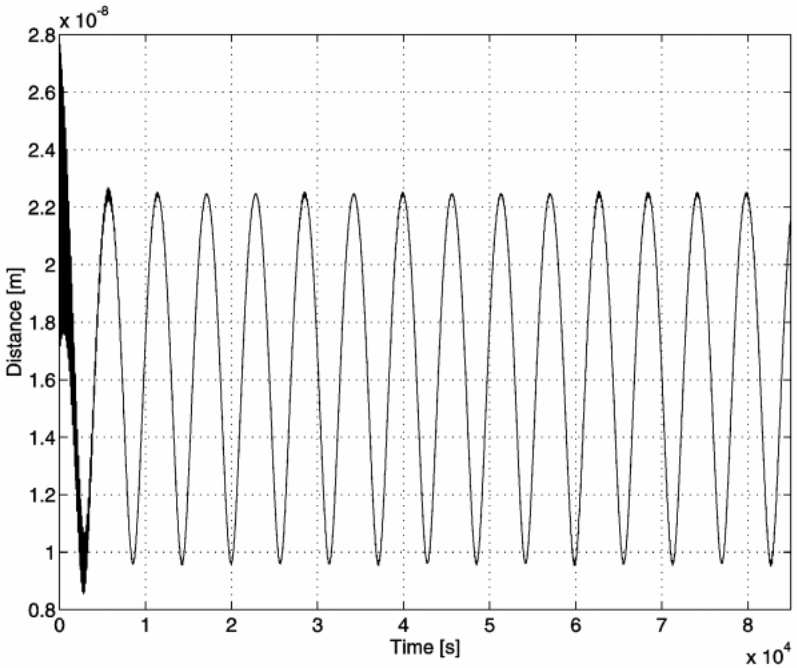

Figure 6-9 One day simulation of the 2-body PGB-TM system showing their relative distance (ideal case). Oscillations at orbital period are due to the oscillating term of the drag; the offset from the X axis is due to the DC term of the drag which displaces the equilibrium position of a fixed vector along X. The short period oscillations (see Fig. 6.10 for a close up), represent the whirl motion and decay in few thousand seconds.

This test of the ideal case was an important check of the principles of the whirl control: the results are in perfect agreement with the theoretical predictions, confirming the validity of the control law.

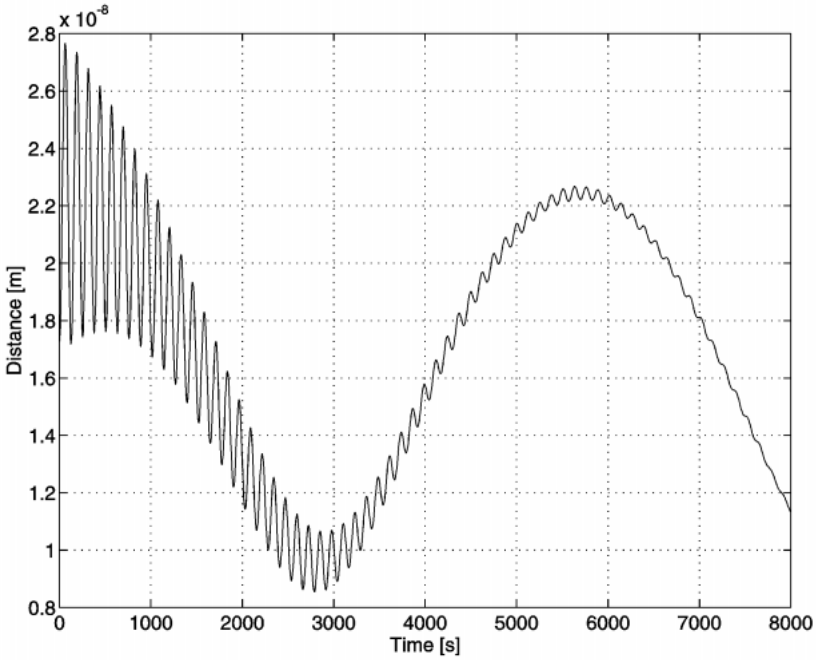

Figure 6.10 Short sample from the one-day simulation of the ideal 2-body PGB-TM system shown in Fig. 6.9: the rapid decay (over a few thousand seconds) of the short periodic whirl oscillations is apparent.

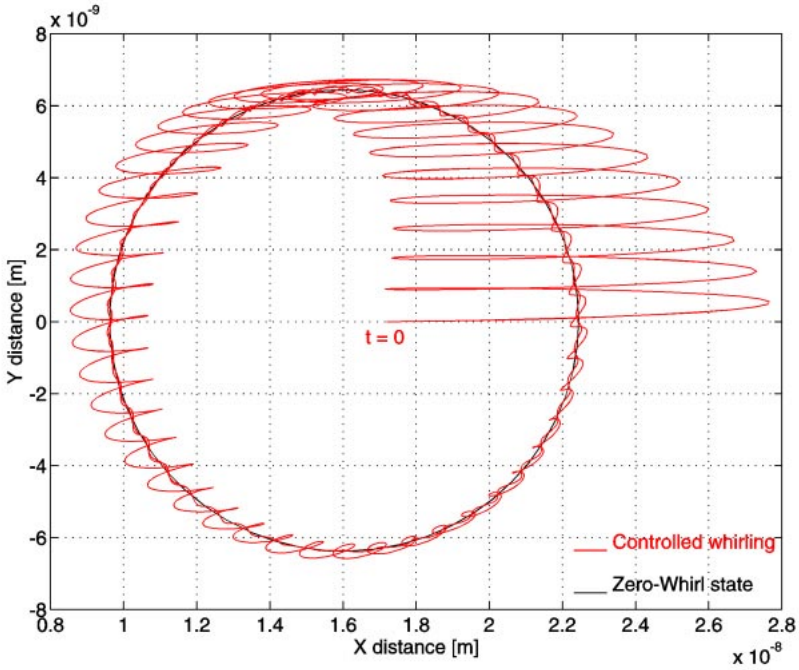

Figure 6.11 Sample of 15000 sec from the one day simulation of the ideal 2-body PGB-TM system shown in Fig. 6.9. This polar plot shows the approaching of the test mass to its ideal "equilibrium circle" caused by the residual drag force, and corresponding to a non dissipating spring (no whirl motion, infinite quality factor). The constant displacement along the X axis is caused by the DC term of air drag.

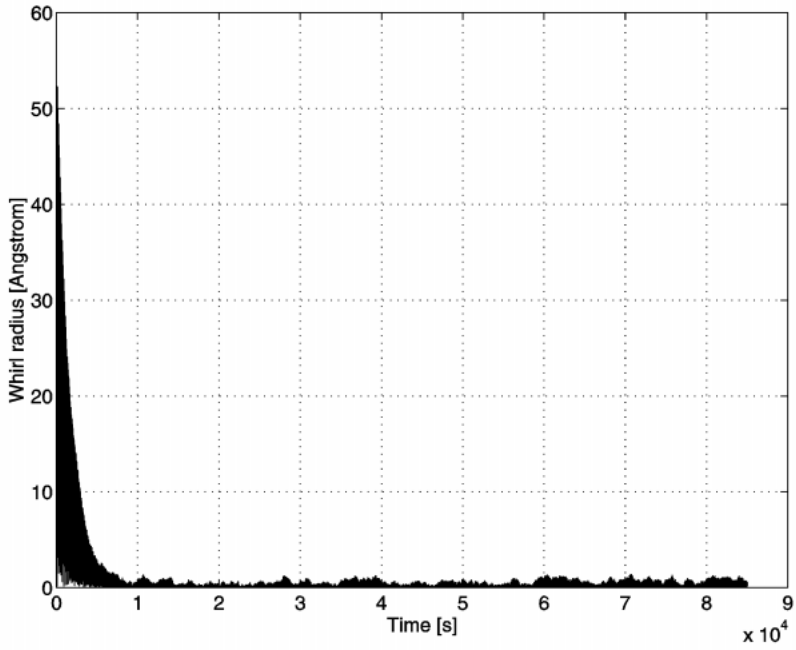

Figure 6.12 One day simulation of the ideal 2-body PGB-TM system as in Fig.6.9. Here we plot the whirl radius, which reduces to one or two Angstrom after 6000-7000 sec only.

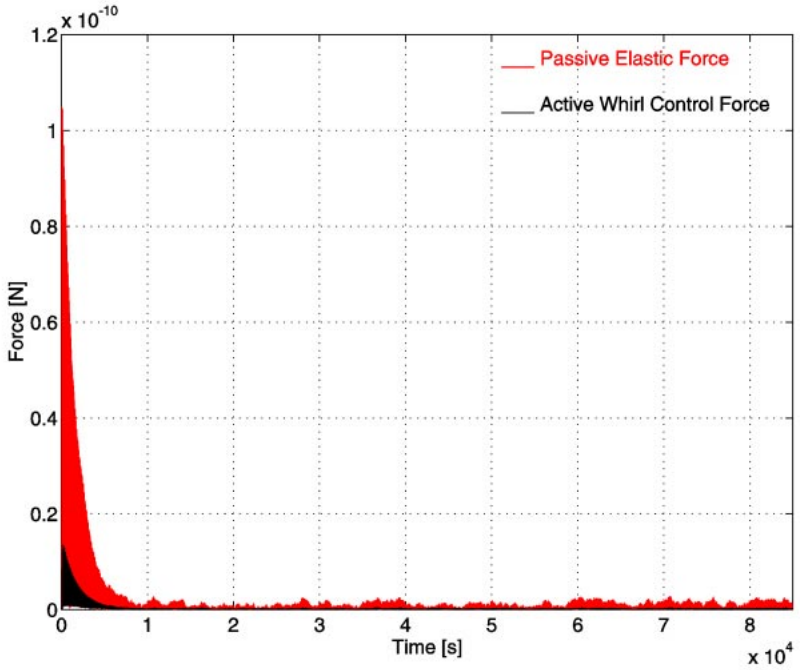

Figure 6.13 One day simulation of the ideal 2-body PGB-TM system as in Fig. 6.9. Here we plot the passive elastic force of the spring for comparison with the active force of the control. Note that in these simulations the active force was taken to be 11 times larger than the minimum value required to provide stability, so as to speed up the simulations. We have checked that a force only 2.5 times larger than the minimum does stabilize the system, obviously less rapidly.

We now introduce realistic noise sources as listed at the beginning of this Section.

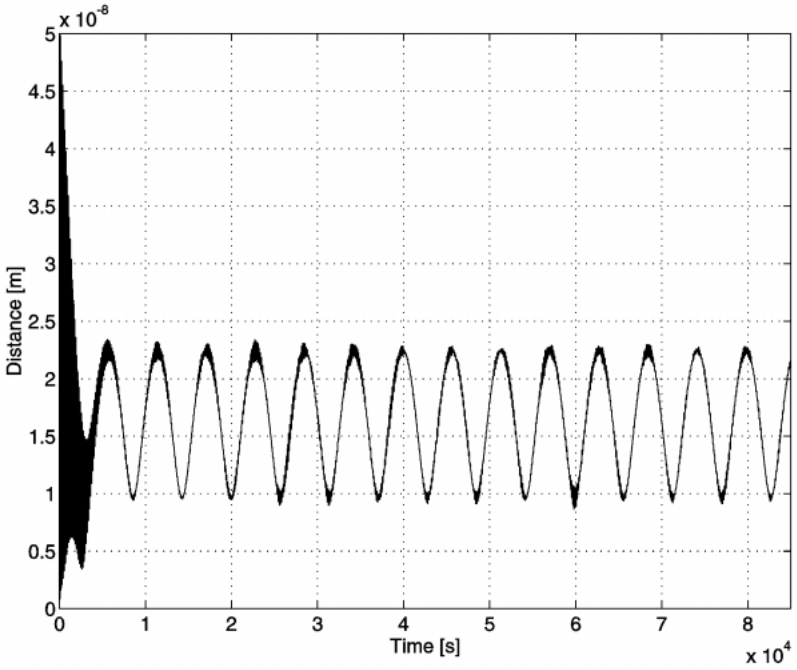

Figure 6.14 One day simulation of the 2-body PGB-TM system with realistic error sources. Oscillations at orbital period are due to the oscillating term of the drag; the offset from the X axis is due to the DC term of the drag which displaces the equilibrium position by a constant amount along X. The short period oscillations (see Fig. 6.15 for a close up) represent the whirl motion and decay in few thousand seconds.

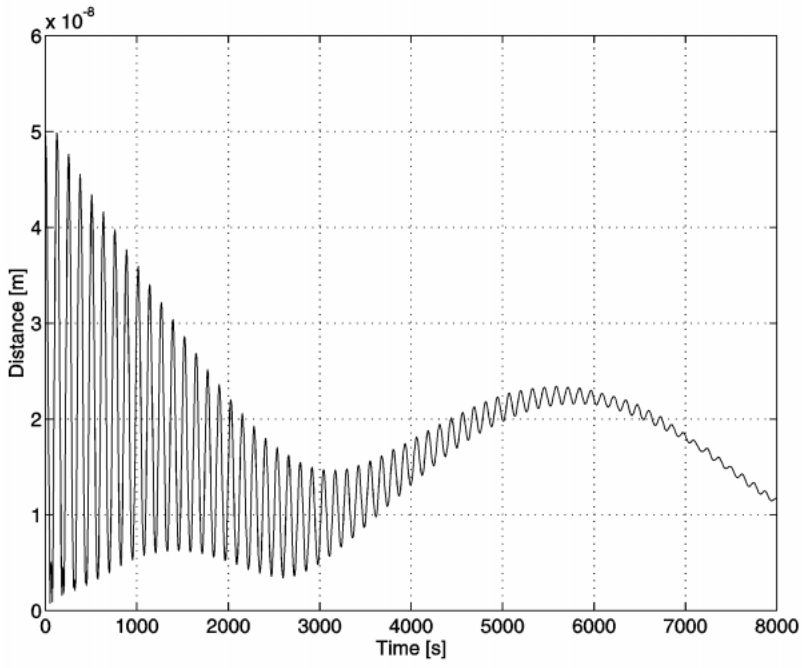

Figure 6.15 Sample from the one-day simulation of the realistic 2-body PGB-TM system as in Fig. 6.14. The short period oscillations are the whirl oscillations, which decay in a few thousand seconds.

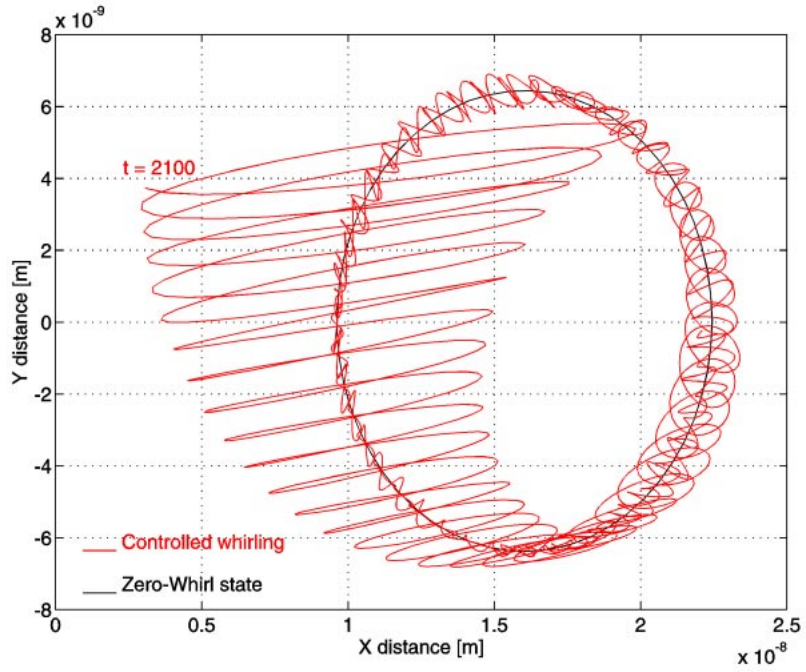

Figure 6.16 Sample of 15000 sec from the one day simulation of the realistic (noisy) 2-body PGB-TM system as in Fig. 6.14. This polar plot shows the approaching of the test mass to the ideal "equilibrium circle" due to the variations of the residual drag force, and corresponding to a non dissipating spring (infinite quality factor, no whirl motion). Note that the scales on the two coordinate axes are different (the zero whirl "circle" is therefore distorted).

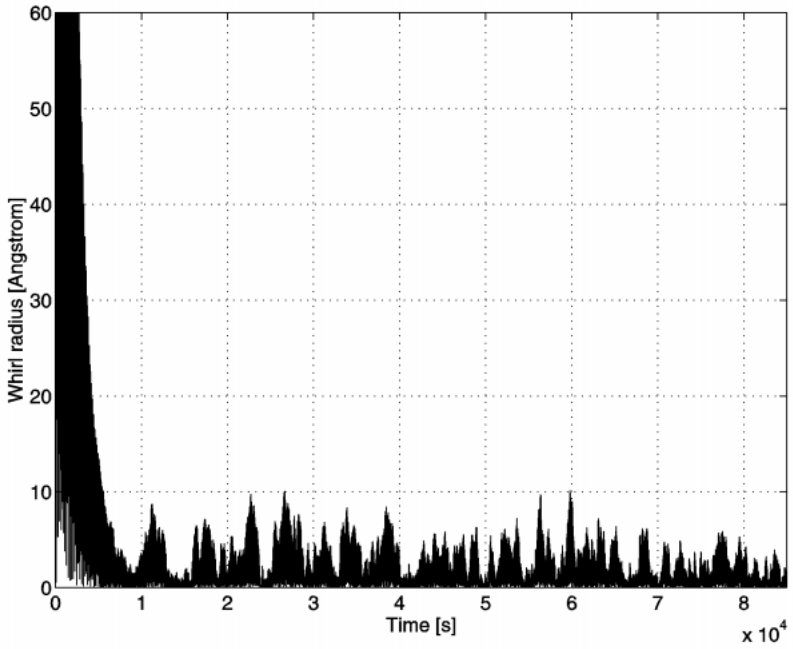

Figure 6.17 One day simulation of the realistic (noisy) 2-body PGB-TM system as in Fig. 6.14. Here we plot the whirl radius, which reduces to a few Angstrom after 7000-8000 sec only.

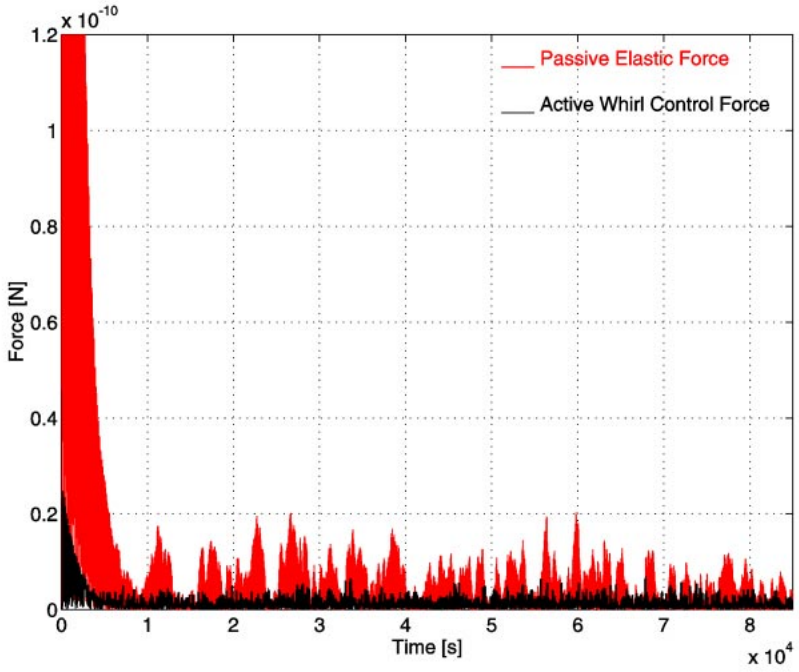

Figure 6.18 One day simulation of the realistic (noisy) 2-body PGB-TM system as in Fig. 6.14. Here we show the passive elastic force of the spring for comparison with the active force of the control. We recall that, in order to speed up the simulations, we apply an active force 11 times larger than the minimum needed for stabilization, and that an active force only 2.5 times larger than the minimum has been tested and found to be sufficient.

The 2-Body PGB-TM results show an impressive agreement between the ideal case and the case with realistic errors. We are therefore led to apply the same control laws to the full *6*-Body GG system, both in *2* and in *3* dimensions. We have: $m_{s/c} = 122.071$ *kg*, $m_{PGB} = 43.647$ *kg*, $m_{TM} = 10$ *kg*, $\omega_s = 2$ *Hz*, $k = 0.02$ *N/m*, $Q_{PGB} = 90$, $Q_{TM} = 500$, $C_{NR}(PGB) = 0.05$ *Ns/m*, $C_{NR}(TM) = 0.009$ *Ns/m* (as above, this is about *11* times larger than the minimum value required for stability). The residual drag acting on the spacecraft has a DC component equal to $5 \cdot 10^{-9}$ *N* plus an orbital frequency term which is *40%* of the DC component and a *10%* noise on both components. We have compared the ideal case (perfect sensors) with a realistic case where:

- RMS of the readout capacitors $= 10^{-2}\ \mu m$
- Bias of the readout capacitors $= 10\ \mu m$
- Angular Bias of the readout capacitors $= 1^o$
- RMS of the Earth Elevation Sensor, $RMS(\omega_s) = 10^{-4}\ \omega_s$
- $\varepsilon = 1 \mu m$ (initial offset of the springs)

All plots are shown in the non rotating frame. The gimballed arms were modeled without rings (see Sec. 6.1.10).

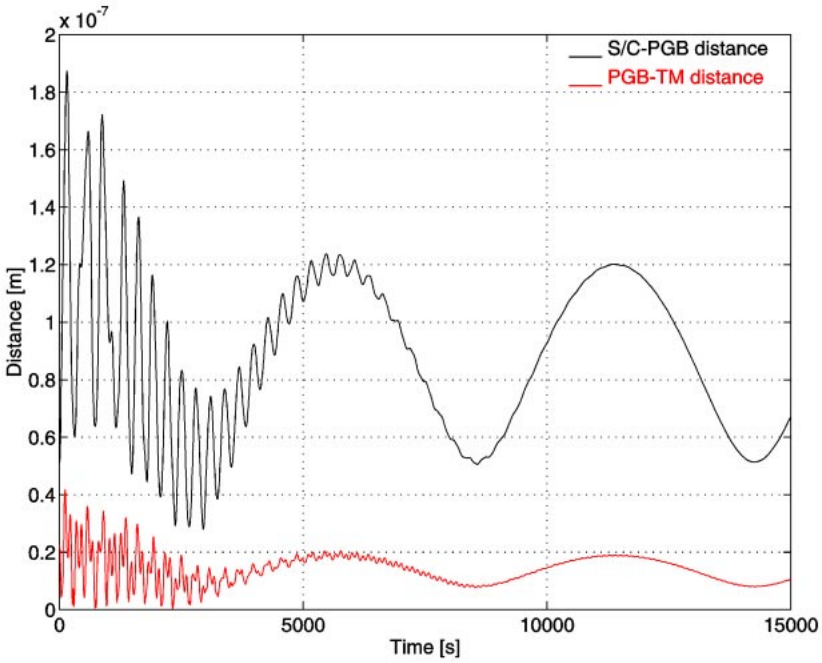

Figure 6.19 Ideal 6-body GG system. Simulation of 15000 sec. The figure shows the distance between the PGB and the spacecraft, and the distance between the external test mass and the PGB. There are three types of oscillations: one is at the orbital period, due to the component of the drag at this frequency, another is at the whirl period of the PGB (controlled), and the one with the shortest oscillation period is the controlled whirl motion of the test mass. The offset of the distances with respect to the X axis is due to the DC component of the drag force.

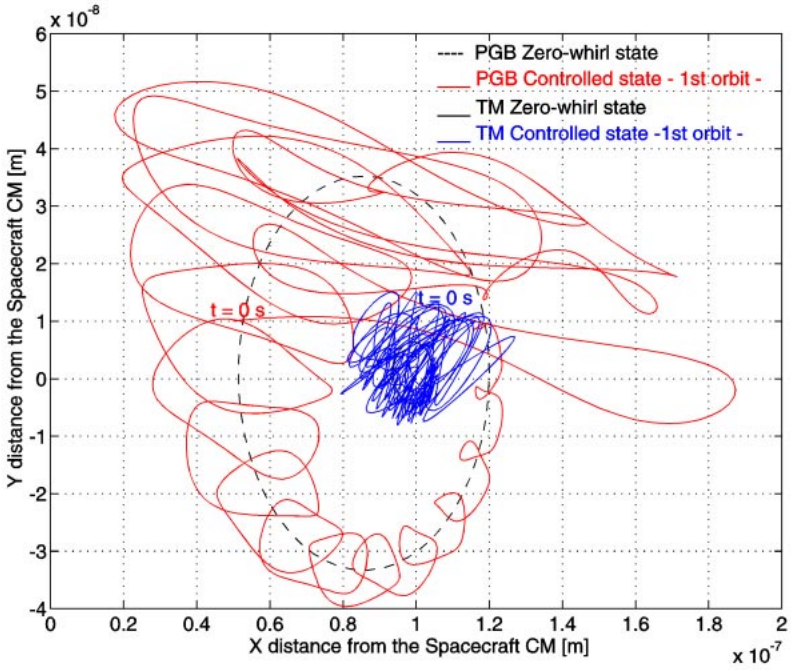

Figure 6.20 Ideal 6-body GG system. Polar plot showing the motion of the PGB and of the external test mass with respect to the center of mass of the spacecraft (0,0) during the first orbit (6000 s). The whirl motions start to be damped, but still need some time. Note that the scales on the two coordinate axes are different (the zero whirl "circle" is therefore distorted)

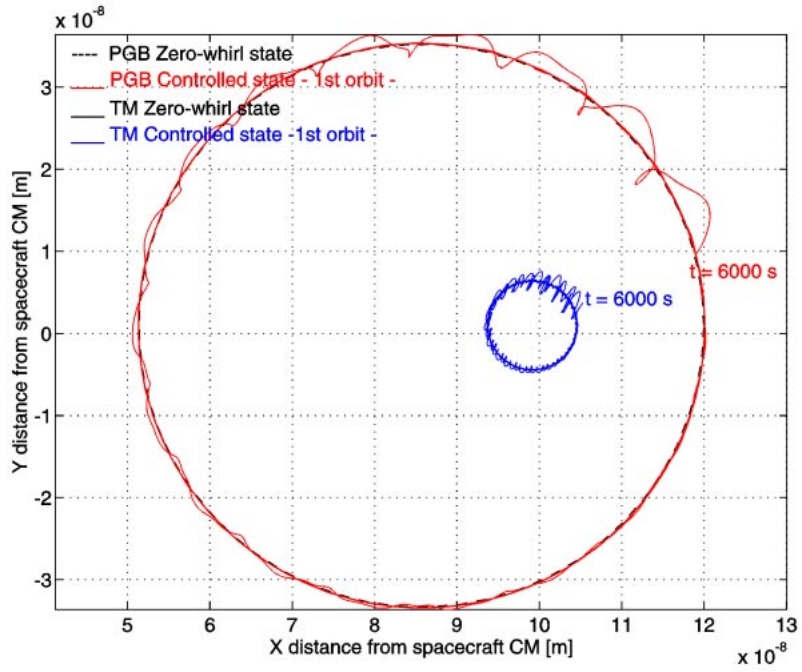

Figure 6.21 Ideal 6-body GG system. Polar plot showing the motion of the PGB and of the external test mass with respect to the spacecraft center of mass (0,0) during 9000 sec after the first orbit. It is now apparent that the whirl motions are damped and that the bodies are already very close to their zero-whirl orbits (the circles in this polar plot)

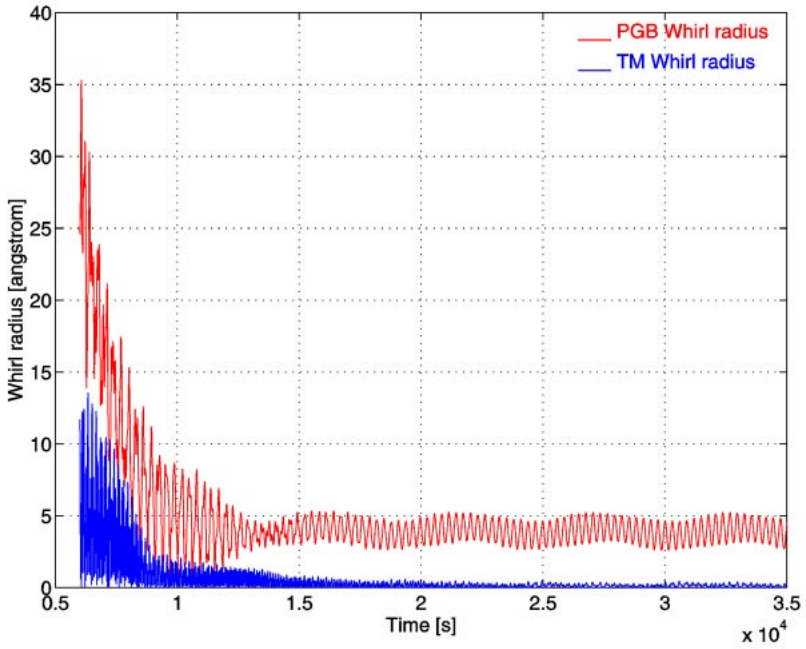

Figure 6.22 Ideal 6-body system. Here we plot the whirl radii of the PGB and of the external test mass for the same time interval as in Fig. 6.21.

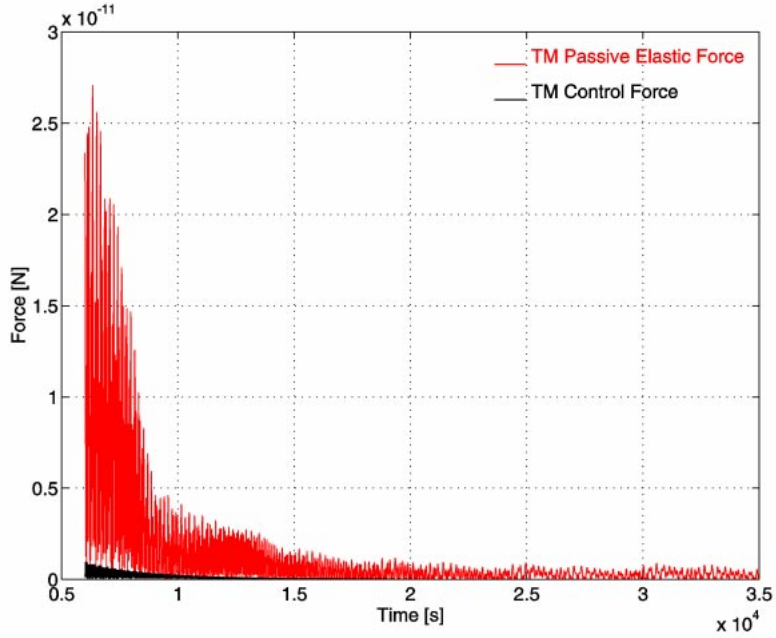

Figure 6.23 Ideal 6-body GG system. Here we plot the passive elastic force for comparison with the active control force in the case of the external test mass. The value of C_{NR} , the coefficient of non rotating damping applied to the test body, is 0.009 Ns/m, which is about 11 times larger than the minimum required value. A force 2.5 times larger than the minimum was found to be sufficient.

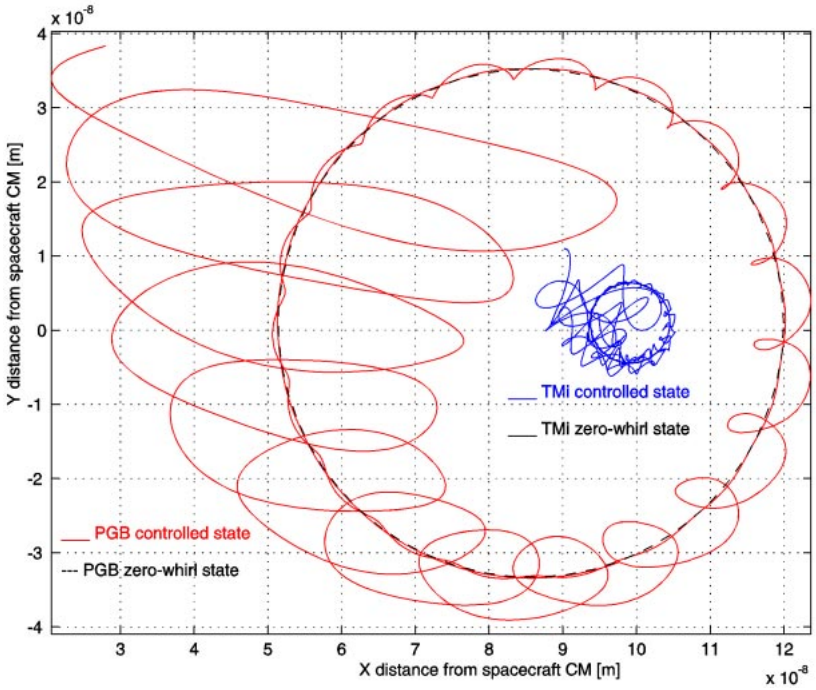

Figure 6.24 Ideal 6-body GG system with all degrees of freedom (3D simulation). No sensor noise applied (ideal case). The residual drag amounts to $5 \cdot 10^{-9}$ N (DC), and $2 \cdot 10^{-9}$ N at orbital frequency (T_{orb}=5701.64 s), with 10% noise. It is applied only in the xy plane; there is no external forcing term acting along the z-axis. As compared to the planar case, the additional degrees of freedom are shown not to produce any changes in the dynamics. However, the required computing time is much bigger, particularly if sensor noise is taken into account.

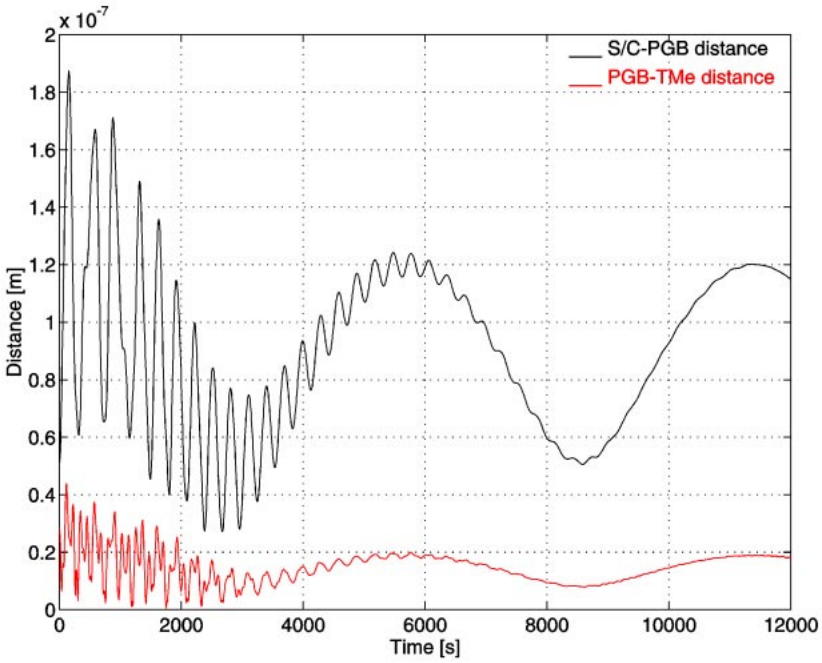

Figure 6.25 The 6-body GG system with noise as given in the text.. Simulation of 12000 sec. The figure shows the distance between the PGB and the spacecraft and the distance between the external test mass and the PGB. As usual, there are three types of oscillations: one at the orbital period, due to the orbital component of the drag (the longest period), another with the whirl period of the PGB (controlled), and an even shorter one at the whirl period of the TM (also controlled) .The offset of the distances with respect to the X axis is due to the DC component of the drag force.

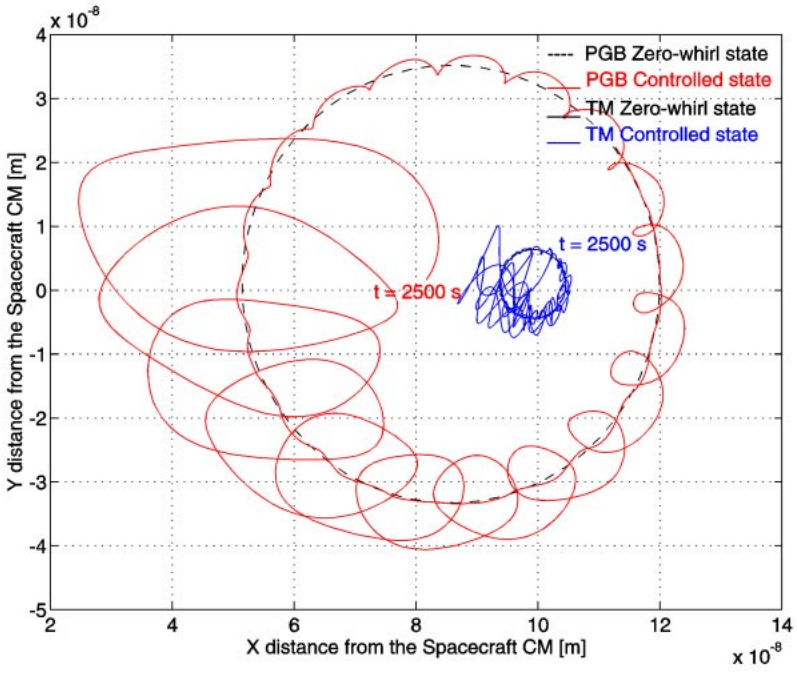

Figure 6.26 The 6-body GG system with realistic noise (see text). This polar plot shows the motion of the PGB and of the external test mass with respect to the center of mass (0,0) of the spacecraft for 9500 sec after the first 2500 sec.

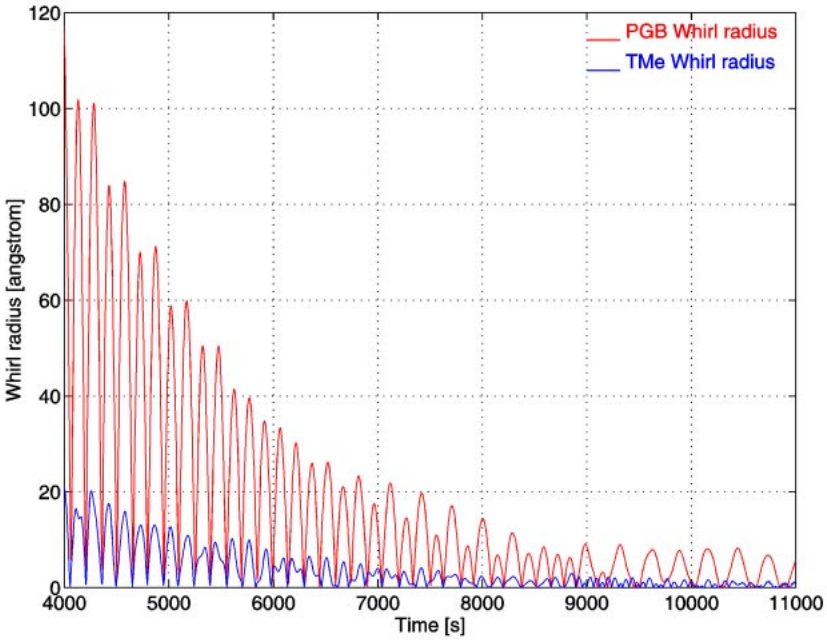

Figure 6.27 The 6-body system with realistic noise (see text). We plot the whirl radius of the PGB and of the external test mass after the first 4000 sec. These values are in very good agreement with the theoretical predictions and the expected self centering.

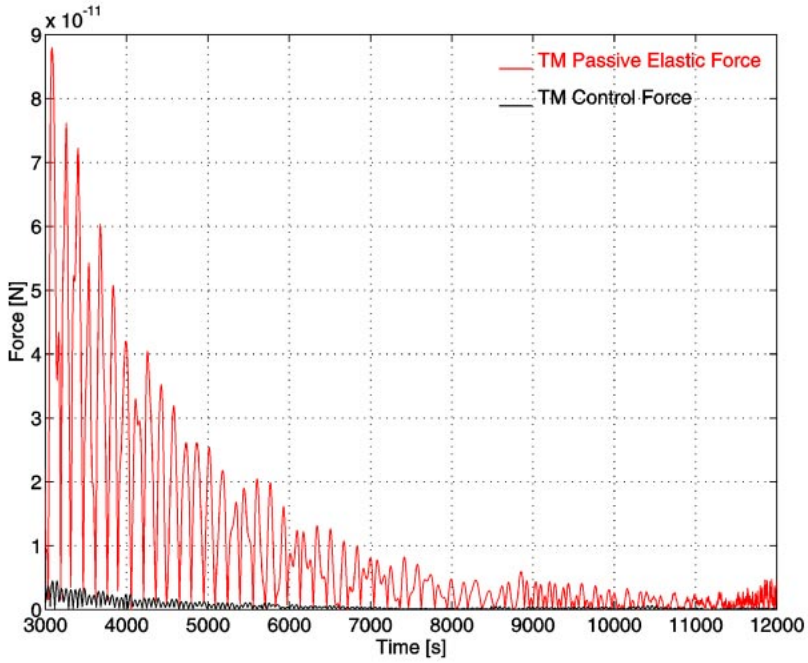

Figure 6.28 The 6-body GG system with realistic noise (see text). Here we plot the passive elastic force of the spring for comparison with the control force acting on the external test mass. The value of the C_{NR} coefficient of non rotating damping applied to the test body is 0.009 Ns/m, which is about 11 times larger than the minimum required value. We have checked that an active force only 2.5 times larger than the minimum could stabilize the system.

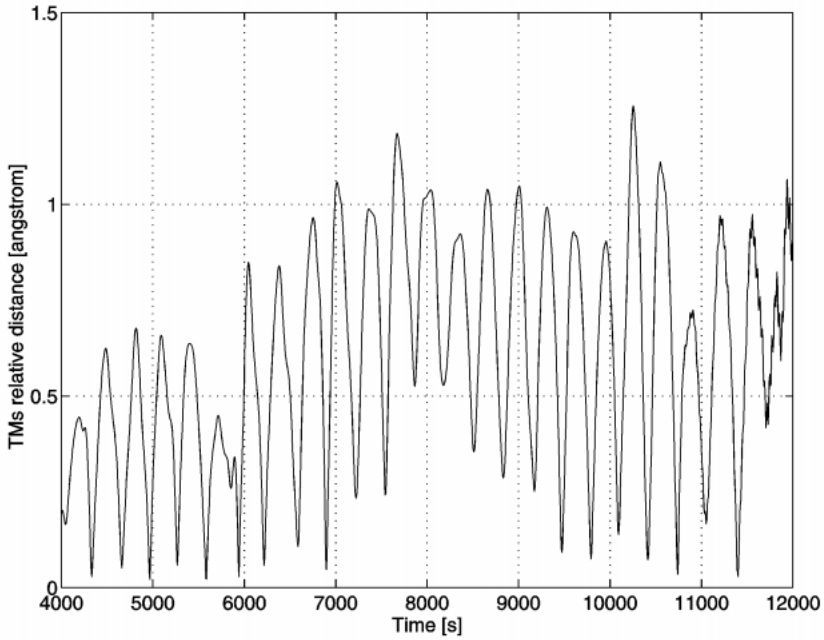

Figure 6.29 The 6-body GG system with realistic noise (see text). Here we plot the relative displacement between the inner and the outer test mass (differential displacement) obtained after applying the active control of their whirl motions as outlined in the previous sections (by double Fourier analysis). Note that in this simulation the whirl control is always on, i.e. this is a worst case simulation because whirl control can in fact be switched off during scientific data acquisition (see Sec. 2.1.5). Yet, this result is impressive in that it shows how active control by means of electrostatic sensors/actuators can be so accurate as to make the GG test bodies (macroscopic rotors of 10 kg each) self-center on one another as expected in supercritical rotation in absence of dissipation (infinite mechanical quality factor, zero-whirl). Achieving such a small separation of the test bodies is very important in order to reduce classical disturbing effects (such as Earth tides). Note that –although very small indeed– this relative displacement is still 160 times larger than the one expected in case of an EP violation to the level of 1 part in 10^{17} (see Eq. 2.2), which is the target of the GG mission. However, in the non-rotating reference frame (as in Fig. 6.26) the signal appears –after synchronous 2-phase demodulation at the 2 Hz spinning frequency– as a constant displacement always along the direction to the center of the Earth (indicated as the Y axis in Fig. 6.26 and as the X axis in Fig. 2.21); to the contrary, the whirl motion (shown in Fig. 6.26) which gives rise to the separation plotted here as function of time, has a distinct frequency, namely the natural frequency of the whirl (as it is apparent). This allows us to separate the relative displacement signal.

In summary, this work demonstrates that the whirl control problem of the complete GG system can be solved in realistic conditions. It is worth stressing that the results obtained in the presence of noise sources are especially good for the test masses because, while in the ideal case the active control force is, by the definition the same on both of them (common mode), this is obviously no longer the case when noise is introduced; it is therefore a very good feature of the controller designed here that of being able to avoid the onset of any spurious differential force between the test bodies. Having achieved the results shown in Fig. 6.29, it is possible to proceed to the recovery of the expected EP signal as discussed in Sec. 2.1.7, Fig. 2.21

6.1.15 DRAG FREE CONTROL

So far we have applied the active control of whirl motions in the presence of a residual drag force assuming that air drag acting on the spacecraft has already been compensated. This is the task of the drag-free control. In this Section we present our current design for the DRAG FREE CONTROL (DFC) of the GG satellite and test it in combination with the control of whirl motions. We do so first in the *2*-body model PGB-Spacecraft and then in the full 6-body model of GG, both in the case of ideal, perfect sensors and in the case of realistic errors. The basic features of the GG drag free control are:

- The largest drag force acting on the GG spacecraft (in the inertial frame) is at the orbital frequency $\nu_{orb}=1/5701.64\ Hz = 1.75388\cdot10^{-4}\ Hz$; its amplitude is $150\ \mu N$, with a noise amounting to *10%* of it
- The DFC designed for GG is a notch filter at the orbital frequency ν_{orb}; the bandwidth is narrow so that it does not affect the dynamics of the system
- The DFC force is (in the inertial reference system):

$$\underline{F}_{DFC}(s)=\frac{K_{NF}\,s}{s^2+2\zeta\omega_{orb}s+\omega_{orb}^2}\,\underline{x}(s) \tag{6.24}$$

with $\omega_{orb}=2\pi\nu_{orb}$ and ζ the "damping" of the DFC, which describes its bandwidth; $\underline{x}(s)$ is the relative displacement in the inertial reference system.

- The gain and damping of the notch filter are, respectively, $K_{NF} = 4\ 10^{-4}\ N/s$ and $\zeta = 10^{-7}$.
- The DFC reads the inertial $\underline{x}(s)$ built from the Whirl Control, and the F_{DFC} force defined in the inertial reference system is then transformed into the rotating one.
- The transfer function which defines the DFC, $F_{DFC}(s)/x(s)$, is discretised by a bilinear transformation with pre-warp frequency equal to the orbital frequency and sampling time equal to the spin period of the spacecraft (because $x(s)$ is rebuilt by the whirl control at each spin period).
- The resulting rotating force is applied to the spacecraft by the FEEP thrusters.

The results are shown in the following figures; all plots are in the inertial (not rotating) frame of reference. The whirl control is always on, although the time-span of the simulation is always too short –given the initial very high level of drag– for the whirl motions to be damped; here the relevant issue is whether the DFC is effective in reducing the amplitude of the effect of drag at the orbital frequency, which it is.

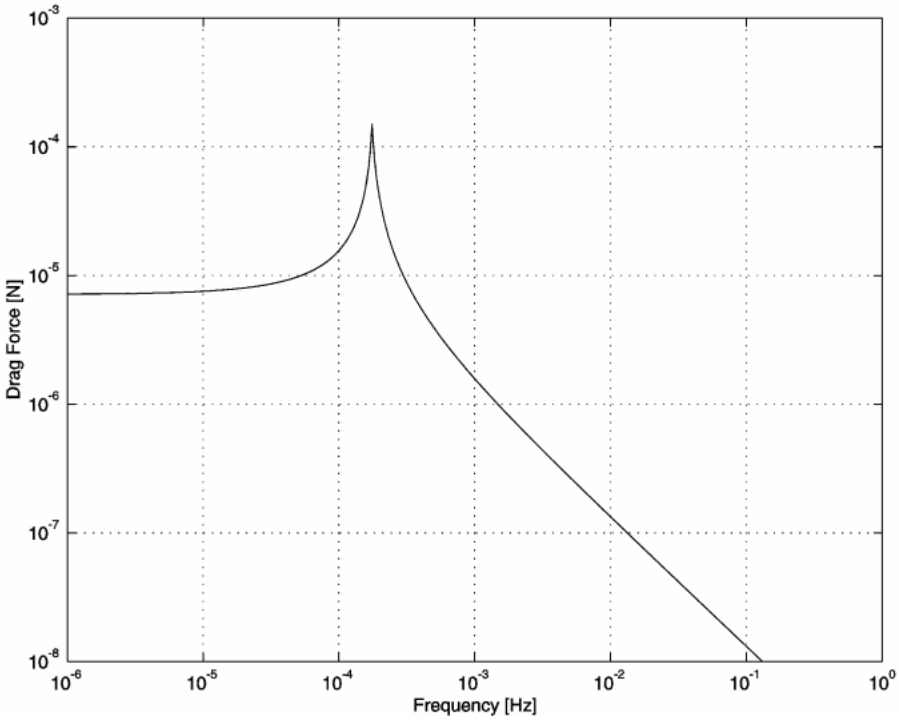

Figure 6.30 Simplified model of the drag force used in the simulations of the DFC: drag along the x axis

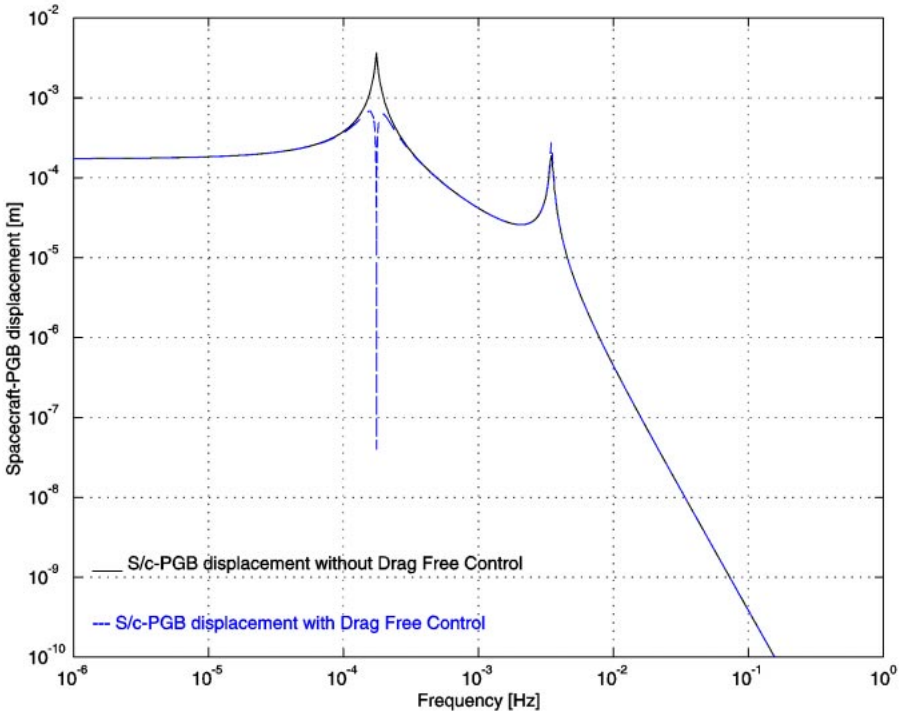

Figure 6.31 Theoretical relative displacement between the PGB and the spacecraft (2-Body model) without (continous curve) and with (dashed curve) the application of drag free control; (m_s=122.07 kg, m_p=63.647 kg, ν_s=2 Hz, Q=90).

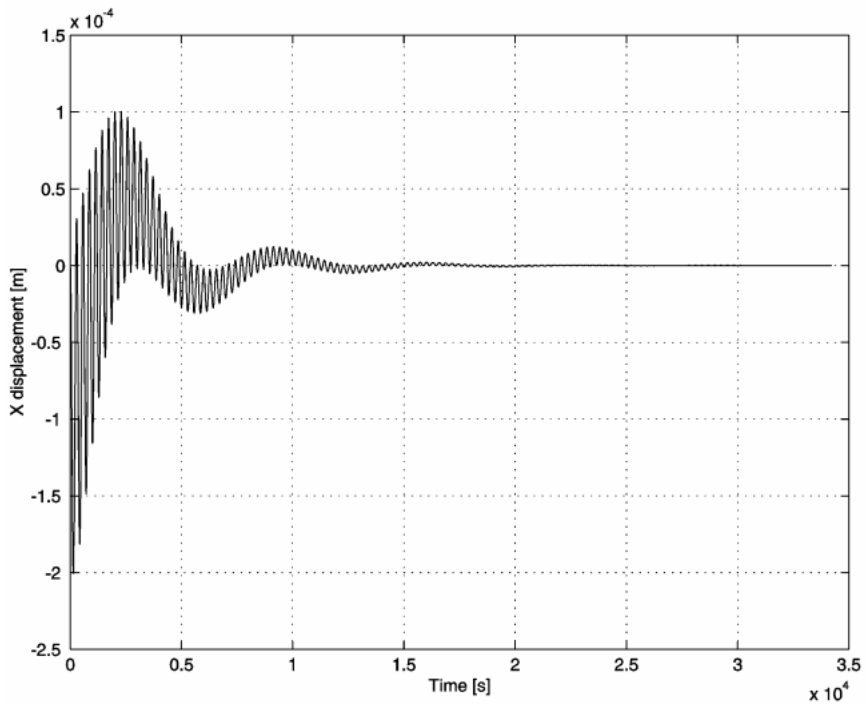

Figure 6.32 Relative displacement in the PGB-Spacecraft 2-body model with DFC applied (data as in Fig. 6.31) and the addition of some error sources as follows: RMS(capacitance sensor)=10^{-2} μm, Bias(capacitance sensor) =10 μm, Angular Bias(capacitance sensor) = 1^{o}, RMS(ω) = 0. Drag = 1.5 10^{-5} N at orbital frequency (T_{orb}=5701.64 s) in the inertial reference frame, with 10% noise. The reduction of the amplitude of the displacement at the orbital frequency has been tested also with larger values of Drag (1.5 10^{-4} N). In this simulation FEEP thrusters and Earth sensors are assumed to be perfect (no error).

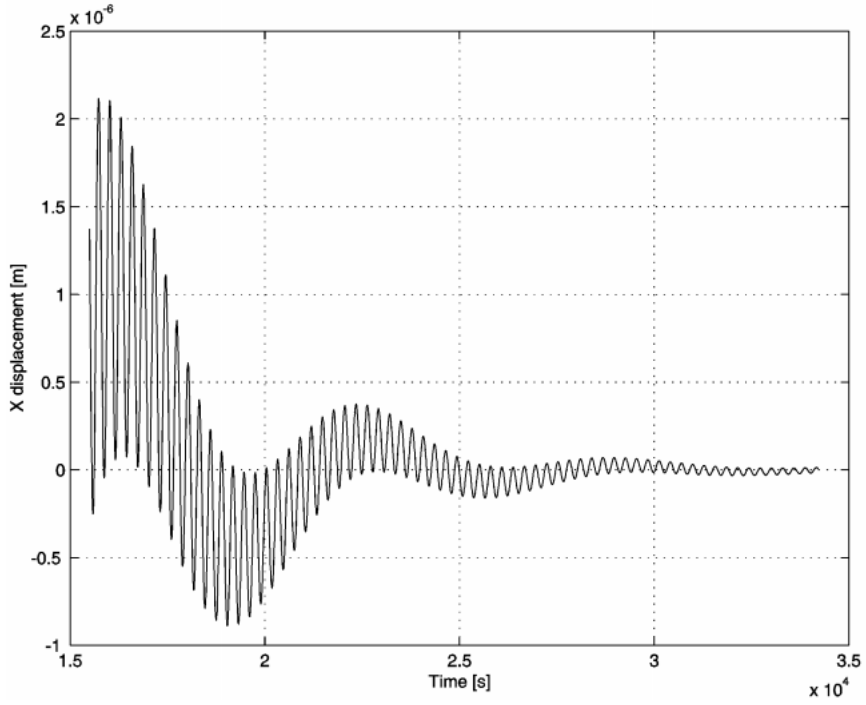

Figure 6.33 A detail from the previous plot showing how the drag free control is effective in reducing the amplitude of the relative displacement in just a few orbital periods of the satellite around the Earth.

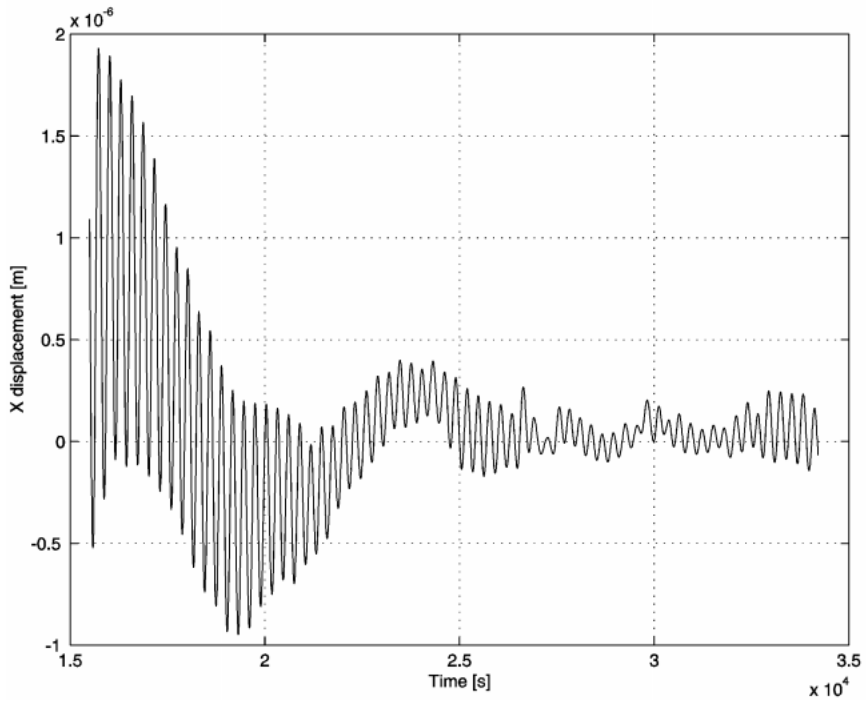

Figure 6.34 Relative displacement in the PGB-Spacecraft 2-body model with DFC applied and the addition of noise sources as follows: RMS(capacitance sensor)=10^{-2} μm, Bias(sensor) =10 μm, Angular Bias(sensor) = 1°, Earth Elevation Sensor RMS(ω) = 10^{-5} ω, RMS(FEEP) = $5 \cdot 10^{-9}$ N (at 20 Hz), BIAS(FEEP) = $5 \cdot 10^{-9}$ N. Drag = 1.5 10^{-5} N at orbital frequency (T_{orb}=5701.64 s) with 10% noise.

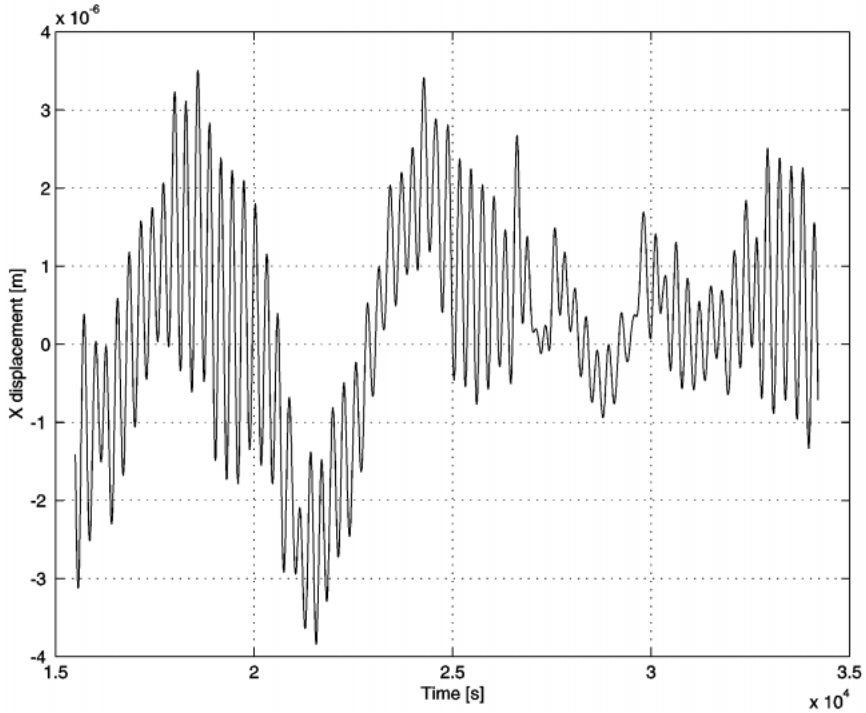

Figure 6.35 Same as the previous plot except for the error assumed for the Earth Elevation Sensor, now a factor of 10 worse than in Fig. 6.34: RMS(ω)=10^{-4}ω

Figs. 6.34 and 6.35 show the dependence of the DFC performances from the sensitivity of the Earth Sensor: this is due to the last operation of the DFC, which needs to transform the force

from the inertial to the rotating frame where the actuators (FEEP) operate. The following figure shows the result of the simulation for the 6-body GG system, indicating that the DFC works just as well as in the 2-body case, save for the fact that it is much more demanding in terms of CPU time needed to run the simulations. Therefore, in the full system we have used the lower Earth sensor noise in order to show a significant reduction of drag already in first 2 orbital periods. Our purpose was to show that the current design of the DFC is adequate to reduce drag at the orbital frequency.

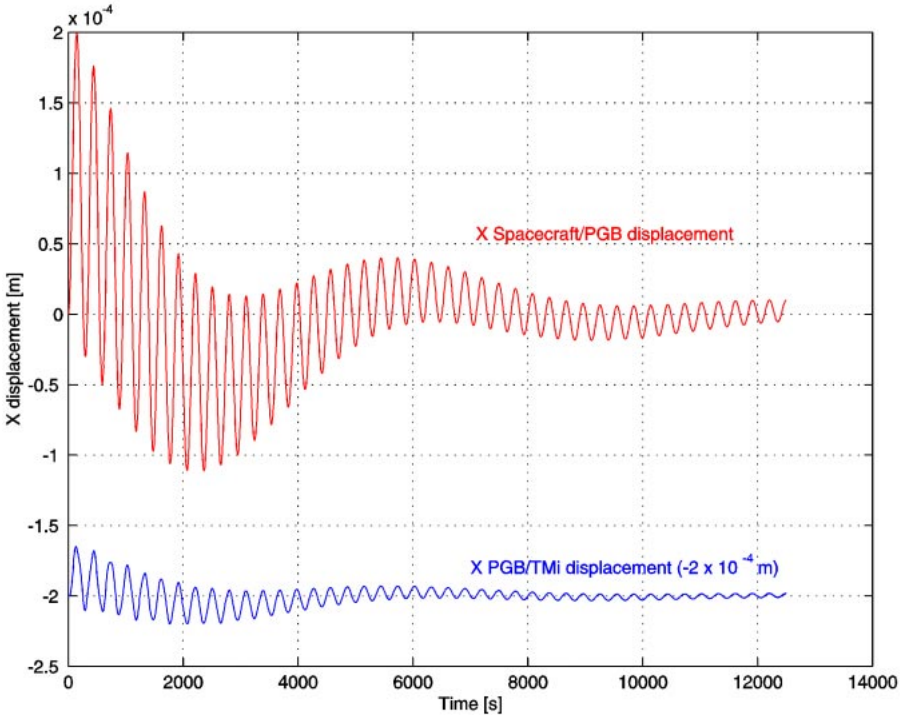

Figure 6.36 The GG 6-body system simulated with DFC for about two orbital periods. The noise sources applied are: RMS(sensor)=10^{-2} μm, Bias(sensor) =10 μm, Angular Bias(sensor) = 1°, Earth Sensor RMS(ω) = 10^{-5} ω, RMS(FEEP) = 5 10^{-9} N (at 20 Hz), BIAS(FEEP) = 5 10^{-9} N. Drag = 1.5 10^{-5} N at orbital frequency (T_{orb}=5701.64 s) with 10% of noise. The purpose of the DFC is to reduce drag at the orbital frequency (the short periodic whirl oscillations are not relevant at this point and they are taken care of by the whirl controller): it is apparent from the PGB-Spacecraft curve that the amplitude of the oscillation at the orbital period (caused by drag) has been significantly reduced. As for the test mass, note that the curve giving its displacement from the PGB has been shifted by -2·10^{-4} m in order to avoid it being hidden by the previous one. In this case too the amplitude of the oscillation at the orbital period is quickly reduced by the DFC.

In summary, the DFC fulfils the scientific requirements of the GG mission. Although longer numerical simulations are needed, including partial drag compensation also along the spin/symmetry axis, we see no obstacles. It is also not a problem to add notch filtering at other frequencies (e.g. the second harmonic of the orbital drag…). However, it has been found that the performance of the DFC depends heavily on the knowledge of the spin rate: (Earth Sensor RMS(ω_s)). The requirement on the RMS(ω_s) cannot be relaxed beyond 10^{-4} ω_s, which appears to be doable (see Sec. 5.5, p.138).

7. MISSION OPERATIONS AND GROUND CONTROL

7.1 MISSION OPERATIONS CONCEPT

The GG mission is devoted to a single experiment that, once initialized, runs uninterrupted to the end of the scientific data collection (*6 months* after the end of the set-up and first calibration). There are no maneuvers, either orbital changes or attitude slews, during the scientific mission. The processing of scientific data is done in bulk, therefore no scientific *quick-look* is required. All scientific operations are autonomous, executed on the basis of time-tagged operation sequences that are loaded at least one day in advance. Given the high level of autonomy, the tasks of the ground control are essentially limited to:

- Generation and transmission of command sequences and parameters
- Analysis of satellite data to establish that the satellite is operating correctly.

A summary timeline of the mission is provided in Table 7.1.

The mission requires an equatorial orbit and therefore an equatorial station (San Marco) is ideally suited. Because of the low-inclination orbit, a regular pattern of ground passes with almost constant duration can be assumed. Support by other stations in the early orbit phase and the critical spin-up maneuver is a possibility to be reviewed. After the nominal attitude has been achieved no other attitude maneuvers are needed throughout the life of the mission.

As it is customary, the ground segment will include, besides the ground station, an Operational Control Center (OCC), responsible of the execution of the mission operations, and an Operational Scientific Center (OSC), responsible of the generation of the scientific operation sequences. There is no special requirement for real-time interaction between the on-board payload and the OSC, or, in general, between the satellite and the OCC.

7.2 INITIALIZATION, CALIBRATION AND CONTROL

The main operational modes of the satellite (after commissioning at the beginning of life) are:

a) Experiment Set-up and Calibration Mode (see also Sec. 2.1.7)
b) Normal mode (scientific operation of the experiment)
c) High-rate Data Collection Mode
d) Safe (Hold) Mode.

The experiment set-up phase will be based on semi-autonomous procedures, possibly with intermediate checks by the ground after each phase before the next operation is executed. The experiment set-up includes the balancing of the test masses (see Sec. 2.1.4) and the mechanical balancing of the capacitance read-out sensors (see Sec. 2.2.1). Both operations need to be repeated at regular intervals, estimated as *20 days* for the balancing of the test masses and *15 days* for the mechanical balancing of the capacitance bridge (see Sec. 2.2.3). Automatic procedures for such operations will be elaborated, possibly with some interaction with the ground control.

Launch and Ascent Phase		
duration:	≈1 hour	- spinning release by the launcher
		- satellite off activation of OBDH and RF by separation switch
Early Orbit Phase		
duration:	≈1 day	- sun acquisition, rate damping and coarse attitude stabilization (autonomous)
		- satellite acquisition by the EOP ground station network
		- satellite health check
Satellite Commissioning		
duration:	≈1 week	- satellite control handed over to the dedicated ground station (San Marco, Kenya assumed)
		- subsystem commissioning
		- satellite spin-up (semi-autonomous, assisted by the ground station)
Payload Switch-on and Calibration		
duration:	≈3 weeks	- FEEP thruster switch on (pre-calculated thrust profile)
		- Coarse thruster calibration
		- Activation of electrostatic dampers common-mode sensing
		- PGB unlocking
		- Activation of common-mode sensing
		- Activation of drag-free control
		- Activation of spin rate control
		- Test mass unlocking
		- Test mass centering & alignment
		- Fine test mass set-up / iteration
Scientific Measurements		
duration:	6 months	- Routine data collection

Table 7.1 Sequence of events

In the science measurements phase, the operation will be essentially autonomous. The Normal Mode is characterized by the drag-free control, executed by the FEEP electric min-thrusters. However, the survival of the mission does not depend on the drag-free control, since the stability of the operational attitude is guaranteed by the gyroscopic stability. In case of malfunctions, the scientific operations will be put on hold and housekeeping data will be collected and transmitted to ground on the next station passes; resumption of the operations will be commanded by the ground.

Generally, the command and parameter sequences of the Normal mode will need to be updated on a time basis of several weeks, except in the set-up phase when the frequency will be higher (some hours).

The scientific data are sent to ground after demodulation, and the telemetry rate is generally small (see section 7.3 below). Exceptionally, it may be necessary to transmit to Earth the raw (non demodulated) data, for special checkout, parameter identification, and troubleshooting. Because of the nature of the experiment, it is anticipated that the duration of such high rate data collection periods does not need to be longer than about *10 minutes*. Therefore, the telemetry capacity of the telecommunication links is not exceeded.

7.3 SCIENTIFIC DATA MANAGEMENT

The scientific data comprise the position of the test masses relative to each other and the "laboratory" (PGB), the time, the spin reference signal and ancillary data such as the temperature, the attitude of the spin axis and the phase difference between the PGB and the spacecraft's outer vessel (see Table 7.2). The scientific signals are demodulated on board at the spin frequency and only demodulated data (i.e., the data that contain the putative Equivalence Principle violation signal at the orbit frequency) are sent to ground.

DATUM	DATA RECORDS	NO.	SAMPLING RATE (Number of samples / Typical period)	COMMENTS
Relative position of test masses	Electrical potential phase and amplitude	2	100/500 sec	Natural differential period ≅ 500 sec
Relative position of PGB w.r.t. spacecraft vessel	Electrical potential phase and amplitude	2	20/300 sec	Natural period of oscillation ≅ 300 sec
Relative position of each Test Mass w.r.t. PGB	Electrical potential phase and amplitude	2x2	20/100 sec	Natural period of oscillation ≅ 100 sec
Spin period reference signal (from Earth Sensor)	Time, phase & amplitude	3	15/ 0.5 sec	Spin period ≅ 0.5 sec
Temperature		1	20/500 sec	
Spin axis attitude	2 angles	2	20/500 sec	
Phase difference between PGB and spacecraft vessel		1	10/300 sec	Natural period of oscillation ≅ 300 s

Table 7.2 Scientific data

The only exception is the spin reference signal, used for the demodulation, that is sampled *15* times per spin period of *0.5 sec*, that is at *30 Hz*, and is sent to the ground without further elaboration.

The scientific data collection rate is small, about *1.5 kbit/s*, and the total telemetry rate is well below the limit data rate (*1 Mbps*) of the ESA S-band ground stations, including Malindi, even in the worst case of *24-hour* autonomy from the ground (see Sec. 5.6). In normal circumstances, we assume the data are downloaded to ground at each orbital pass.

The data set needed for post-processing and elaboration of the scientific products include the data in Table 7.2 above plus the spacecraft positional data. Tracking with a normal accuracy of several km along-track is sufficient for the purposes of the scientific mission.

The minimum integration time of the experiment is determined by the thermal noise and is about *7 days*. Hence, examination of the scientific data at shorter intervals is, strictly speaking, not significant. Therefore, quick look procedures are not needed and the scientific data can be routed to the Scientific Data Center within a couple of days of reception.

On the other hand, for the purposes of checking the health of the scientific payload and the correct execution of the measurement procedures, shorter reaction times may be desirable. Tests based on consistency checks, threshold parameter values etc. will be elaborated and implemented in automatic self-check procedures that can be run periodically by the payload computer, and can be used to alert the ground control of any non-nominal state of the scientific payload. Data affected by anomalies of any sort will be rejected on post-processing and will have no effect but a shortening of the data collection period (which could be made up for by a corresponding extension of the mission lifetime).

The tasks of the Operational Control Centre (OCC) will comprise, besides the normal spacecraft operations (mission planning, monitoring and control; orbit and attitude determination), also the execution of the operations required by the scientific measurements. The OCC will be responsible for routing of the payload telemetry to the Operational Scientific Centre (OSC), and processing of the telecommand requests from the OSC. Co-location of experimenter staff at the OCC, particularly during the early set-up phase, when interaction with the payload on board is more frequent, may be considered.

The data set resulting from the mission will be archived on CDROM and put at the disposal of the scientific community. The complete data set will include raw data, calibrated data and support data (housekeeping, tracking and attitude). The complete data set is expected to comprise about *26 Gbit*.

8. GG PROGRAMME DEVELOPMENT APPROACH

8.1 SATELLITE DEVELOPMENT APPROACH

This chapter describes the approaches and the methods defined for the design, development and verification of the GG satellite. An outline of the programme logic, development and verification approach for the complete satellite is included. The approach described below is the baseline for the satellite programme cost estimate.

8.1.1 PROGRAMME LOGIC

The GG Design and Development will be implemented in a Definition phase and in a Development and Production phase, i.e. respectively at Phase B and at Phase C/D. Phase B includes the definition of the GG flight system and its relevant support equipment and the finalization of the System and Payload design. Phase C/D includes the detailed design, the development, production, verification and delivery of the GG flight Satellite with the Payload installed on it, the associated support equipment, and the launcher adapter.

The satellite-level programme (as opposed to the payload, which is unique and needs a dedicated, lower level programme) will be matched to that of the PRIMA bus, insofar as applicable; this exercise will be done as soon as guidelines for the PRIMA development are published. Within the two major phases, the GG project will be executed in distinct steps with clear milestones checking the successful execution of one step and thus authorizing commencement of the next step. Generally, phases B and C/D are divided in several sub-phases which have their own technical content and are closed with specific reviews. Typical project system sub-phases are:

- System Definition
- System Design
- Detailed Design
- Manufacturing
- Qualification
- Acceptance
- Pre-launch.

The System Technical Reviews are:

- System Requirement Review (SRR)
- System Design Review (SDR)
- Critical Design Review (CDR)
- Qualification Review (QR)
- Flight Acceptance Review (FAR)
- Launch Readiness Review (LRR)

8.1.2 DEVELOPMENT APPROACH

The GG Satellite development and verification will be based on a simplified Protoflight approach in which only one complete satellite model is manufactured and assembled at flight standard. Furthermore, given the heritage from the PRIMA bus, functional tests at the subsystem level are not included in the programme, the subsystem verification being performed at system level in the frame of the integration and system tests.

On the other hand, at payload level (PGB with test masses and dedicated control computer driving the active damping and drag-free control) both a Structural-Thermal Model and Development Model are planned. The purpose of such models is to verify the mission specific functionalities separately, thus avoiding adverse impacts on the system level programme.

The STM, representative of the structural and thermal behaviour of the payload module, will be subjected to a test and validation campaign whose main purpose is to validate and refine the mechanical and thermal mathematical models. As a result, simulations of the P/L performance will provide more accurate predictions. Moreover it will be possible to perform experiments on critical mechanisms, such as the lock/unlock devices.

The Development Model will be a breadboard, functionally representative of the entire payload module, and will be subjected to a validation campaign consisting of functional and electrical tests. The main purpose of this model is to debug well in advance the design of critical items and verify the integration of the relevant software (active damping and drag-free control running in the payload computer). The basic building blocks of the DM are already being assembled as part of the GGG laboratory prototype (see Chap. 3). In this way the programme C/D phase can start with the most critical aspects of P/L design already verified.

At system level, the verification of the functional and software interfaces between the payload module and the system will be performed on the Protoflight Model, replacing the development models with the flight standard equipment and reusing the payload model EGSE.

MODEL PHILOSOPHY. Based on the above criteria, a GG model philosophy has been developed that (a) minimises the hardware (number of models) in the interest of cost and schedule effectiveness, (b) minimizes the development risk by decoupling the activities at the level of the Service Module and Payload Module. Hence, three verification levels are planned, at Equipment level, Payload level and System level, as shown in Fig. 8.1.

HARDWARE MATRIX. Table 8.1 shows the hardware matrix of the spacecraft equipment. The equipment heritage from the PRIMA bus is shown in the last column. (Note that, as far as cost is concerned, FEEP thrusters and FEEP electronic unit are included in the payload cost).

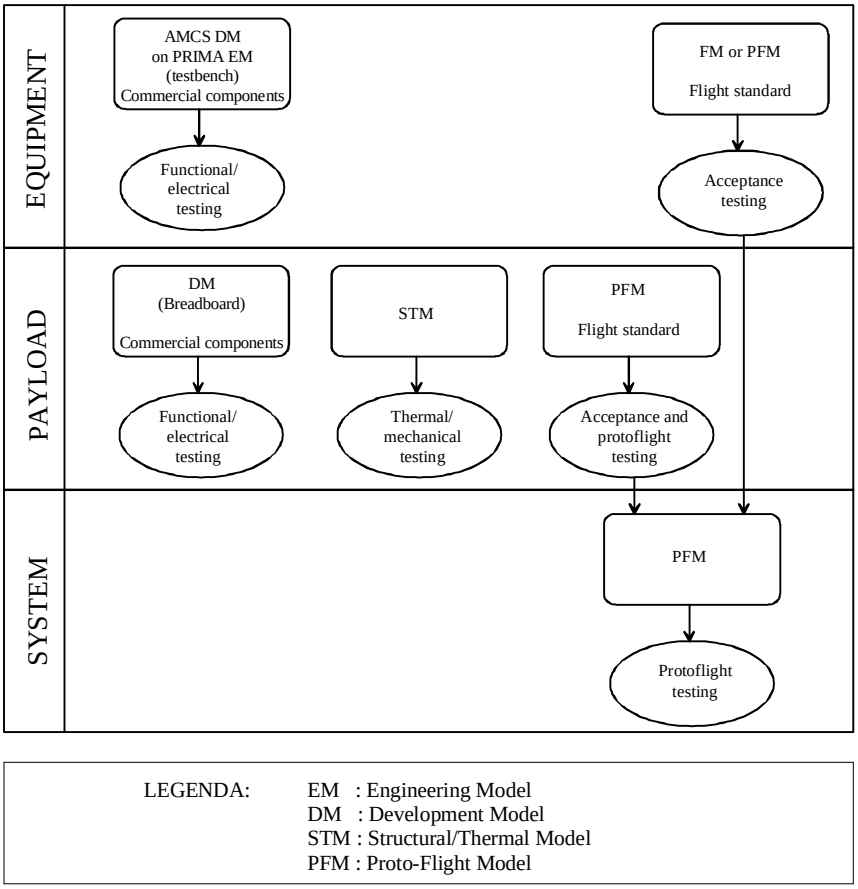

Figure 8.1 Model Philosophy

EQUIPMENT	QUAL. LEVEL	DM	STM	PFM/ FM	SUPPLIER	HERITAGE
ELECTRICALPOWER S/S						
PCDU	O			1	FIAR	PRIMA
SOLAR ARRAY	N/O [1]			1	FIAR/ CISE	PRIMA
BATTERY	O [2]			1	FIAR	PRIMA
INTEGRATED CONTROL S/S						
ICS	O			1	ALENIA/ LABEN	PRIMA
TT&C S/S						
TRANSPONDER	O			1	ALENIA SPAZIO	PRIMA
S-BAND ANTENNA	O			2	ALENIA SPAZIO	PRIMA
RFDU	O			1	ALENIA SPAZIO	PRIMA
AMCS/DFC S/S						
FEEP E.U.	N	1		8	LABEN	
FEEP THRUSTER	N	1		8	LABEN	
SUN/EARTH SENSOR [2]	O			1	ALENIA DIFESA	PRIMA
COARSE SUN SENSOR	O			1		PRIMA
REACTION CONTROL S/S [2]						
N THRUSTER	O			4	BPD	PRIMA
LATCHING VALVE	O			2	BPD	PRIMA
PRESSURE TRANSDUCER	O			1	BPD	PRIMA
FILL/VENT VALVE	O			1	BPD	PRIMA
GAS TANK	O			1	BPD	PRIMA
TUBING & MANIFOLD	O			1 Set	BPD	PRIMA
THERMAL CONTROL S/S	N			1 Set	ALENIA SPAZIO	
STRUCTURE S/S						
MAIN STRUCTURE	N			1	ALENIA SPAZIO	
ANTENNA BOOM & MECHANISM [3]	N			2/1		
HARNESS S/S	N			1 Set	ALENIA SPAZIO	
PAYLOAD	N	1	1	1	LABEN	

Legenda: O = Off-the-shelf M = Modified Design N = New Design

Notes: [1] New panel, off-the-shelf solar cells
[2] Availability (with suitable characteristics) as part of PRIMA bus to be confirmed
[3] Deployment mechanism for bottom antenna only

Table 8.1 Hardware Matrix

8.1.3 VERIFICATION APPROACH

The verification activities will be incrementally performed at different levels and in different phases, applying a coherent bottom-up building block concept, from the equipment to the overall system. The verification programme will cover all the aspects of flight hardware and software together with the associated ground support equipment and other verification tools.

The methods which accomplish the verification of the applicable requirements are, in agreement with consolidated standards, Analysis (including similarity); Test; Inspection; Review Of Design. In general, test is the preferred one, but analysis and other methods can be used in lieu of it if test is not possible or the effort of it is unacceptable with respect to cost and/or schedule constraints.

In line with the verification approach and the model philosophy presented above, a coherent GG integration and test programme will be implemented. As anticipated, some of the verification activities will be performed at lower level, i.e. Experiment (PGB) and equipment, providing in this way a good decoupling of the activities.

The integration and test activities at Satellite level are described below. Table 8.2 shows a summary of the tests performed at Satellite level.

TEST	PFM
Physical Properties	Mass MoI/CoG Spin Balance
Mechanical	Spin Acoustic Leak Pyro Separation Shock Launcher I/F Fit Check Antenna Deployment Check
Alignment	Performance
Thermal	Thermal Vacuum / Thermal Cycling
Electrical	EMC Functional/Software Performance (limited)
Compatibility	System Validation

Table 8.2 System PFM Tests

Protoflight Model (PFM). The system PFM is the satellite flight unit. The PGB will be integrated on the GG service module and then the avionic units and the payload electronic units will be integrated to reach the flight configuration and to perform the system protoflight test campaign before shipping to the launch site.

During the integration of the equipment onto the service module, interface checks, mechanical and electrical, and bonding measurements will be made to verify the adequacy of the assembling. Having completed the integration, subsystems and PGB functional tests will be performed to verify the related functionality, operative modes and the communication between them. At the end an Integrated System Test (IST) will be accomplished to verify the functions and performance of the system.

The IST will be re-executed at the end of the environmental test campaign to detect any degradation of the system. Furthermore, to detect system degradation, if any, during the environmental test and to perform a trend analysis of the main system parameters, a reduced

system functional test (Integrated System Check) will be performed after the EMC and Acoustic test.

The tests will be performed using the system EGSE which allows to acquire the telemetry, generate telecommands, simulate and test the EPS, simulate and stimulate the Attitude sensors and actuators, to simulate the satellite dynamics, kinematic and external environment to perform AMCS closed loop tests, simulation and test of PGB, on board SW up/down loading and testing, test of TT&C and archiving of test data.

After the functional/performance (limited) tests the environmental test campaign will be executed. It will consist of:

- Mass Properties Measurement, in order to verify the mass, inertia, centre of gravity and balancing of the satellite (Spin Balance Test). If necessary, suitable balancing masses will be mounted on selected locations to recover any possible centre of gravity deviation and unbalance. If the spin balance test is done with an empty tank, a correlation with the analytical model (tank full) shall be done.
- Acoustic Test, in order to verify that the satellite can withstand the acoustically induced vibration environment encountered during all mission phases. All spacecraft subsystems which will operate during the launch shall also be operated and monitored during the test.
- Separation Shock Test**,** to demonstrate the capability of the satellite to withstand the shock levels and frequency spectra due to the launcher separation, i.e. firing of the pyrotechnic devices. Before performing the test, the Launcher I/F fit check will be performed.
- Antenna Deployment Test, in order to check the mechanical deployment of the bottom antenna. The test will be performed after each environmental test.
- Thermal Vacuum/Cycling Test**,** in order to demonstrate the ability of the satellite to meet the operational requirements under space environment and at temperature extremes which simulate those predicted plus acceptance margins. Moreover this test will detect, if any, materials, process and workmanship defects that could occur under thermal vacuum and thermal stress conditions.
- Electromagnetic Compatibility Test . The EMC test will be performed to verify both the external compatibility with the launcher and the launch site and the internal compatibility, and to asses the EMC safety threshold (6 dB). During the test the satellite will operate in the modes of operation used during flight. Both conducted and radiated emission and susceptibility tests will be performed. DC magnetic emission test and the magnetic cleanliness will be accomplished in order to verify the compliance with the applicable magnetic requirements
- Steady State Load Test, to demonstrate that the satellite is capable of sustaining the launch and spin quasi static load without suffering permanent deformation or failure. The Spin Test at *120 r.p.m*. will be used which provides a fast and effective way of testing.

All the environmental tests will be performed with the PGB in locked condition. Hence, a strong effort must be done to correlate by analysis the tested configuration, i.e. PGB locked, with the flight configuration, PGB unlocked, both in terms of satellite balancing and thermal behaviour. At the beginning and at the end of the environmental tests, alignment and leakage tests will be performed in order to trace any degradation of the system.

The compatibility between the Satellite and the Operational Control Centre (OCC) will be demonstrated by performing a System Validation Test (SVT) which will consist in the demonstration of the RF and data compatibility with the Ground Station and the OCC. A preliminary compatibility check with the Ground Station (RF compatibility) will be performed using a Satellite Suitcase which is a simulator able to receive/ transmit commands/ telemetry via RF.

PROGRAMME SCHEDULE Fig. 8.2 shows the programme schedule. A start in January, 1999 is assumed, with no interruption between programme phases and delivery of the Flight Model to ASI within December 2001. The duration of the phases was estimated based on the typical duration of tests such as those included in the preliminary programme described above. An essential assumption was that advanced development of the payload critical items is already ongoing as part of the GGG laboratory experiment. The resulting durations are *9 months* (Phase B) and *27 months* (Phase C/D).

ID	Task Name	Duration	Start	Finish
1	**System Phase B**	**191d**	**07-01-99**	**30-09-99**
2	Kick Off	1d	07-01-99	07-01-99
3	Preliminary Design Review	1d	30-09-99	30-09-99
4	GG Laben Phase B	191d	07-01-99	30-09-99
5	**System Phase C/D**	**580d**	**01-10-99**	**20-12-01**
6	Kick Off	1d	01-10-99	01-10-99
7	Critical Design Review (CDR)	1d	06-09-00	06-09-00
8	Qualification Results	1d	09-03-01	09-03-01
9	FAR	1d	20-12-01	20-12-01
10	PFM Equipments Manufacturing &	201d	01-06-00	08-03-01
11	S/C PFM Structure Mn. & Int.	132d	07-09-00	09-03-01
12	PFM Units Delivery To Alenia	0d	10-03-01	10-03-01
13	S/C PFM Equipm.s Int. & Tests	50d	11-03-01	18-05-01
14	**PGB PFM Delivery To Alenia**	**1d**	**18-05-01**	**18-05-01**
15	PGB PFM Int. & Tests	5d	19-05-01	25-05-01
16	**S/L PFM Funct. & Environm. Tests**	**149d**	**26-05-01**	**20-12-01**

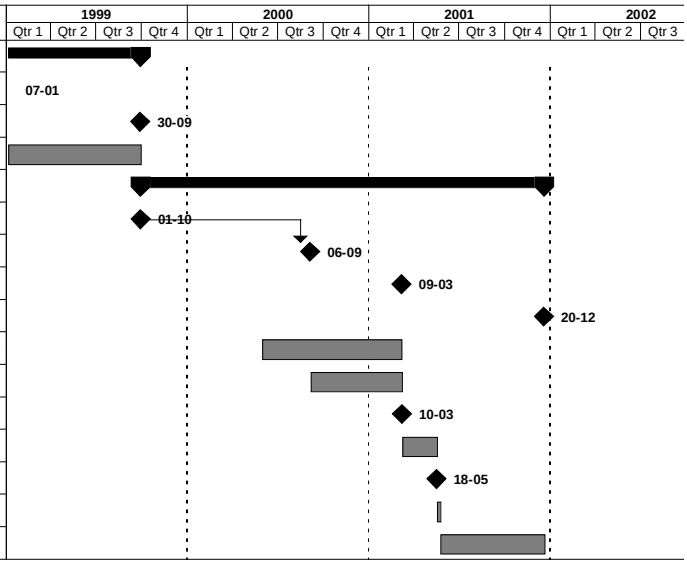

Figure 8.2 GG Programme Development Schedule

8.2 ELECTRICAL AND MECHANICAL GROUND SUPPORT EQUIPMENT

The GG Ground Support Equipment (GSE) is the set of all hardware and software tools needed to support the satellite Assembly, Integration, Verification and Test (AIV&T) programme, in order to demonstrate that all requirements are met and all functions and performances are in accordance with the specifications. According to the different integration stages, the GSE comprises unit Test Equipment, Subsystem GSE and System GSE. Both Mechanical and Electrical GSE are necessary for the GG programme.

MECHANICAL GROUND SUPPORT EQUIPMENT. The following MGSE items are preliminarily identified.

1. Transport containers for the units, the integrated payload (PGB) and the satellite. Special containers with shock absorbers and shock gauges are to be used for the integrated PGB and satellite, to minimize the risk of damage.
2. Lifting and support devices to move the satellite within the integration and test facilities and to simplify unit installation and de-installation.
3. Protective covers for the contamination-sensitive and safety-critical parts such as solar panels, antennas, thrusters.
4. Special facilities for mechanical measurements: physical dimensions, mass, moments of inertia, centre of gravity, balancing, alignment.

Reuse of payload MGSE items 1-3 in the system programme is envisaged. Use of standard PRIMA MGSE for the measurements listed under item 4 will be pursued as far as possible.

ELECTRICAL GROUND SUPPORT EQUIPMENT. At least the following EGSE items are necessary for the electrical AIV&T:

1. Satellite check-out equipment (system EGSE)
2. Payload EGSE (Pico-Gravity Box and payload electronics)
3. On board data handling, power and TT&C EGSE
4. Unit Testers for attitude sensors, PCDU, battery, transponder, gas thrusters and FEEP.

The System EGSE will be used to support the integration and verification of the satellite up to its final flight configuration, and also to support the integration and test of the satellite with the launcher and the launch campaign. The following functions will be implemented:

- Acquisition and monitoring of telemetry data
- Generation of telecommands
- Simulation and test of the power subsystem and its equipment
- Simulation and test of the attitude sensors and actuators
- Test of the Integrated Control System
- Simulation of spacecraft dynamics and environment for AOCS closed loop test
- Simulation and test of the payload
- On board software up/down loading and testing
- Test of the TT&C subsystem
- Archiving of test data for post processing
- Development and execution of test software (test sequences) and a test data base
- Presentation of test data to the test engineers via suitable man-machine interface.

All of the above functions are standard and therefore assumed to be implemented in the PRIMA EGSE (supplemented with the necessary mission-specific software). The same applies to subsystem EGSE (item 3 above) and unit testers (item 4), with the exception of the FEEP.

Payload EGSE is used to test the integrated Pico Gravity Box and its electronic equipment in a stand-alone configuration. A complete functional and performance verification not being possible on the ground, the PGB verification will be performed by analysis and simulations, based on the results of the GGG laboratory experiment. The PGB testing on the ground is therefore limited to the functionality of the electronics and the interfaces with the satellite Integrated Control System. The payload test equipment will perform the following functions:

- Simulation of primary power
- Generation of commands to electrostatic dampers, FEEP and inch-worms
- Acquisition of data from the sensors and the EP measurement chain.

A Unit Tester will be developed to test the FEEP when integrated with their control electronics and high voltage supply. It will include Unit Tester Controller, power supply, and input/output front end to generate commands and monitor the internal parameters (voltage and current monitors being used to compute the applied power and hence the thrust). The I/O front end will also be used at payload and system level to monitor the commands sent to the FEEP and permit closed loop tests.

8.3 TECHNOLOGICAL REQUIREMENTS

The GG proposed design presented herein does not rely on any completely new technologies. Although many requirements of the GG payload are very stringent, they can be met by technologies and processes already existing in the commercial market, which will have to be refined for use in a space application.

The only exception is the Field Emission Electric Propulsion (FEEP); however, even in this case prototypes have already been manufactured and tested and complete qualification is ongoing under ESA contract. An orbital test of FEEP and their electronics is planned during a Shuttle flight within 1999/early 2000, hence compatible with the time schedule of GG. On the other hand, GG is likely to be the first satellite using FEEP for drag free control, a development that will be of great interest for future fundamental physics missions, such as LISA, thanks to the exceptional performance of these thrusters, in terms of linearity, throttling capability and propellant consumption.

A number of critical aspects of the project will be verified in the laboratory in the near future as part of the GGG programme (GALILEO GALILEI ON THE GROUND, see Chap. 3), that can be regarded (besides having scientific objectives of its own) as a "technological" model of the P/L. However the complete flight experiment cannot be completely tested on the ground due to the earth's gravity, which prevents the P/L from being suspended through very thin springs; therefore, some additional activities have to be carried out, prior to the construction of the GG flight model.

The proposed approach to such activities is based on a model philosophy including Structural & Thermal Model, Development Model and Protoflight Model, as described in Sec. 8.1.2.

A survey of the payload elements that may need advanced breaboarding activities, to avoid any risk in the satellite development programme, is presented below.

- The structural and thermal aspects will be tested on the Payload STM together with some critical aspects such as the lock/unlock mechanism. The main purpose of the structural test will be to validate the design with respect to the launch vibration environment. Relevant STMs will be developed for the new design items that need a qualification campaign with respect to the vibration environment, such as the PGB rods.
- The thermal behavior and thermal stability of the payload will be verified during the STM test campaign, although the most critical aspects (i.e. the heat exchange with the S/C through the elastic suspensions) will be tested later at system level. A thermal vacuum test will be performed on the STM to assess the thermal stability of the Test Masses. The baseline thermal design is based on a completely passive control, through the use of MultiLayer Insulation placed on the outer S/C envelope, to provide the required isothermal behavior. The MLI configuration assumed in the design is based on optimum spacing of the blanket sheets without any contact between layers.
- No particular effort is planned because of the acceleration due to the relatively high spin rate. In fact, a static load of $8\ g$ (applying to equipment located close to the periphery of the satellite) is below the level generally used for the design of electronic and mechanical parts that must withstand vibration levels typical of the current launchers.
- More critical items of the payload, such as the elastic suspensions and other delicate mechanisms must be carefully verified from the structural design point of view. The spring between PGB and S/C will provide also electrical paths for signals and power supply of the PGB electronics. It is made up by wrapping the needed number of wires around a stainless steel wire, that provides the necessary elasticity. Some tests to measure k and Q factors have already been performed, providing values reasonably close to the requirements. Further investigation will anyway be carried out in order to define the optimal configuration. Also in the case of the suspension of the test masses, some prototypes and test results are

available. An alternative solution to the helicoidal springs is under study; the spring is made of a number on thin strips, that can be used for the signal and power transmission. Some more investigation on this aspect is planned as part of the DM activities.

- A qualification campaign is required for the **inch-worm** mechanisms, since they are not yet available in a space qualified version, although they have already been used in ultra vacuum and high radiation environments. The electronics driving the inch worms does not present specific problems, with the exception of the aspects related to high voltage, which are however well covered in the past LABEN experience in HV design. Hence no specific development activities are planned. For the same reason the power supply units for the FEEP does not present any specific concern. The configuration is based on a well consolidated design already flown on BeppoSAX and BDPU and that, as mentioned above, will fly within 1999/early 2000 on the Shuttle.
- The capacitance read-out circuit is the core of the experiment. A first breadboard of this circuit has been realised and is presently under test with GGG. This circuit has to be considered with particular care due to the extremely high sensitivity required to detect the displacement between two test masses, close to the current technological capability. Therefore some development on this aspect is envisaged too.
- Another important electronic part that will be tested on GGG is the active damper control electronics. The test will demonstrate the capability of active dampers to suppress, by application of very small forces, the whirling motion that develops in "supercritical" rotation.
- The complete drag free control system cannot be tested on the ground. Verification will be performed by software simulation, incorporating results from tests of the key elements (capacitance sensors, active dampers, FEEP thrusters) as they become available, in such a way as to optimize the control laws with respect to real-world sensor and actuator characteristics.

REFERENCES

Afonso, G., F. Barlier, M. Carpino, P. Farinella, F. Mignard, A. Milani and A.M. Nobili, *Annales Geophysicae*, **7(5)**, 501 (1989).

Aversa, N., *Laurea Thesis in Aerospace Engineering, University of Pisa,* in preparation (1998)

Bartoli, C., von Rohden, H., Thompson, S.P., and Blommers, J., "A Liquid Cæsium Field Ion Source for Space Propulsion," *Journal of Physics D: Applied Physics*, Vol. **17**, (1984), pp. 2473-2483.

Blaser, J.P., M. Bye, G. Cavallo, T. Damour, T., C.W.F. Everitt, A. Hedin, R.W. Hellings, Y. Jafry, R. Laurance, M. Lee, A.M. Nobili, H.J. Paik, R. Reinhard, R. Rummel, M.C.W. Sandford, C. Speake, L. Spencer, P. Swanson, and P.W. Worden Jr., "Satellite Test of the Equivalence Principle"*, Report on the Phase A Study*, ESA/NASA SCI (93)4 (1993)

Blaser, J.P., Cornelisse, J., Cruise, T. Damour, F. Hechler, M. Hechler, Y. Jafry, B. Kent, N. Lockerbie, H.J. Pik, A. Ravex, R. Reinhard, R. Rummel, C. Speake, T. Sumner, P. Touboul and S. Vitale, STEP: "Satellite Test of the Equivalence Principle"*, Report on the Phase A Study*, ESA SCI (96)5 (1996)

Braginsky, V.B., V.I. Panov, "Verification of the Equivalence of Inertial and Gravitational Mass", *Sov. Phys. JEPT*, Vol. **34**, pp. 463-466 (1972)

Bramanti, D., A.M. Nobili & G. Catastini: "Stabilization of Weakly Coupled Rotors: A General Derivation of the Required Forces" (1996), available on line: http://tycho.dm.unipi.it/ ~nobili/ggweb/ pap1/pap1.html

Catastini, G, D. Bramanti, A.M. Nobili, F. Fuligni & V. Iafolla: "Pico Gravity Box (PGB): Efficiency of a Passive Noise Attenuator in Space", *ESA Journal*, **16**, 401-417, (1992)

Catastini, A.M. Nobili & D. Bramanti: "Passive Vibration Isolation in a Spinning Spacecraft" (1996), available on line: http://tycho.dm.unipi.it/~nobili/ggweb/pap2/pap2.html

Cajori, F: *Sir Isaac Newton's Mathematical Principles of Natural Philosophy*, University of California, Berkley, (1934)

Chapman P.K. and A.J. Hanson, *Proceedings of the Conference on Experimental Tests of Gravitational Theories*, Cal. Tech. JPL TM no. 33-499 (1970) 228.

Chen X.,Cousin B.,Mc Ellistrem M., and Hamers R.J., "High-performance, low noise digital controller for inchworm piezoelectric translator", *Rev.Sci.Instrum.*, No.**63**,October (1992), pp.4308-4313

Comandi, G. *Laurea Thesis in Physics, University of Pisa*, in preparation (1998)

Comandi, G., G. Catastini and A.M. Nobili: "Radiometer effect on the GG Test Bodies", (1998), available on line*:* http://tycho.dm.unipi.it/~nobili/ggweb/radiometer/radiometer.html

Cornelisse, K. *Private communication* (1998)

Cowsik, R., N. Krishnan and C. S. Unnikrishnan: "The TIFR Equivalence Principle Experiment", *Proceedings of the 8th Marcel Grossmann Congerence,* Jerusalem (1997).

Crandall, S.H., "The Role of Damping in Vibration Theory", *J. Sound Vib.,* **11(1)**, 3-18, (1970)

Crandall, S.H., *Rotordynamics*, pp. 1-44 in "Nonlinear Dynamics and Stochastic Mechanics", W. Kliemann and N.S. Namachchivaya Eds., CRC Press, Boca Raton, Florida (1995)

Crandall, S.H. *private communication,* (1997)

Crandall, S.H. & A.M. Nobili: "On the Stabilization of the GG System" (1997), available on line: http://tycho.dm.unipi.it/~nobili/ggweb/crandall/crandall.html

Den Hartog, J.P., 1985, *Mechanical Vibrations* (Dover Publications, Inc., New York, first published 1934).

Dickey, J.O. P.L. Bender, J.E. Faller, X X Newhall. R.L. Ricklefs, J.G. Ries, P.J. Shelus, C. Veillet, A.L. Whipple, J.R. Wiant, J.G. Williams and C.F. Yoder, *Science*, **265** (1994) 482.

Einstein, A. *Jahrbuch Rdaioaktiv,* **4,** 411 (1907)

Eötvös, R.V., D. Pekar, E. Fekete, "Beitrage zum gesetze der proportionalität von trägheit und gravität", *Ann. Physik*, Vol**. 68,** pp. 11-66 (1922)

Eötvös, R.V., "Gesammelte Arbeiten" edited by P. Selényi, Akad. Kiadó, Budapest, 307 (1952)

Fuligni, F. and V. Iafolla, “Galileo and the Equivalence Principle”, *STEP Simposium*, 104-109, (1993)

Galileo: *Edizione Nazionale delle Opere di Galilei,* nuova ristampa, Barbera, Firenze, (1968)

GALILEO GALILEI (GG): *Pre Phase A Report*, ASI (1996)

Genta, G. “Vibration of Structures and Machines”, Springer, New York (1993).

Iafolla, V., E.C. Lorenzini, V. Milyukov and S. Nozzoli: "Methodology and Instrumentation for Testing the Weak Equivalence Principle in Stratospheric Free Fall", *Review of Scientific Instruments*, **69**, no. 12, December. 1998.

Jafry Y and M. Weinberger, “Evaluation of a Proposed Test of the Weak Equivalence Principle Using Earth-Orbiting Bodies in High-Speed Co-Rotation”, *Class. Quantum Grav*. **15** 481-500 (1998)

Jones R., Richards C. “The Design and some Applications of Sensitive Capacitance Micrometers”, *Journal of Physics E: Scientific Instruments* **6** (1973) p.589-600.

Lorenzini, E.C., I.I. Shapiro, F. Fuligni, V. Iafolla, M.L. Cosmo, M.D. Grossi, P.N. Cheimets and J.B. Zielinski, *Harvard-Smithsonian Center for Astrophysics Preprint Series* No. 3966, (1994) also in *Il Nuovo Cimento,* **109** B no. 11 Nov. 1195-1209 (1994)

Lund, N. *private communication,* (1995)

Marchal, C. *private communication,* (1996)

Marcuccio, S., Genovese, A., Andrenucci, M., “Experimental Performance of Field Emission Microthrusters”, *Journal of Propulsion and Power*, Vol. **14**, No. 5, September 1998, pp. 774-781.

Marcuccio, S., Giannelli, S., and Andrenucci, M., “Attitude and Orbit Control of Small Satellites and Constellations with FEEP Thrusters,” *Proceedings of the 25th Electric Propulsion Conference*, IEPC-97-188, Cleveland, OH, (1997).

Marcuccio, S., Saviozzi, M., Paita, L., Andrenucci, M., “Flight Demonstration of FEEP on Get Away Special”, AIAA 98-3332*, 34th Joint Propulsion Conference*, Cleveland, OH, (1998).

Melchior, P, B. Barlow, B. Ducarme and M. Delcourt, “Discussion of a Long Series of Gravity Tide Measurements at Alice Springs in the Centre Australia” in IUGG Gen. Assembly, Symp. 20, Canberra (1979).

Nelson, H.D. and S.H. Crandall, “Analytic Prediction of Rotordynamic Response”, Chap. 2 in *Handbook of Rotordynamics*, F.E. Ehrich Ed., McGraw Hill, (1992)

Milani, A, A.M. Nobili and P. Farinella, “Non--Gravitational Perturbation and Satellite Geodesy”, Adam Hilger, Bristol, (1987).

Nobili, A.M.,G. Catastini, A. di Virgilio, V. Iafolla & F. Fuligni: “Noise Attenuators for Gravity Experiments in Space”, *Physics Letters A*, **161**, 45-54, 1991

Nobili, A.M., D. Bramanti, E. Polacco, G. Catastini, E. Rossi, B. Bertotti, P. G. Bizzeti, V. B. Braginsky, V. P. Mitrofanov, W. Flury, A. Brillet, T. Quinn, F. Barlier, C. Marchal, A. Bernard, P. Touboul, A.H. Cook, J. Hough, I.W. Roxburgh and A. Polnarev, *Galileo Galilei (GG), Proposal for the M3 Medium Size Mission of ESA,* (1993).

Nobili, A.M., D. Bramanti, E. Polacco, G. Catastini, A. Milani, L. Anselmo, M. Andrenucci, S. Marcuccio, G. Genta, C. Delprete, E. Brusa, D. Bassani, G. Vannaroni, M. Dobrowolny, E. Melchioni, C. Arduini, U. Ponzi, G. Laneve, D. Mortari, M. Parisse, F. Curti, F. Cabiati, E. Rossi, A. Sosso, G. Zago, S. Monaco, G. Gori Giorgi, S. Battilotti, L. D'Antonio and G. Amicucci, "GALILEO GALILEI. Flight Experiment on the Equivalence Principle with Field Emission Electric Propulsion”, *J. Astronaut. Sc*., **43**, 219-242 (1995)

Nobili, A.M., D. Bramanti, G. Catastini, A. Anselmi, S. Portigliotti, A. Lenti, G. Volpi, S. Marcuccio: “GG-Experience en vol sur le principe d'equivalence avec propulsion electric par emission de champ; GALILEO GALILEI (GG)-Test of the Equivalence Principle with a Small Spinning Spacecraft: The Stabilization of its Weakly Coupled Masses", in Scientific Satellites Achievements and Prospects in Europe”, *Proceedings*, AAAF-ESA, 3-74/89, (1996)

Nobili,A.M., G. Catastini & D. Bramanti: “GG: Dissipation by the Electrostatic Dampers” (1997a), available on line: http://tycho.dm.unipi.it/~nobili/ggweb/qdampers/qdampers.html

Nobili, A.M., G. Catastini & D. Bramanti: "Energy Gained by Whirling Motion as Fraction of Energy Lost by Spinning Rotor" (1997b), available on line: http: //tycho.dm.unipi.it/ ~nobili/ggweb/ratio/ratiol.html

Nobili, A.M., D. Bramanti, G. Catastini, E. Polacco, A. Anselmi, S. Portigliotti, A. Lenti: "GALILEO GALILEI (GG): A Small Satellite for a High Accuracy Test of the Equivalence Principle", *48th Intenational Astronautical Congress*, Turin, Italy, IAA-97-IAA.11.3.01, (1997c)

Nobili, A.M., D, Bramanti, E. Polacco, G. Catastini, G. Genta, E. Brusa, V.B. Mitrofanov, A. Bernard, P. Touboul, A.J. Cook, J. Hough, I.W. Roxburgh, A. Polnarev, W. Flury, F. Barlier, C. Marchal, "Proposed Non Cryogenic, Non Drag Free Test of the Equivalence Principle in Space", *New Astronomy*, **3**, No. 3, pp. 175-218 (1998a)

Nobili, A.M., D. Bramanti, E. Polacco, G. Catastini, A. Anselmi, S. Portigliotti, A. Lenti, P Di Giamberardino, S Monaco, R Ronchini: "Evaluation of a Proposed Test of the Weak Equivalence Principle Using Earth-Orbiting Bodies in High-Speed Co-Rotation: Re-Establishing the Physical Bases", *Class. Quantum Gravity*, in press (1998b)

Pace, E., F. De Martini and F. Melchiorri: "A Capacitive Detector to Test the Equivalence Principle in a Free Fall Experiment", *Rev. Sci. Instrum.* **63(5)**, 3112-3119 (1992)

Paolucci, F., d'Agostino, L., and Burgoni, S., "Design and Performance Study of a Micro-Newton Thrust Stand for FEEP," *Proceedings of the 2nd European Spacecraft Propulsion Conference,* ESA SP-398, Noordwijk, The Netherlands (1997), pp. 465-472.

Renner, J., *Matematikai és Természettudományi Érteitö* **53**, 542-570 (1935)

Roll, P.G., R. Krotkov, R.H. Dicke, "The Equivalence of Inertial and Passive Gravitational Mass", *Ann. Phys.,* N.Y., Vol. **26**, pp. 442-517 (1964)

Su, Y., B.R. Heckel, E.G. Adelberger, J.H. Gundlach, M. Harris, G.L. Smith and H.E. Swanson, "New tests of the universality of free fall", *Phys. Rev. D*, Vol. **50**, pp. 3614-3636 (1994)

Williams J.G., X X Newhall and J. O. Dickey, *Phys. Rev. D,* Vol. **53** pp.6730 (1996).

Unnikrishnan, C.S.: "Experimental Gravitation in India - Progress and Challenges", in India, *Classical and Quantum Gravity*, **11**, A195 (1994)

Worden, Jr., P.W. and C,W.F. Everitt, "Test of the Equivalence of Gravitational and Inertial Mass Based on Cryogenic Techniques", in *Proc. Int. School of Physics E. Fermi, Course LVI: Experimental Gravitation*, Academic Press, New York, pp. 381 (1973)

Worden, Jr P.W., "A Cryogenic Test of the Equivalence Principle", *PhD thesis*, Stanford University, Stanford, California, (1976)

Worden, Jr., P.W., *Acta Astronautica*, **5**, 27 (1987)

The **GG PROJECT** is on the Web at: http://tycho.dm.unipi.it/~nobili/ggproject.html
This **Report** is on the Web at: http://tycho.dm.unipi.it/~nobili/ggweb/phaseA/ index.html